A LEED STUDY OF THE SILICON (100) SURFACE

by

Stephen J. White, B.Sc., M.Sc.

A thesis submitted for the degree of
Doctor of Philosophy, University of Warwick

Department of Physics

March 1977

ABSTRACT

An experimental Low Energy Electron Diffraction study of the Si(100) surface.

The principles of dynamical LEED theory, Constant Momentum Transfer Averaging and Auger electron emission and its angular dependence are discussed.

The experimental systems used for LEED and AES measurements are described together with the specimen cleaning procedures used. It is found that argon ion bombardment followed by annealing is the most effective method of obtaining a clean well ordered silicon surface. The familiar Si(100)(2 x 1) clean surface structure is observed. A new surface phase, the Si(100)(1 x 1)H structure, produced by adsorption of atomic hydrogen, is described.

Data is presented for the angular dependence of Auger electron emission from these surfaces. This method is shown to be of little value in structure determination in this case.

A comprehensive set of LEED Intensity-Energy spectra for the (2 x 1) and (1 x 1)H structures is presented. It is shown that LEED data for the (1 x 1) surface provide a valuable test case for theoretical models of low energy electron scattering from silicon. The (2 x 1) data furnish an experimental foundation for structure determination of this reconstructed phase.

CMTA analysis of the LEED data indicates that the (1 x 1)H structure is probably bulk-like, with a top silicon layer spacing contracted by ≈ 3%. For the (2 x 1) surface the analysis indicates that either

the reconstruction is deep or that CMTA is ineffective in eliminating multiple scattering peaks in this case. The latter explanation clearly augurs ill for the future value of CMTA in surface structure determination.

TABLE OF CONTENTS

LIST OF FIGURES

* * * * * *

ACKNOWLEDGMENTS

Grateful thanks are owed to Professor A. J. Forty for making the facilities of the Physics Department available to me, and especially to Dr. D. P. Woodruff for stimulating my interest in surface studies, for his assistance and encouragement and for his aid in computer data processing.

I would also like to thank Mr. O. S. Simpson for technical support and my colleagues in the Surface Physics group as well as Dr. H. G. Maguire and Mr. P. D. Augustus of the Allen Clark Research Centre, for many valuable discussions.

The Science Research Council supported me financially for the major part of this work, in conjunction with the Plessey Co., Ltd. under a 'C.A.P.S.' award.

Much of the writing of this thesis was carried out while working in the Coordinated Science Laboratory, University of Illinois, with Professor G. Ehrlich, for whose forbearance I am grateful.

Thanks are also due to Professor F. Jona for allowing me to reproduce the calculated LEED profiles in Chapter Six.

Also deserving of thanks are Ms. S. Friedlander for draughting assistance and Mrs. P. Stout for typing the thesis.

DECLARATION

All the work described in this thesis is my own, except where stated otherwise.

Portions of this work have been published or are soon to be published as references [81,95,104,105].

Stephen J. White
Urbana, Illinois, February 1977

A LEED STUDY OF THE SILICON (100) SURFACE

CHAPTER ONE

LEED: EXPERIMENT AND THEORY

I. Introduction

In this chapter we will illustrate the historical development of Low Energy Electron Diffraction (LEED), with particular reference to the relationship between experiment and theory, in order to put into perspective the work to be described later in this thesis.

The driving force behind the interest in surface properties is largely generated by the problem of catalysis; which is still only poorly understood, despite the importance of the processes which depend upon heterogeneous catalysis. An understanding of the nature of the surfaces of metals, in terms of their atomic and electronic structure, and of the way in which other materials are bound to these surfaces, should pave the way to a better theoretical appreciation of the principles of catalysis.

Another important area in which surface properties are of enormous importance is in the field of electronic devices. The electronic properties of semiconductors are dependent to a large degree on their surfaces, because of the existence of localized electronic states associated with the 'dangling' covalent bonds at the surface. A knowledge of the atomic and electronic structure at the surface of an elemental semiconductor such as silicon should enable us to predict with more certainty the properties of the material in its technological role.

Following early LEED work by Schlier and Farnsworth [1] and Lander and Morrison [2] which established the silicon (100) surface net as a

(2 x 1) structure, a number of surface structural models were proposed. More recently surface state and surface energy calculations have led to further proposals.

The unreconstructed Si(100) surface is illustrated in Fig. 1.1. We see that the surface has two 'dangling bonds' per surface layer atom. Clearly this structure is unstable; reconstruction takes place to produce a configuration with lower surface energy as evidenced by the (2 x 1) net observed experimentally.

One model for the reconstruction, proposed by Schlier and Farnsworth [1] is also illustrated in Fig. 1.1. In this model pairs of <110> rows of top layer atoms move together, with new bonds being formed between adjacent atoms. In the following discussions we refer to this model as the 'leaning-rows' structure. A slightly modified version of this model has been supported on chemical grounds by Levine [3].

Another model is that suggested by Phillips [4], based on earlier proposals by Lander and Morrison [2]. In this 'vacancy' structure illustrated in Fig. 1.1, alternate atoms are missing along <110> rows. A similar 'canted ridge' model which also involves surface vacancies has recently been proposed by Harrison [5].

Other proposed models are those by Haneman [6] in which alternate <110> rows are raised perpendicular to the surface with no lateral displacement, and Seiwatz [7] which consists of conjugated pairs of atoms in a zigzag chain.

These structural models are supported largely by chemical arguments, or by calculations of surface electronic properties.

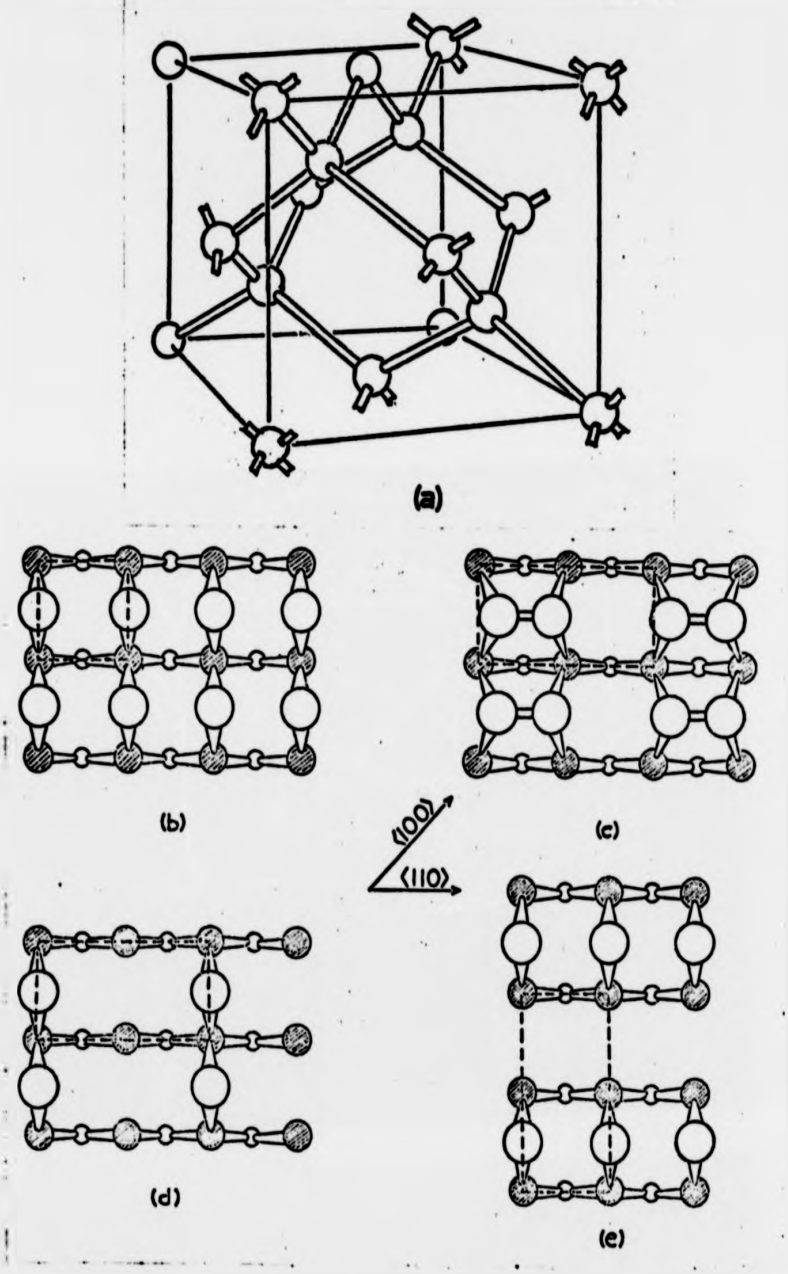

Fig 1.1 The silicon crystal structure and the (100) surface; (a) The bulk, (b) Unreconstructed (100) surface, (c) 'leaning rows' (2 x 1) model, (d) and (e) 'Vacancy' (2 x 1) models. Circles of successively smaller size denote atoms in successively deeper layers, second layer atoms are shaded.

Low Energy Electron Diffraction offers the possibility of being able to determine surface atomic structures both for adsorbate systems and clean surfaces. The purpose of the work to be described here was to gain a better understanding of the LEED process, as applied to a semiconductor, and, if possible, to determine the atomic structure of the Si(100) surface.

II. Historical Development

IIi. Experimental Developments

Low Energy Electron Diffraction was first 'discovered' in 1927 by Davisson and Germer [9], and confirmed the wave-like nature of the electron. Following this early work the technique was somewhat neglected until the early 1960's, when the development of Ultrahigh Vacuum techniques made possible the study of truly 'clean ' surfaces for the first time.

Early work on LEED [8,9] was performed using a Faraday cup to detect diffracted electrons. This approach permitted relatively simple measurements of the intensity in a given beam but was inconvenient in practice. The development of the display system [10,11], allowed the whole diffraction pattern to be viewed on a fluorescent screen, a major advance since the state of order could be assessed and surface structure 'net' determined simply by observing the LEED pattern. This method is now standard practice among LEED workers; though measurement of intensities in this system is more difficult, necessitating the use of a spot photometer to record the brightness of spots on the screen, a rather clumsy approach. The apparatus used in the following studies

combines the two approaches, consisting of a display LEED system, together with a moveable Faraday cup for measurement of beam intensities.

IIii. LEED from Silicon and Other Materials

With the renewal of interest in LEED in the early 1960's silicon was one of the first materials to be studied, Farnsworth [1] and Lander and Morrison [2] in particular performed extensive work on both clean and adsorbate covered surfaces. The experiments carried out at this time (1958-1963) are open to some question, however, since there was no technique available for monitoring the purity of the surfaces studied. Thus we have no knowledge of the degree of contamination of specimens used in these years, though the cleaning processes used, together with system pressures, may give us some clues. It should be noted, however, that the principal surface nets observed by these workers are those which are generally agreed today to be the 'clean' surface structures. These structures are, for the (100) surface a (2 x 1) structure, and for the (111) surface, the (7 x 7) pattern. Lander and Morrison also observed a (4 x 2) structure, which may have been due to an impurity.

Note: In some cases the LEED patterns were indexed differently from the notation used in this work; published photographs of the patterns observed confirm the similarity of the results to more recent studies.

On the basis of their experimental intensity profiles and kinematical calculations, Lander and Morrison proposed structural models

for the (100) and (111) surfaces of silicon. Agreement between the principal features of the predicted and observed intensity profiles was claimed, however it was later shown [7] that similar agreement could be found using quite different structural models.

Following the introduction of Auger Electron Spectroscopy (A.E.S.) as a surface analytical tool (1968) [12,13,14], LEED results could be taken with more assurance of surface purity. An increasing volume of experimental LEED data (for silicon work see the Bibliography [15]) made it clear that Kinematic Theory was inadequate to describe LEED, and that a full Dynamical approach was necessary if the technique was to realize its potential in determining surface structures.

Initially there was considerable divergence in the approach of the various theoretical workers. The principle methods were, the Multiple Scattering Approach of McRae [16], the Band Structure Method of Heine and others [17], and the Inelastic Collision Model of Duke *et al.* [18], and for a number of years these calculations showed only limited agreement with experimental results. Within the last two years, however, the work has been more successful. The different theoretical approaches have largely converged and differ essentially only in the formalism used, and the precise numerical methods adopted. Certain surface structures have now been 'determined' with little ambiguity (notably that of chalcogens on Nickel [19,20,21]) with good agreement of experimental and theoretical curves and agreement between different methods. This work will be discussed in more detail later in this chapter.

Recent work, principally by Lagally *et al.* [22], has indicated that another approach may also be valid. This is the Constant Momentum Transfer Averaging (CMTA) method, a data-reduction technique which attempts to solve surface structure problems by averaging experimental intensity profiles and comparing the results with a pseudo-kinematic calculation. The complexity of the calculation required is reduced considerably in this approach, though a larger range of data is required from the experimentalist. The method has been applied with possible success to the structure of oxygen on Cu(100) [23]. Again we will discuss this technique later in the chapter.

Since LEED now seems capable of determining certain surface structures it seems clear that the problem of the reconstructed surface of a semiconductor such as silicon can be approached again with more confidence. The work to be discussed here attempts to do this by obtaining data suitable for comparison with dynamical calculations, and to investigate CMTA as an approach toward a less complex method for the determination of surface structures.

III. Experimental Aspects of LEED

As in most work concerned with the nature of crystal surfaces, LEED experiments must be carried out in a vacuum, with pressures of less than 10^{-9} Torr. The necessity of this provision is readily seen when we note that the classical kinetic theory of gases predicts that a surface exposed to an ambient pressure of 10^{-6} Torr can be covered by an adsorbed monolayer in 1 second, assuming that all colliding molecules stick to the surface.

In addition the specimen surface must be free of contaminants. Cleaning may be carried out by cleavage in vacuum, heat treatment, inert gas ion bombardment or chemical treatment, depending on the specimen material. The purity of the surface can then be determined by an electron spectroscopic technique, such as Auger electron emission, discussed in Chapter Three.

A schematic diagram of the LEED system used in the present study is shown in Fig. 2.5. The arrangement is typical of most systems, though with the addition of a Faraday cup to monitor beam intensities. The specimen is mounted on a manipulator which permits its positioning in front of the electron beam, adjustment of the angle of incidence and, in some cases, the azimuthal angle.

The electron gun contains a cathode supplying electrons by thermionic emission. These electrons are focussed and accelerated by the anodes, producing a current of ~1μA into a beam of ~1mm in diameter. The electron energy spread in the better instruments is typically ~0.2 eV.

Elastically diffracted electrons leaving the specimen surface are energy analyzed by the grids shown in Fig.2.5 and form a diffraction pattern on the fluorescent screen. The limited resolution of energy analysis results, however, in a contribution to LEED intensities of electrons which have undergone some types of inelastic collision. Thus the small changes in energy (<0.1 eV) produced by phonon interactions are not resolved in most LEED experiments.

IIIi. Intensity-Energy Spectra

As we will see, the diffraction pattern produced in the display instrument yields the symmetry of the surface net directly. In order to determine the positions of atoms within the unit cell we must also measure the intensity of the diffracted beams as a function of one of the diffraction parameters.

The most convenient method in LEED is to vary the incident electron energy and to measure intensity using a spot photometer focussed on the screen, a Faraday cup, or by a photographic technique. The intensity may then be plotted as a function of energy for a given azimuth and angle of incident to form an 'Intensity-Energy Spectrum' (or 'I-V Profile').

IIIii. The Coherence Zone and Surface Order

The energy spread in the electron beam, together with its angular divergence, limit the range over which the beam is coherent. The coherence width (Δw) and length ($\Delta \ell$) are given by [24]

$$\Delta w = \frac{\lambda}{(2\ R/S)(1 + \Delta E/2E)}$$

$$\Delta \ell = \frac{2\lambda E}{\Delta E}$$

where the radius (R) of the electron beam is assumed small compared with the distance (S) between source and sample.

In a typical LEED experiment for E = 150 eV ($\lambda \simeq 1$Å) with an energy spread $\Delta E \simeq 0.2$ eV the coherence length is ~1000Å, much longer than the penetration depth of ~5-10Å. The limited length of coherence can therefore be neglected for most LEED work. For values of (R/S) of 10^{-2}-10^{-3},

a typical range for most LEED experiments, the coherence width is ~100Å. LEED experiments are only sensitive to surface order over this distance.

Disordered areas contribute only to the background intensity in LEED patterns, though if the surface is ordered only over regions somewhat smaller than the coherence width a broadening of diffraction spots is produced. Large scale ordered features on the surface, such as facets or a regular array of steps may produce splitting of LEED beams. Disordering of lesser degree may, while not producing obvious effects in diffraction patterns, result in changes in Intensity-Energy spectra as noted by Jona [25], and discussed later.

LEED is therefore a selective technique which 'picks out' ordered areas in a crystal surface. This is a valuable feature since these areas are often of the greatest interest. It must be remembered however that LEED patterns and I-V spectra may not be representative of the surface as a whole. Careful examination of Intensity-Energy spectra is necessary to ensure that the surface under study is well ordered.

IV. The Principles of LEED and Modern Theory

In the following sections we will describe the principles of the LEED process, and proceeding by analogy from X-ray diffraction, a kinematic approach for calculation of LEED beam intensities. It will then be shown why this simple model has proved inadequate to describe experimental results. The principles underlying a dynamical theory of LEED will be outlined, together with a discussion of recent successful structure determinations; followed by a discussion of the Constant Momentum Transfer Averaging approach.

IVi The Principles of LEED

The surface of a crystalline solid has a lattice structure which is perfectly periodic only in 2 dimensions. This 2-dimensional periodic lattice is usually referred to as a surface 'net' whose structure may be indexed with reference to the substrate structure. There are two standard notations [26,27], the most commonly used being that of Wood; this convention will be adopted in this work.

For example, if the surface structure has primitive translation vectors $\underset{\sim}{a}_{1s}$ and $\underset{\sim}{a}_{2s}$ and those for the bulk are $\underset{\sim}{a}_1$ and $\underset{\sim}{a}_2$, and if:

$$\underset{\sim}{a}_{1s} = 2\underset{\sim}{a}_1 \quad \text{and} \quad \underset{\sim}{a}_{2s} = \underset{\sim}{a}_2.$$

The surface net is described as (2 x 1); the diffraction pattern exhibits half orders in the azimuth corresponding to the direction of $\underset{\sim}{a}_1$. If the primitive vectors of the surface net are not parallel to those of the substrate, then the angle between them is indicated.

We can now define a surface reciprocal net by means of the relation

$$\underset{\sim}{a}_i \underset{\sim}{a}^*_j = 2\pi\delta_{ij}$$

where $\underset{\sim}{a}^*_1$ and $\underset{\sim}{a}^*_2$ are the primitive vectors of the reciprocal net.

Extending this description to three dimensions we see that because of the lack of periodicity normal to the surface we have a 3-dimensional reciprocal lattice which consists of a set of lines or 'rods.'

Now if we consider diffraction of a beam of electrons from a 2-dimensional periodic net as illustrated in Fig. 1.2.; constructive interference will occur when momentum is conserved parallel to the surface:

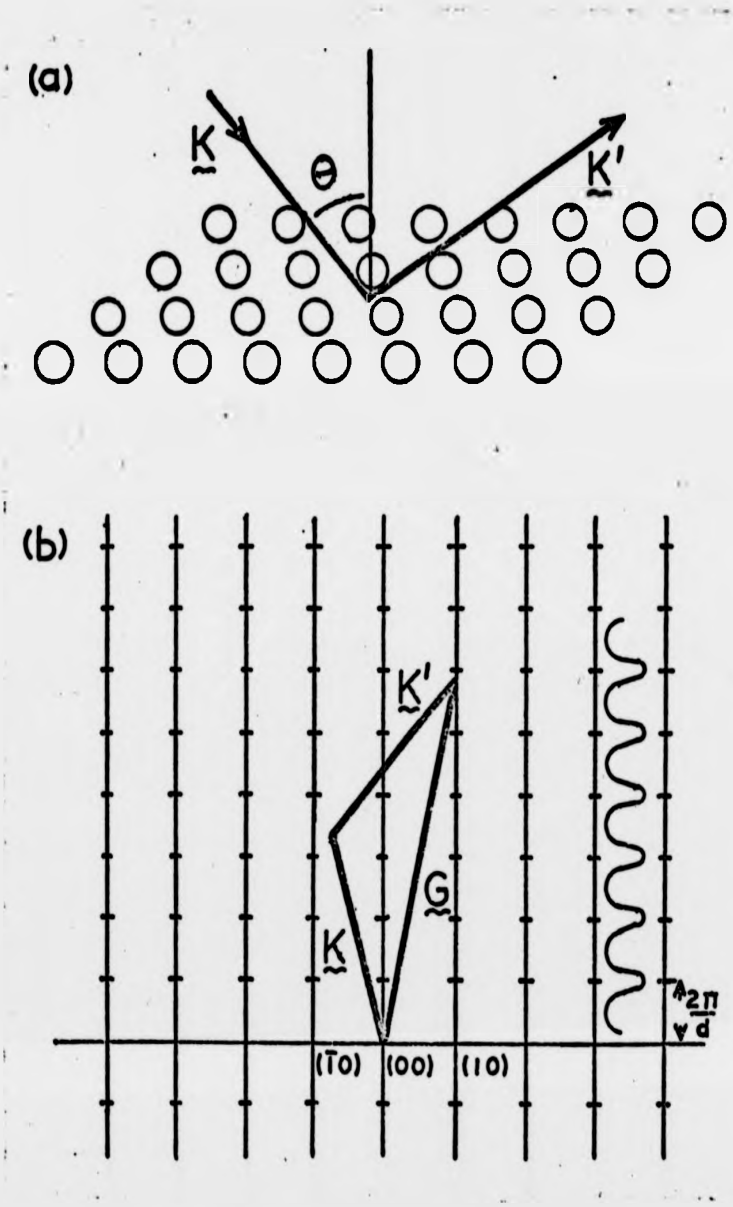

Fig. 1.2 (a) Diffraction from a 2-dimensional structure.
(b) The reciprocal lattice.

$$\text{i.e.,} \quad \hbar\underset{\sim}{K}'_{hk} = \hbar\underset{\sim}{K} + \hbar\underset{\sim}{g}_{hk}$$

$$\text{thus} \quad \underset{\sim}{K}'_{hk} = \underset{\sim}{K} + \underset{\sim}{g}_{hk}$$

subject to conservation of energy

$$\text{i.e.,} \quad \frac{(\hbar\underset{\sim}{K}'_{hk})^2}{2m} = \frac{(\hbar\underset{\sim}{K})^2}{2m}$$

$$\text{thus} \quad |\underset{\sim}{K}'_{hk}| = |\underset{\sim}{K}|$$

where $\underset{\sim}{K}$ and $\underset{\sim}{K}'_{hk}$ are the electron wave vectors of the incident and diffracted beams respectively.

The wave vector is given by the de Broglie relation

$$|\underset{\sim}{K}| = |\underset{\sim}{p}/\hbar| \simeq 2\pi\sqrt{E/150.4}$$

in Å^{-1} where E is the electron energy in eV, $\underset{\sim}{g}_{hk}$ is a reciprocal net vector

$$\underset{\sim}{g}_{hk} = h\underset{\sim}{a}^*_1 + k\underset{\sim}{a}^*_2$$

Thus the diffracted beams reflect the geometry of the reciprocal net.

For a simple unreconstructed solid surface kinematic theory predicts that the strongest scattering into a given beam will occur when momentum is conserved perpendicular to the surface, this corresponds to the familiar Bragg condition for 3 dimensions

$$\underset{\sim}{K} - \underset{\sim}{K}'_{hk\ell} = \underset{\sim}{G}_{hk\ell}$$

where $\underset{\sim}{K}'_{hk\ell}$ and $\underset{\sim}{G}_{hk\ell}$ are the three-dimensional equivalents of $\underset{\sim}{K}'_{hk}$ and $\underset{\sim}{g}_{hk}$.

If the crystal is perfectly periodic in 3 dimensions and the incident radiation samples a large number of atom layers the reciprocal net rods become a true lattice of points as in X-ray diffraction. In the case of LEED however there are departures from perfect periodicity normal to the surface, and the penetration of the electron beam is limited; thus we find that the reciprocal net rods become 'modulated'; the scattering power into a given diffracted beam varies along the length of the rod, being largest near the reciprocal lattice points of the 3-dimensional periodic structure. This is illustrated in Fig. 1.2.

Thus, as the energy of the incident beam is varied, the diffracted beams move along their respective rods, and vary in intensity according to the modulation of the rods. In the simplest kinematical model a plot of intensity versus energy would have single peaks whose width is governed by the attenuation length of the electron wave.

V. The Theory of LEED, an Historical Review

In the following section we will describe the development of theoretical approaches to LEED, and discuss those parameters which have been identified as being important in the calculation of LEED intensities.

We will make no attempt to provide a complete review of all the various approaches, but merely intend to indicate the key developments in the theory. Similarly, a detailed discussion of formalisms and methods of calculation is beyond the scope of this thesis. We will therefore emphasize the physical meaning of the components of a successful theoretical model. A more detailed treatment of theoretical

methods, and extensive bibliographies may be found in the reviews by Tong [28], Webb and Lagally [29], and in Pendry [30].

Vi. The Kinematic Approach

Some of the first attempts to explain LEED Intensity Energy Spectra were based on approaches used successfully in X-ray diffraction, though some early work used dynamical approaches [31,32]. Simple X-ray theory rests on the use of the Born Approximation, that the cross section for elastic scattering of the incident wave is small. Only first order scattering events need be considered, and the diffraction process produces maxima in intensity under conditions predicted by the familiar Bragg formula.

The scattered amplitude in this approximation is:

$$A = A_o \sum_i^N f_i(\theta,E) \exp(i\underset{\sim}{S}.\underset{\sim}{r}_i)$$

where the f_i are the atomic scattering factors, $\underset{\sim}{r}_i$ the position of the i^{th} atom, and $\underset{\sim}{S} = \underset{\sim}{K}' - \underset{\sim}{K}$ is the scattering vector.

The scattered intensity per unit solid angle is then:

$$I(\underset{\sim}{S}) = AA^* = I_o \sum_{ij}^N f_i(\theta,E)\, f_j^*(\theta,E) \exp[i\underset{\sim}{S}.(\underset{\sim}{r}_i - \underset{\sim}{r}_j)]$$

which, for identical scatterers, reduces to:

$$I(\underset{\sim}{S}) = I_o |f(\theta,E)|^2 \sum_{ij}^N \exp[i\underset{\sim}{S}.(\underset{\sim}{r}_i - \underset{\sim}{r}_j)]$$

Considering diffraction from a crystal, with lattice points located at:

$$\underset{\sim}{r}_i = m_1\underset{\sim}{a} + m_2\underset{\sim}{b} + m_3\underset{\sim}{c}$$

where the m's are integers, and $\underset{\sim}{a}$, $\underset{\sim}{b}$, $\underset{\sim}{c}$ are the primitive translation vectors of the lattice; and if the crystal has atomic positions within the unit cell at:

$$\underset{\sim}{\rho}_n = u_n\underset{\sim}{a} + v_n\underset{\sim}{b} + w_n\underset{\sim}{c}$$

the scattered amplitude is:

$$A(\underset{\sim}{S}) = \sum_{in} f_n(\theta,E) \exp\left[i\underset{\sim}{S}.(\underset{\sim}{r}_i + \underset{\sim}{\rho}_n)\right]$$

or

$$A(\underset{\sim}{S}) = \left\{\sum_n f_n(\theta,E) \exp\left(i\underset{\sim}{S}.\underset{\sim}{\rho}_n\right)\right\}\sum_i \exp i\left(\underset{\sim}{S}.\underset{\sim}{r}_i\right)$$

$$= F(\theta,E) \sum_i \exp\left(i\underset{\sim}{S}.\underset{\sim}{r}_i\right)$$

where $F(\theta,E)$ is the Crystal Structure Factor.

The Intensity is then:

$$I(\underset{\sim}{S}) = \left|F(\theta,E)\right|^2 \sum_{ij} \exp\left[i\underset{\sim}{S}.(\underset{\sim}{r}_i - \underset{\sim}{r}_j)\right]$$

$$= \left|F(\theta,E)\right|^2 I(\underset{\sim}{S})$$

$I(\underset{\sim}{S})$ is the Interference Function.

If we now construct the reciprocal lattice for the crystal, we can write an expression for a general vector in this lattice.

$$\underset{\sim}{G}_{hk\ell} = h\underset{\sim}{a}^* + k\underset{\sim}{b}^* + \ell\underset{\sim}{c}^*$$

where h, k, ℓ are integers and $\underset{\sim}{a}^*$, $\underset{\sim}{b}^*$, $\underset{\sim}{c}^*$ are the primitive translation vectors of the reciprocal lattice. Now the interference function is only non-zero when the Laue conditions are satisfied. Intensity maxima will then occur when:

$$\underset{\sim}{S} = \underset{\sim}{G}_{hk\ell}$$

--a generalised form of Bragg's Law.

In the case of LEED the lack of symmetry normal to the surface relaxes the third Laue condition. The isolated spots found in X-ray diffraction then become peaks in a beam of varying intensity which is present at all energies above the emergence condition.

As well as the interference function the structure factor $F(\theta,E)$, also affects the intensities observed.

For example we may write the 3-Dimensional structure factor for silicon

$$F_{hk\ell}(\theta,E) = \sum_n f_n(\theta,E) \exp\left[2\pi i(hu_n + kv_n + \ell w_n)\right]$$

Introducing the basis of the silicon structure (illustrated in Fig. 1.1), with atoms at coordinate positions (0,0,0) and (1/4,1/4,1/4) within the unit cell, the structure factor becomes

$$F_{hk\ell}(\theta,E) = \sum_n f_n(\theta,E)[1 + \exp \pi i(h+k) + \exp \pi i(k+\ell) + \exp \pi i(h+\ell)]\ \{\ 1 + \exp\left[\frac{\pi i}{2}(h+k+\ell)\right]\}$$

The first term in brackets is the structure factor for the f.c.c. lattice, this predicts missing beams for h, k, ℓ values of mixed parity,

due to the choice of the non-primitive unit cell. The second term is due to the basis of two atoms and produces further systematic absences of diffracted beams

VI.(a) The Debye-Waller Factor. When considering diffraction by a real crystal we must take into account the effect of thermal vibrations. Since the time of interaction of an electron with a scattering centre ($\sim 10^{-16}$s) is small compared with the period of an atomic vibration ($\sim 10^{-13}$s), the atoms are effectively stationary as viewed by an incoming electron. The displacement of the ion cores from their equilibrium positions introduces a small time-dependent aperiodicity in the ideal crystal structure, however. An intensity measurement takes place over a significantly longer time than the period of vibration; the collected intensity is then an average over a range of atomic displacements. In X-ray diffraction the intensity of a beam is proportional to the Debye-Waller factor, exp (-2W). For elemental crystals, using the Debye model of the phonon spectrum,

$$W = 8\pi^2 \langle u^2 \rangle \cos^2\Theta_o/\lambda^2$$

where $\langle u^2 \rangle$ denotes the mean square atom displacement in the direction of the diffraction vector. In the high temperature limit

$$\langle u^2 \rangle = \frac{3h^2T}{mk_B\Theta_D^2}$$

where k_B is the Boltzmann constant, m the mass of the scatterers and Θ_D the Debye Temperature of the crystal.

In the case of LEED the description is more complicated, even in the kinematic approximation, since atoms near the surface have a larger vibrational amplitude (a lower effective Debye Temperature), than those in the bulk. This results in a lower diffracted intensity from the top layer, reducing the sensitivity in the region of greatest interest.

In general, however, the Debye-Waller factor predicts a rapid reduction in intensity with increasing temperature, together with decreasing intensities at higher incident electron energies.

The kinematic approximation to LEED, with the addition of damping of the electron wave, enables us to predict the positions of Bragg peaks in LEED spectra for a given surface structure.

It soon became clear however, that this simple approach was inadequate to describe experimental LEED results. Intensity-Energy spectra showed other large peaks in addition to the Bragg features and in general even the kinematic peaks were shifted from their expected positions, and often severely distorted.

These effects occur because of the strong scattering experienced by the electrons in the energy range used in LEED. The strong scattering which makes LEED sensitive to the surface region of the crystal also results in the breakdown of the Born approximation, and multiple scattering events make a significant contribution to the scattered intensity.

Vii Dynamical Theory

One of the earliest attempts at a dynamical theory for LEED in the new period of interest in the 1960's was the approach introduced by

McRae [16], who based his method on the multiple scattering equations formulated by Lax [33].

The principal features of McRae's model were as follows. The primary beam, represented by a plane wave, was incident on a muffin tin model of the crystal; an array of spherical atomic scattering potentials, whose scattering factors could be expressed in terms of the partial wave expansion. Scattering at the boundary of the crystal was formally neglected, as were inelastic processes. The wave field within the crystal was then expressed as the sum of the primary wave and waves scattered from ion cores.

In his model calculation of LEED spectra McRae used the approximation of isotropic scatterers (an 's-wave' model), and predicted the following important characteristic features of LEED spectra.

1.) Bragg Peaks, generated as described by kinematic theory.

2.) Secondary Bragg Peaks, produced by multiple scattering between atom layers

3.) Resonance Peaks in the specular beam, associated with the emergence of a non-specular beam, produced by multiple scattering in a single layer of the crystal

The method adopted of expressing the wavefield as a superposition of diffracted waves within the crystal is essentially one of solving the band structure for the surface region. This fact was explicitly recognized by Boudreaux and Heine [17] in their approach to the problem.

In this method LEED was considered from the point of view of matching wave functions at the surface; the incident plane wave was

matched to Bloch waves and evanescent waves within the crystal. Boudreaux and Heine showed that their calculation predicted the same features identified by McRae (and observed in experimental data).

1.) Bragg Peaks, corresponding to band gaps in the crystal electronic structure

2.) Secondary Bragg Peaks; explained in this formalism in terms of the coupling between allowed Bloch waves, producing a peak in the (00) Beam where there is a Bragg Peak in some other beam

3.) The Surface Wave Resonance. It was shown that under certain conditions a large amplitude may be produced in a beam travelling along the surface, at an energy just below its emergence condition; coupling between Bloch waves then leads to peaks in other beams.

It will be noted that both these early theoretical models formally neglected inelastic scattering processes; the first workers to emphasize the importance of inelastic events were Duke and Tucker [18].

Following the 'many-body' theories of electron-electron interactions in solids of, for example, Pines [34], Duke and Tucker constructed a model of LEED in which inelastic loss processes dominate the characteristics of the electron wave function within the crystal. These electron-electron interactions limit the penetration of the incident beam to ≤ 10 Å for electrons in the energy range $15 \text{ eV} < E < 150 \text{ eV}$. Four principal energy loss mechanisms were identified, namely; creation of surface and bulk plasmons, incoherent particle-hole pair production, and ion core excitation. Phonon scattering is not normally considered

an inelastic process in this context, since electrons which have lost energy to phonons cannot normally be resolved from elastically scattered electrons in typical experiments.

Duke and Tucker pointed out that for an injected electron a few volts above the plasmon emission threshold the first three of these mechanisms lead to a finite elastic lifetime, with an associated uncertainty in the energy of the electron of the order of 1 eV. The most obvious effect of this uncertainty is an energy broadening of Bragg Peaks. Damping also reduces the calculated diffracted intensity to a level of the same order as that observed experimentally.

Calculation of LEED spectra was carried out using the multiple scattering propagator formalism developed by Beeby [35], with the addition of a complex electron self energy to include inelastic processes. Despite the use of the unrealistic s-wave model of scattering this approach gave some qualitative agreement with experimental results.

Most calculations prior to 1971, despite improved methods of dealing with multiple scattering and inelastic processes, continued to use simplified models for the ion core scattering potential. Believing that this was the main reason for the often poor agreement between theory and experiment, Pendry considered the ion cores in some detail [36]. In constructing the potential Pendry examined the two important contributions; the Hartree term, due to the electrostatic field of the core electrons and the nucleus, and the Exchange terms. Screening of the potential by conduction electrons was considered to be a much smaller effect than in conventional band structure calculations, because of the larger scattering power of ion cores at LEED energies.

Ion core potentials for the LEED energy range were calculated in the Hartree-Fock approximation and expressed in terms of phase shifts. An imaginary part was added to the uniform potential between muffin tin cores to represent the effects of absorption.

Using a "hybrid Bloch wave method" Pendry calculated LEED spectra for the Cu(100) surface and achieved good agreement with experiment; he also showed that changes in the form of ion core potential used produced significant changes in the calculated spectra.

One of the first calculations to combine a realistic model of the ion core potential with inelastic scattering and temperature effects was performed by Tong and Rhodin [37]. Duke and Tucker's inelastic scattering approach was used with the addition of higher order, energy-dependent, phase shifts to describe ion core scattering, derived from the Pendry-Capart potential for the LEED energy range. Finite temperature corrections, a Debye-Waller factor to account for the effects of thermal vibrations, were made using the scheme adopted by Duke and Laramore [38]. The method used a perturbation expansion to second order, which was found to converge satisfactorily for the Al(100) surface. Aluminium is a weak scattering, 'nearly free electron' metal. Good agreement was found with experimental results obtained by Jona. Independent calculations by Jepsen *et al.* [39], achieved similar agreement with the same experimental data.

In a subsequent paper Jepsen *et al.* [40], extended their calculations to non-normal angles of incidence and to other metals. Theirs is basically a Bloch wave approach, which they refer to as the layer-KKR

method. In this approach multiple scattering within each layer is treated by the Korringa-Kohn-Rostoker method previously used in band theory, scattering between layers in the beam representation introduced in an earlier work [41].

Ion core scattering was described by the Snow band structure potential, which fits Fermi-surface data, expanded to eight phase shifts. Temperature corrections were included. The appropriate real inner potential and the imaginary component were determined empirically. Calculated spectra for Al(100), Cu(100) and Ag(100) showed good agreement with experimental data, though the fit was less satisfactory for the stronger-scattering Ag(100).

Thus, by 1972, the foundations were laid for a workable approach to structure determination using LEED. A number of workers had produced calculations capable of reproducing experimental results for a variety of metal surfaces [36-40,42], though large computing power and considerable run times were required for most methods.

Perturbation Theory approaches, while making smaller demands in terms of computation, posed problems of their own. In the case of stronger scattering materials perturbation expansions often showed poor convergence especially if inelastic damping was relatively weak.

A method developed by Pendry [43], attempted to circumvent these problems. This method was termed Renormalised Forward Scattering (RFS) perturbation theory. On the basis that the strong scattering regime predominates only in the forward direction, while backscattering is relatively weak, RFS treats forward scattering events 'exactly,'

leaving the weak backscattering to be dealt with in the perturbation approximation. The method produced good convergence (even when backscattering was not weak, due to inelastic damping), and excellent agreement with Pendry's exact Bloch wave scheme for the Cu(100) surface, and was much faster than the latter method.

Another perturbation method, similar to RFS, though with some claimed advantages has recently been developed by Holland and Zimmer [44], and termed the Reverse Scattering (RS) method. The principal virtue of this method is that it can handle co-planar sublayers or layers very close together when other methods such as RFS fail. For simple structures, however, it is slower. For a discussion of some perturbation techniques the reader is referred to Tong [28].

Following successful work on clean surfaces, attention was turned to adsorbate systems. These problems involve the addition of a foreign layer of atoms, characterised by a different set of atomic scattering phase shifts. Calculations have been carried out for a number of systems, notably the Chalcogen (O, S, Se, Te) 'c(2 x 2)' overlayers on the Ni(100) surface. After initial disagreement three independent groups of workers 'determined' the surface structure of oxygen on Ni(100) to an estimated accuracy of ~0.1Å in the 'd-spacing' (normal to the surface) of the overlayer [19,20,21].

Today the major problems associated with the calculation of LEED intensities seem to have largely been overcome. Difficulties still present themselves, the choice of a suitable ion core potential is a question which has still not been fully resolved for many materials;

extension to semiconductor surface structures may increase the difficulty here owing to the markedly non-spherical nature of the silicon atom in the lattice. Perhaps the largest problem is the sheer magnitude of exact methods of calculation. If LEED is to become a routine technique for the determination of surface structures emphasis must be placed on perturbation approaches such as those of Pendry [43], Tong and Rhodin [37] and Holland and Zimmer [44].

VI. The Physical Basis of LEED Theory

In the preceding discussion we have attempted to illustrate the development of LEED theory. The last ten years has seen a dramatic leap in our understanding of the LEED process. In the following section we will describe the physical basis of an accurate theory.

The incident electron beam is represented as a plane wave, characterised by a wave vector $\underset{\sim}{K}$. This wave is incident on the surface of a crystal, the structure of which is modelled in the muffin tin approximation as illustrated in Fig. 1.3.

The muffin tin model consists of a set of spherical ion core potentials, the radius of which may be chosen by consideration of atomic size and charge neutrality within the muffin tin sphere. In between ion cores is a uniform potential, V_o, the Inner Potential of the crystal. This is the potential well which confines conduction electrons to the crystal, and its magnitude may be gauged approximately from work function measurements, the inner potential is then $\phi + E_F$, where ϕ is the work function and E_F is the Fermi Energy, though as has been pointed

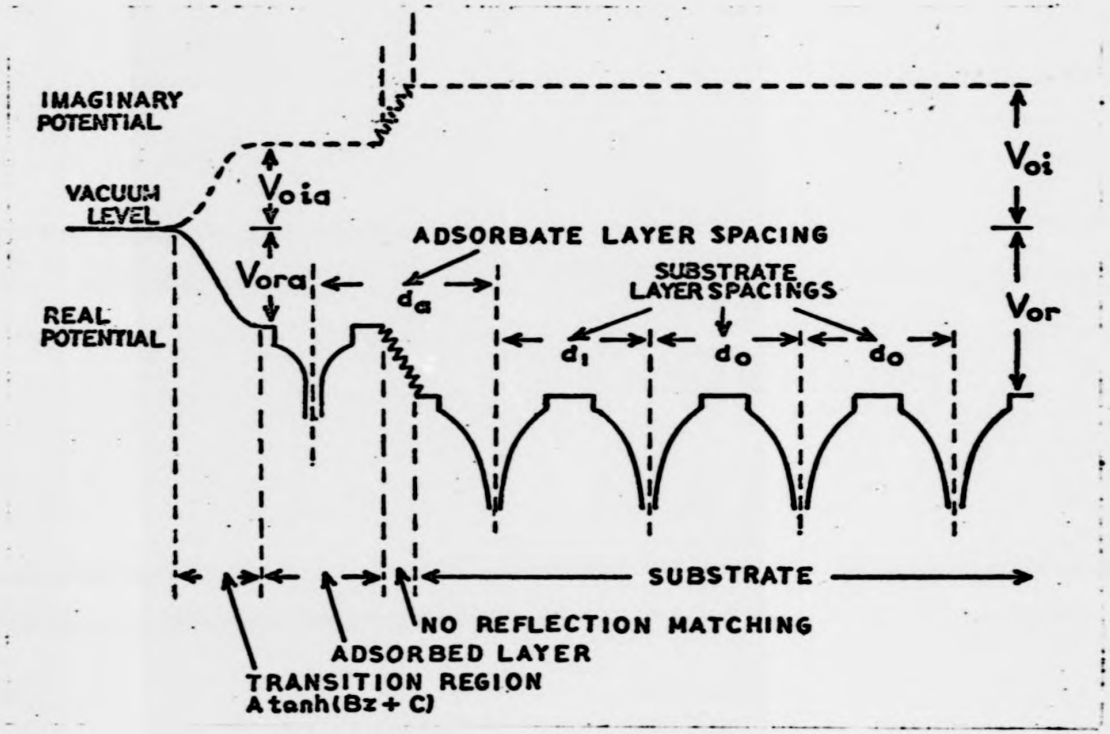

Fig. 1.3 Muffin Tin model of an adsorbate covered surface (after Marcus *et al.* [19]).

out by Jepsen *et al.* [40], the value of inner potential 'seen' by LEED electrons differs somewhat from the 'static' value because of exchange and correlation effects. Thus the effective inner potential is to some extent dependent on the energy of the incident electron though the dependence may be small when the combined effects of both exchange and correlation are considered.

In addition to the real component of potential which increases the energy of the incident electron on entering the crystal, and changes their angle of incidence in a manner analogous to Snell's law, there is an imaginary component, producing damping of the electron wave. This simulates the effect of inelastic processes, principally plasmon generation, which reduces the mean free path of an elastic electron to ~10Å in the LEED energy range. Thus the inelastic processes are represented by the use of a complex 'Optical Potential' [30]. The elastically scattered electron then obeys the Schrödinger equation with an effective or optical potential term. The optical potential may be written:

$$V_{op} = V_{or} + iV_{oi}$$

where V_{or} is the real part of inner potential, and V_{oi} the imaginary component.

This complex potential must then be matched to the vacuum outside the crystal, as illustrated in Fig. 1.3. Abrupt termination of the potential produces unphysical large reflections at the barrier created. A procedure commonly adopted is the 'no-reflection matching' condition

in which the wavelength and angle of incidence are changed by the appropriate amount within the crystal, but effects produced by the energy barrier are neglected. Another method is to smoothly terminate the potential at the surface so that it tails off into the vacuum, within a length of the order of the dielectric screening length, e.g., by a function such as $V_{op} = A (\tanh Bz + C)$, where z is the distance normal to the surface.

Both the real and imaginary components of the optical potential may be determined empirically. Jepsen *et al.* [39,40] use a procedure in which the inner potential is determined by fitting curves calculated at normal incidence to experimental results, 'sliding' curves along the energy scale to produce best agreement of peak positions. Spectra may then be calculated for other angles of incidence using the appropriate 'refractive index' implied by the potential. This procedure may be misleading in cases where there is a large change in spacing at the surface, or when there are adsorbates, since the change in d-spacing or the different phase shifts in the adsorbate layer may produce peak shifts which might be associated with inner potential effects.

The absorptive, imaginary components of the potential may be established by examination of Bragg peaks in experimental spectra; the width of the narrowest peaks is largely determined by the uncertainty in energy introduced by damping. The lowest width that a peak may have is given by $\Delta E \gtrsim 2|V_{oi}|$ [30].

Construction of a suitable ion core potential may be more difficult. As we have mentioned above calculated Intensity-Energy spectra are very

sensitive to the form of potential chosen. We may write the Schrödinger equation for the motion of the incident electron under the effect of the core potential, after Pendry [30].

$$\left[-1/2\ \nabla_o^2 - \frac{Z}{|\underset{\sim}{r}_o|} + v_s(\underset{\sim}{r}_o) + \sum_j \int \sum_{sj} \frac{|\psi_j(\underset{\sim}{r}_j, s_j)|^2}{|\underset{\sim}{r}_o - \underset{\sim}{r}_j|}\, d^3\underset{\sim}{r}_j\right] \phi(\underset{\sim}{r}_o, s_o)$$

$$- \sum_j \left[\int \sum_{sj} \frac{\psi_j^*(\underset{\sim}{r}_j, s_j)\ \phi(\underset{\sim}{r}_j, s_j)}{|\underset{\sim}{r}_o - \underset{\sim}{r}_j|}\, d^3\underset{\sim}{r}_j\right] \psi_j(\underset{\sim}{r}_o, s_o)$$

$$= (E_t - E_{ct})\ \phi(\underset{\sim}{r}_o, s_o)$$

$$= E\ \phi(\underset{\sim}{r}_o, s_o)$$

where $\phi(\underset{\sim}{r}, s)$ is the incident electron wave function, with position and spin coordinates $\underset{\sim}{r}$ and s respectively. The ψ_j's are core state wave functions; Z is the nuclear charge, and v_s is the potential due to the screening charge. E_t is the total energy of the system, E_{ct} is the energy associated with the core states.

The first term in brackets on the left hand side simply describes the motion of an electron in the electrostatic field of core electrons and nucleus. The second term describes exchange effects in the Hartree-Fock approximation. The Hartree, electrostatic, part of the potential may be calculated from atomic wave functions such as those tabulated by Herman and Skillman [45], since the core states are perturbed little in the crystalline state. Accounting for exchange and correlation contributions is still the subject of some uncertainty. In some cases the Slater local approximation for exchange is adequate, and preferred to the full Hartree-Fock term shown above [36]. The Slater approximation gives

$$V_{ex}(\underset{\sim}{r}) = -3\left[\frac{3\rho(\underset{\sim}{r})}{8\pi}\right]^{1/3}$$

where $\rho(\underset{\sim}{r})$ is the local electron density at position $\underset{\sim}{r}$. Other authors [39,40] have used potentials incorporating Hartree-Fock exchange with success.

At this stage some account must be made of lattice vibrations. As we saw earlier the kinematic approach makes use of the Debye-Waller factor which describes the effect of the incoherence introduced by thermal vibrations on the diffracted intensity. In the dynamical method the lattice vibrations are usually dealt with by modifying the effective ion core potentials. In general the vibrational amplitude is a function of the distance of that atom from the surface, with the atoms in the top layer of an elemental crystal having a mean square vibrational amplitude of (typically) twice the bulk value.

The ion core potential is then expressed in terms of phase shifts in the partial wave expansion, sufficient phase shifts must be used to produce accurate results.

Having described scattering of the incident electron wave by a single ion core multiple scattering events are considered. The effective wave field incident on an ion core is expressed as a superposition of the incident wave and waves scattered by other ion cores. A number of formalisms have been adopted, such as those of McRae [16], Beeby [35] and Marcus and Jepsen [39-41].

The diffracted intensity for a given electron energy may then be calculated; repeating the process for a range of energies produces an Intensity-Energy spectrum for a given beam.

Determination of the relaxation of the surface layer of a clean crystal then proceeds by adjustment of the surface plane d-spacing of the model, until good agreement with experimental data is achieved.

In the case of adsorbate systems an appropriate ion core potential for the adsorbate atoms must be calculated, together with a suitable optical potential for this layer, matching this potential to the vacuum on one side, and to the crystal on the other, as illustrated in Fig. 1.3.

The most probably adsorbate atom positions may be inferred from chemical and symmetry considerations, this may be sufficient to determine the 2-dimensional symmetry of adsorbate sites and to give some idea of the d-spacing of this layer. Calculations are then performed for a number of structures, the criterion for the correct structure again being degree of agreement between theoretical and experimental curves.

We will now go on to describe an alternative approach to the analysis of LEED data. Though a less 'exact' approach, and one which has little formal justification, the data reduction, 'Averaging,' approach developed by Lagally *et al.* [22] promises the advantage of structure determination with only simple kinematic calculations.

VII. Constant Momentum Transfer Averaging

In view of the large computing power required, and therefore the high cost of dynamical LEED calculations, it is not surprising that a number of workers have suggested alternative approaches to structural analysis. These mainly consist of data reduction methods in which data is averaged in some way to reduce the contribution of multiple scattering effects, and Fourier Transform methods similar to those used in X-ray work, such as that proposed by Clarke *et al.* [46].

A data reduction technique designed principally for application to overlayer structures is the 'energy-averaging' method proposed by Duke *et al.* [47].

The most promising of these techniques is the Constant Momentum Transfer Averaging (CMTA) approach, developed by Lagally *et al.* [22]. In this method a range of Intensity-Energy spectra at different diffraction parameters are averaged at constant scattering vector $\underset{\sim}{S}$. Multiple scattering features are 'washed-out' in the average, relative to single-scattering Bragg features, leaving spectra which may be compared with kinematic calculations.

To illustrate the principle of this method, we write the diffracted intensity due to single and double scattering events, after Webb and Lagally [29].

$$I(\underset{\sim}{S}) = \sum_{ij} f_i(\theta,E)\, f_j^*(\theta,E)\, \alpha_i\, \alpha_j^* \exp[i\underset{\sim}{S}.(\underset{\sim}{r}_i-\underset{\sim}{r}_j)]$$

$$+ \sum_{\substack{imjn \\ i\neq m \\ j\neq n}} f_{im}\, f_{jn}^*\, \alpha_{im}\, \alpha_{jn}^* \exp[i\underset{\sim}{S}(\underset{\sim}{r}_i-\underset{\sim}{r}_j)] \times \exp\{i[\underset{\sim}{K}'.(\underset{\sim}{r}_{im}-\underset{\sim}{r}_{jn})+|\underset{\sim}{K}'|(|\underset{\sim}{r}_{im}|-|\underset{\sim}{r}_{jn}|)]\}$$

$$= I_1(\underset{\sim}{S}) + I_m(\underset{\sim}{S}, \underset{\sim}{K}, \underset{\sim}{K}')$$

The f's are the atomic scattering factors and f_{in} is the product of appropriate scattering factors, α is a factor representing the attenuation of the incident wave, $\alpha = A_{n+1}/A_n$ the ratio of amplitudes contributed to the scattered beam by atoms in successively deeper layers; α_{im} describes the attenuation involved in the double scattering process

from atoms i and m. This analysis can easily be extended to higher orders of scattering

We see that, while the single scattering summation (the first summation on the left hand side) depends only on $\underset{\sim}{S}$, the scattering vector or momentum transfer; that portion of the double scattering term (and of higher order terms) which describes the interference between doubly scattered amplitudes, depends explicitly on the propagation vectors $\underset{\sim}{K}'$ and $\underset{\sim}{K}$. Thus, if a number of Intensity - Energy spectra are averaged at constant $\underset{\sim}{S}$, those terms in $I_m(\underset{\sim}{S},\underset{\sim}{K},\underset{\sim}{K}')$ for which $r_{im} \neq r_{jn}$ oscillate with variation in $\underset{\sim}{K}$ and $\underset{\sim}{K}'$, reducing these multiply scattered terms to a slowly varying background and eliminating much of the complicated structure in the profiles. Scattering from equivalent pairs of atoms, for which $r_{im} = r_{jn}$ also depends only on $\underset{\sim}{S}$, however, and these terms survive the average, though their contribution to the intensity is simply the single scattering Interference Function. Thus the averaged intensity contains an effective atomic scattering factor, which is different from that used in a simple single scattering model.

Pendry [30] has discussed the effect of averaging in terms of the elimination of multiple scattering features and suggests that the averaged data might rather be termed 'quasi-elastic,' in view of this modification to the atomic scattering factors and the use of the attenuation factor α, which in this description includes both elastic and inelastic processes.

In practice the only effective determination of the success of CMTA is an experimental one. The usual form in which LEED data is

produced is as Intensity-Energy spectra. Averages may be produced by converting then to spectra in $\underset{\sim}{S}$, preferably with an appropriate inner potential correction to account for refraction, and simply summing the curves.

Lagally *et al.* [22] and McDonnell *et al.* [23] have shown that averaging spectra taken over a wide range of angles of incidence is most effective in eliminating dynamical features in a number of materials. Variations in azimuthal angle do not generate sufficient variation in $\underset{\sim}{K}$ and $\underset{\sim}{K}'$ to produce kinematic-like profiles. The most effective approach is to obtain data over a wide range of both these parameters. For several metals, e.g., Ag(111) [22], Ni(111) [48], Cu(111) [23], this procedure produces essentially kinematic profiles, with only small dynamical features remaining.

Comparison with kinematic calculations has demonstrated that CMTA may be effective in the determination of the changes in d-spacing of the top layer of atoms in clean metal surfaces [49].

Adsorbate structures may prove to be difficult to solve. A study by McDonnell *et al.* [23] examined an extensive set of experimental data from both clean Cu(100) and the $(\sqrt{2} \times \sqrt{2})$ R45° oxygen structure on this surface. Kinematic calculations were performed for a number of possible adsorbate structures. Comparison of peak positions within experimental and theoretical spectra, together with examination of the extra features introduced by adsorption, produced a 'best fit' which suggested that the structure is reconstructed, with a top layer of approximately co-planar copper and oxygen atoms.

Lagally *et al.* [49] showed that averaged intensity profiles should be sensitive to adsorbates; calculations for CO on W(100) indicated that the form of the adsorbate could be identified. In addition experimental work for the (00) Beam from the oxygen-on-W(110) structure enabled these authors to eliminate certain of the possible adsorbate structures.

Much of this work is still somewhat inconclusive however, and as Woodruff [50] has demonstrated, the 'phase problem' will reduce the sensitivity of CMTA in adsorbate structure determination.

In LEED the atomic scattering factors, the f_n's, are complex, introducing a phase shift in the amplitude of a wave scattered from this potential. This uniform phase shift has no effect on averaged intensity profiles from clean surfaces. Foreign species, however, with their different f_n, introduce a new set of phase shifts. The positions of the important adsorbate-substrate scattering peaks then depend both on the structure, and on the particular f_n involved; changes in phase produce the same effect as changes in atomic positions. In addition, variation of the phase component of f_n with energy and scattering angle means that adsorbate-substrate scattering features will tend to become washed-out when averaged, severely reducing the sensitivity of the technique for surface structure determination.

Further experimental work is necessary to determine whether this is likely to prove an insurmountable problem.

The CMTA approach offers the possibility of surface structural analysis with only simple calculations which may be carried out by the

experimentalist, though it has the disadvantage of requiring a much more extensive set of data than is necessary for comparison with dynamical calculations. The question of whether the technique is sufficiently sensitive for its purpose is one which is still unresolved.

In a subsequent chapter we will apply the CMTA technique to data from the clean reconstructed Si(100)(2 x 1) surface, and to the Si(100)(1 x 1)H structure produced by hydrogen adsorption. This provides us with valuable new information with which to assess the technique, as they should provide ideal cases for the application of this approach to structure determination.

CHAPTER TWO

EXPERIMENTAL SYSTEM AND PROCEDURES

PART A: EXPERIMENTAL SYSTEM

I. The Ultrahigh Vacuum System

The vacuum system used in these studies is illustrated in Fig. 2.1. The main vacuum chamber is constructed of nonmagnetic stainless steel (type EN58B) and uses standard 'Conflat' flanges, sealed by means of copper gaskets. Fig. 2.2 shows the arrangement of the pumping facilities. The main pump is a 'Ferranti' Ion Pump (speed ~150 ℓs^{-1}); this pumps the main chamber via an isolation valve, which may be closed to permit argon ion bombardment of the specimen or adsorption work. A Titanium Sublimation Pump is fitted, enabling the base pressure of the system to be reached more rapidly; it may also be used to pump active gases when argon ion bombardment is taking place. The pumping speed of this device may be increased by passing water or liquid nitrogen through the cooling coils fitted.

The whole system, including the ion pump and sublimation pump can be baked to 250 °C; after 24 hrs. bakeout and thorough outgassing of the various filaments, etc., the base pressure of the system is normally $\leq 2 \times 10^{-10}$ Torr.

Pressures in the main chamber are measured by means of a 'Vacuum Generators' VIG10 Nude Ion Gauge and IGP3 Control Unit. For the early part of this work (clean surface data) a lanthanum hexaboride (LaB_6) coated rhenium filament was fitted to this gauge. This type of filament

CHAPTER TWO

EXPERIMENTAL SYSTEM AND PROCEDURES

PART A: EXPERIMENTAL SYSTEM

I. The Ultrahigh Vacuum System

The vacuum system used in these studies is illustrated in Fig. 2.1. The main vacuum chamber is constructed of nonmagnetic stainless steel (type EN58B) and uses standard 'Conflat' flanges, sealed by means of copper gaskets. Fig. 2.2 shows the arrangement of the pumping facilities. The main pump is a 'Ferranti' Ion Pump (speed ~150 ℓs^{-1}); this pumps the main chamber via an isolation valve, which may be closed to permit argon ion bombardment of the specimen or adsorption work. A Titanium Sublimation Pump is fitted, enabling the base pressure of the system to be reached more rapidly; it may also be used to pump active gases when argon ion bombardment is taking place. The pumping speed of this device may be increased by passing water or liquid nitrogen through the cooling coils fitted.

The whole system, including the ion pump and sublimation pump can be baked to 250 °C; after 24 hrs. bakeout and thorough outgassing of the various filaments, etc., the base pressure of the system is normally $\leq 2 \times 10^{-10}$ Torr.

Pressures in the main chamber are measured by means of a 'Vacuum Generators' VIG10 Nude Ion Gauge and IGP3 Control Unit. For the early part of this work (clean surface data) a lanthanum hexaboride (LaB_6) coated rhenium filament was fitted to this gauge. This type of filament

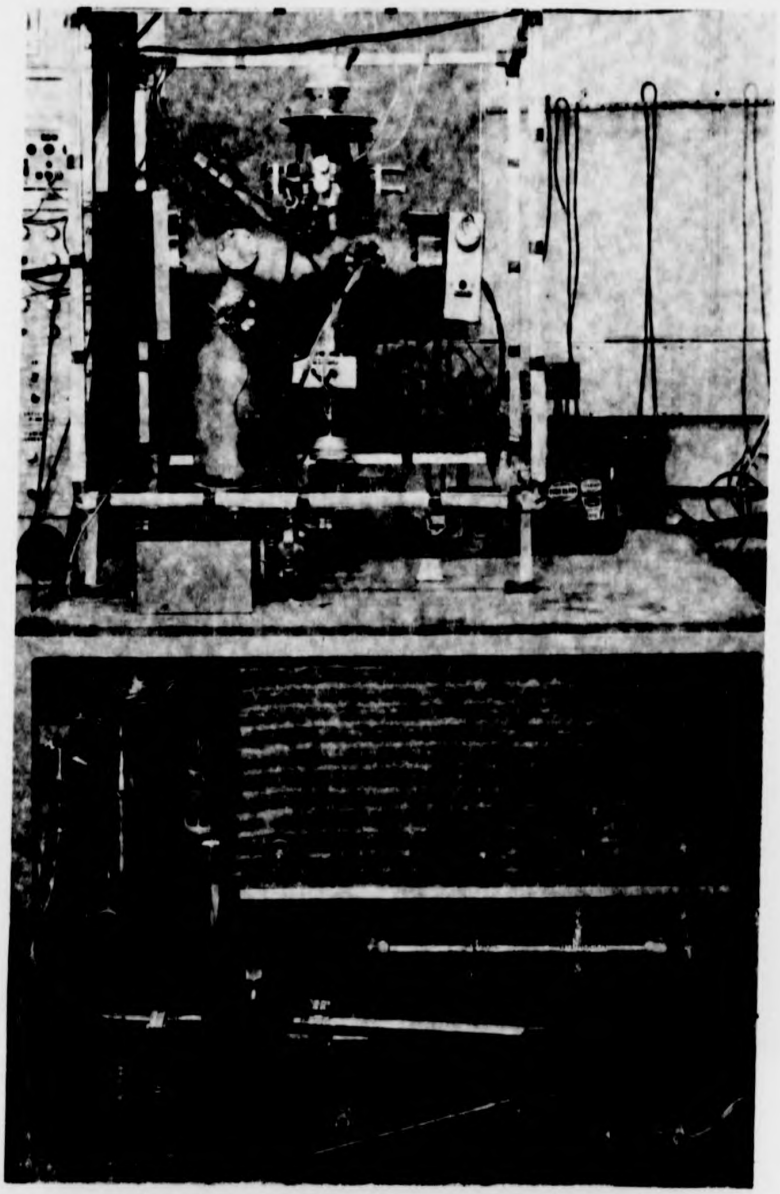

Fig. 2.1 The ultrahigh vacuum system. The specimen manipulator is visible at the top of the system, with the Faraday cup manipulator below it. The viewport is to the left.

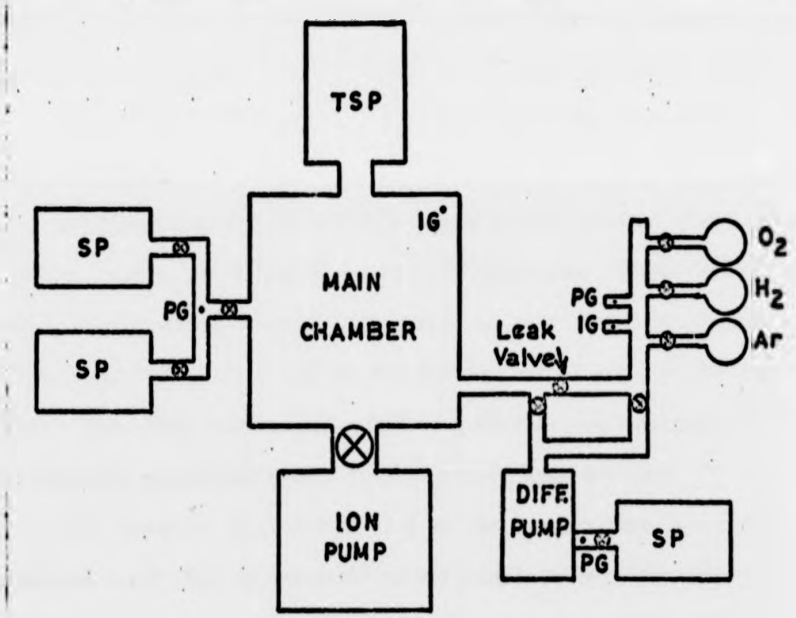

Fig. 2.2 Schematic diagram of the vacuum system.
SP: Sorption pump. TSP: Titanium sublimation pump.
IG: Ion gauge . PG: Pirani gauge. ⊗: Vacuum valve .

produces the necessary electron emission at a lower temperature than that required for tungsten filaments; it is claimed that this lower running temperature reduces both the partial pressure of contaminants produced by the gauge, and the 'cracking' of gases such as CO_2. Later work was performed using this gauge fitted with a simple tungsten spiral filament. No extra contamination was detected when this gauge was used. In both cases the gauge is calibrated for nitrogen pressures, and all pressures quoted in this work are equivalent nitrogen pressures unless stated otherwise.

Rough pumping of the system is accomplished by means of two zeolite sorption pumps. An 'Edwards' mercury diffusion pump (speed ~50ℓs^{-1}) with a liquid nitrogen cooled vapour trap is also fitted for more rapid initial pump down of the system, and for pumping of argon or adsorption gases. This pump is normally backed by a further sorption pump, though for hydrogen adsorption work a trapped rotary pump was used.

Also shown in Figs. 2.1 and 2.2 is the gas-handling line. This stainless steel line is connected to gas supply flasks containing argon, hydrogen, and oxygen. Each flask initially contains 1 litre of gas at 1 atmosphere pressure ('B.O.C.' research grade gases, 99.995% pure). The gas-handling system is pumped by means of the diffusion pump via an isolation valve, and the entire system, with the exception of the gas flasks, is bakeable to 250 °C, independently of the main chamber. Pirani and ion gauges are fitted for pressure measurements, and the base pressure after bakeout is approximately 10^{-7} Torr.

II. Other Facilities

An important feature of the system is the 'V.G.' Q7 Quadrupole Mass Spectrometer; enabling contaminant gases to be identified and their partial pressures estimated, with a sensitivity of ~10^{-11} Torr. Some form of mass spectrometry is absolutely vital when performing adsorption experiments, as we discovered at an early stage of this work. The quadrupole type used here is particularly convenient in use, providing a high-speed scan of mass numbers 1 to 80 on an ordinary oscilloscope display.

The argon ion gun fitted in this system produces an uncollimated beam of ions for specimen cleaning purposes. When operated in a pressure of 10^{-4} Torr of argon the current in the beam is up to ~2 μA at an energy of ~470 eV.

The power supply constructed for resistance heating of the specimen consists of a variable high-voltage supply (0-250 V at 5 A) for use when the specimen is at room temperature and its resistance is high, and a variable low-voltage, high-current supply (0-10 V at 50 A) for use at higher temperatures.

III. The Specimen Manipulator and Heating Stage

The resistance heating stage finally adopted, and used throughout the data collection is illustrated in Figs. 2.3 and 2.4. The stainless steel supports were thoroughly electropolished and rinsed before assembly. Tantalum sheet is used to face those areas which make contact with the specimen, and for the clips which hold the specimen in place. All the tantalum used was thoroughly cleaned using an

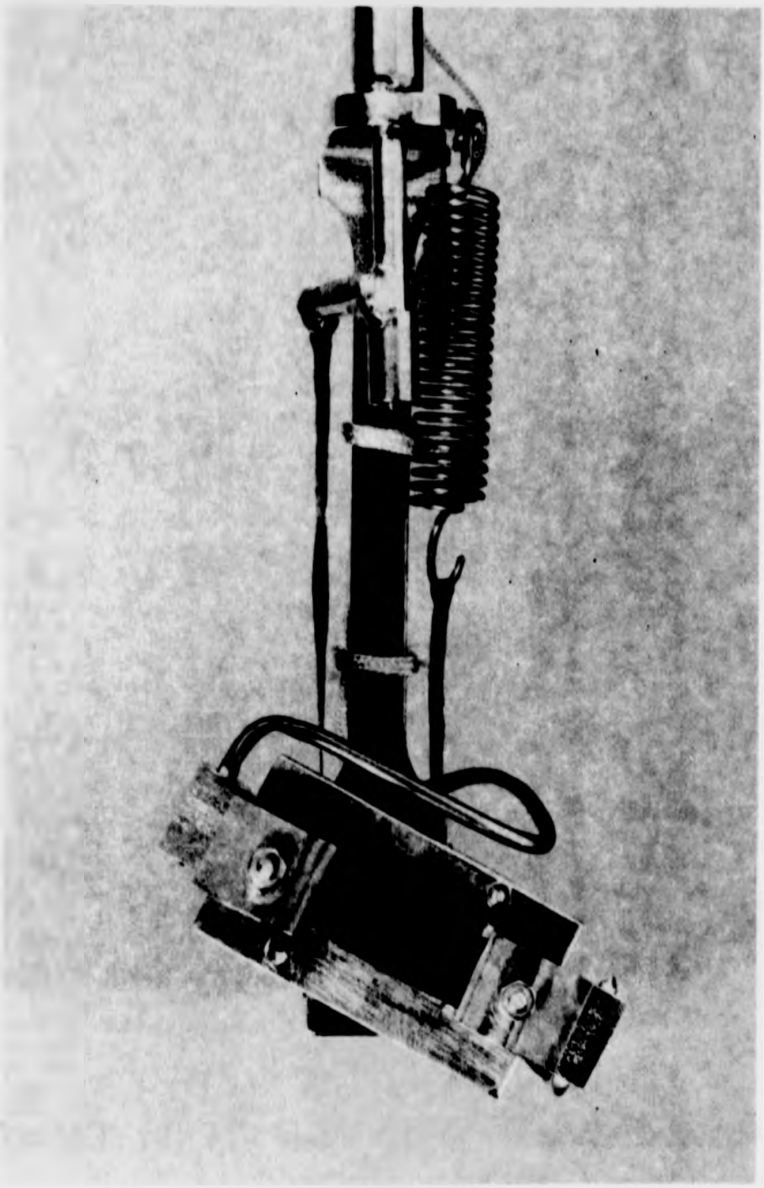

Fig. 2.3 The specimen manipulator and resistive heating stage with Si(100) specimen mounted.

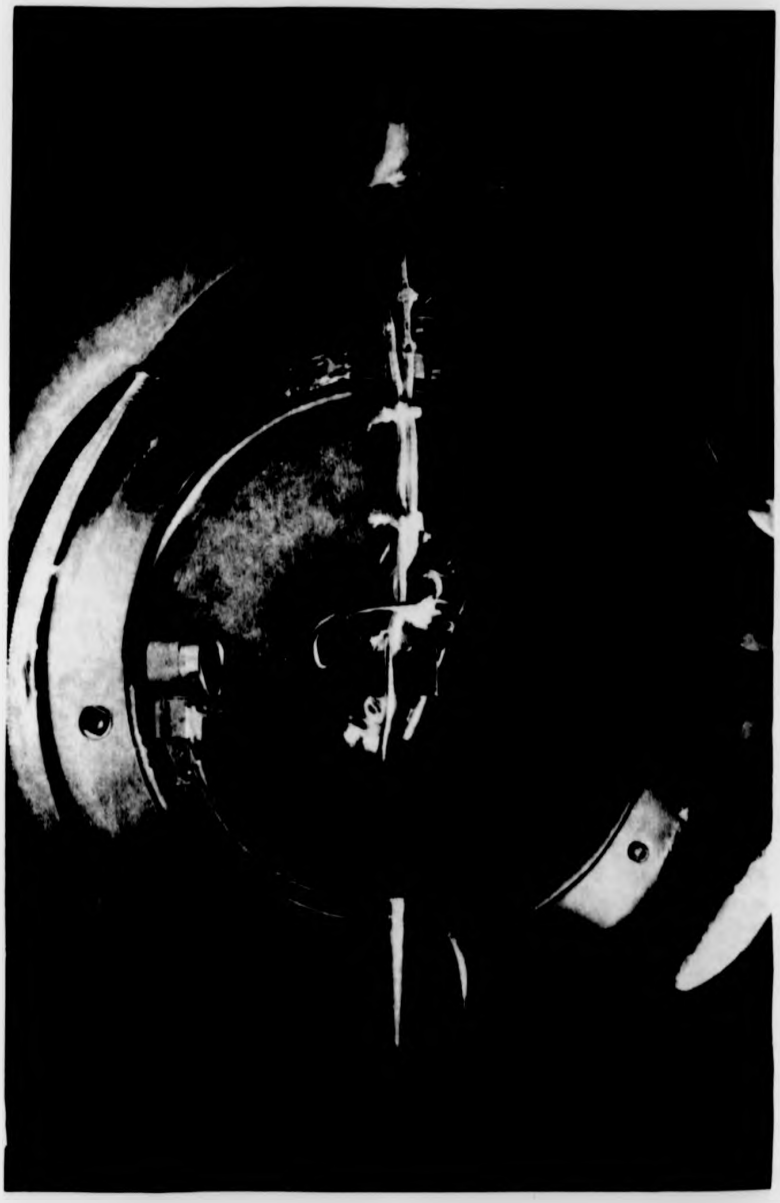

Fig. 2.4 View of the interior of the main vacuum chamber, looking towards the LEED optics. The specimen manipulator is visible at the centre of the figure, the Faraday cup to the left.

$HF/HNO_3/H_2SO_4$ mixture to etch the surface followed by boiling in distilled water to remove any surface fluoride. The tantalum sheet was then outgassed by heating in vacuum to 800 °C - 900 °C for several minutes.

The specimen manipulator is a 'V.G.' type UMD2; allowing a wide range of specimen positions.. Adjustment was accomplished by means of external screw adjustments, communicated to the specimen via three sets of stainless steel bellows. The external adjustment mechanism is visible in Fig. 2.1, the lower end of the manipulator, carrying the specimen mount, in Figs. 2.3 and 2.4. The specimen can be translated in any direction, and may be tilted both 'fore and aft' and from side-to-side. Rotation of the specimen is possible, about an axis parallel to the surface, over a full 360° for angle of incidence adjustment; and about an axis perpendicular to the surface, for azimuthal-angle variation, over a range of ~120°.

IV. The LEED System

The LEED Optics and Faraday cup is shown in Fig. 2.4. and schematically in Fig. 2.5. This system has been described in detail elsewhere [51], so we will confine ourselves to an outline of the main points of this arrangement.

IVi. The Electron Gun

The electron gun used for LEED is a 'V.G.' LEG2, which points toward the specimen, through the centre of the LEED optics in the conventional arrangement. This gun produces a well-collimated beam of electrons, with a spot diameter of approximately 1 mm at the specimen

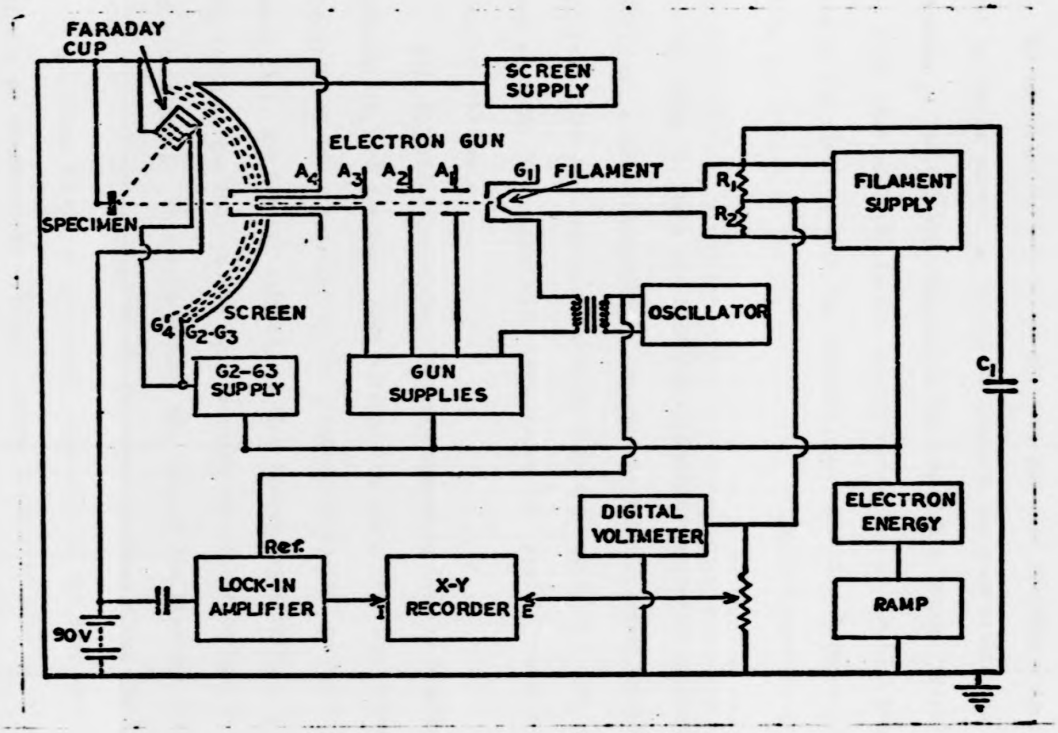

Fig. 2.5 Schematic diagram of the LEED system.

surface. The beam current is 0.6 - 2 μA, and is relatively constant with respect to energy above ~60 eV.

An important feature of an electron gun used for LEED work is that it should have a low spread of electron energies within the beam. A number of factors are responsible for the finite energy 'width' of the beam; they are principally, energy spread due to the high temperature of the electron emitting filament, the variation in potential along the portion of the (directly heated) filament'imaged' by the gun, and any ripple or variation in voltage of the power supplies used.

In order to limit the filament temperature necessary to produce sufficient electron emission, a low-work function filament material is required. The LEG2 employs a rhenium filament coated with LaB_6 which runs at ~1300 °C compared with temperatures of ~2200 °C required for tungsten filaments.

Fig. 2.5 illustrates the filament mounted inside the Wehnelt cylinder (G_1) of the gun. When running the gun a positive extraction potential of 600 V relative to the filament is applied to the first anode (A_1), the Wehnelt cylinder is then biased negatively to 'pinch' the field at the hole in the can, reducing the effective imaged area of the filament. This both reduces the size of the beam and limits energy broadening produced by the potential gradient along the filament.

The third factor in the energy resolution of the gun, that of the ripple on power-supply voltages, proves to be difficult to solve. The arrangement of the electronics used for LEED is shown in Fig. 2.5. It will be noted that in order to maintain the final anode of the gun

at earth potential the filament power supply must be 'floated' to produce the required electron energy. This results in the production of a large mains-frequency ripple on the filament voltage. The normal method of eliminating such noise would be to simply connect a capacitor (C_1) as shown in the figure. If this capacitance is too large, however, a time constant is introduced which limits the slewing rate of the electron energy. A compromise is reached therefore whereby the ripple is reduced but the rate of change of the energy is fast enough to allow rapid data collection.

These precautions ensure that the electron beam has a satisfactory energy width suitable for accurate LEED work; the energy spread is estimated to be $\leq$ 0.3 eV.

IVii. The Electron Optics

The LEED optics is a standard 'V.G.' 3-grid system, subtending an angle of ~120° at the specimen surface. The grids G_2 and G_3 form a retarding field energy analyser; they are strapped together for improved resolution, and for LEED are held at a potential close to that of the electron energy. Grid G_4 is at earth potential, as is the specimen and A_4, the final anode of the electron gun; maintaining an electric field free-space between the specimen and the analyser, and avoiding perturbation of the electron trajectories. In operation, electrons of a given energy from the gun, impinging on the specimen, are diffracted at the surface and traverse this space to G_2 and G_3, where (subject to the resolution of the grid system) all but the elastically scattered electrons are rejected. The elastic component passes through the grids

and is accelerated by the high potential (5-7 kV) applied to the screen. Striking the phosphor at high energy these electrons produce the characteristic LEED pattern.

IViii. The Faraday Cup

The Faraday cup consists of 3 grids and a collector; the grids being connected in exactly the same way as the corresponding grids in the full-size optics. The collector is simply an insulated plate, coated with "Woolly Soot" [52] a material known to have a low secondary emission coefficient; a potential of 90 V is applied to this collector to further reduce secondary emission. The cup is capable of rotation over an arc of 330° in the horizontal plane, the remainder of the arc being blocked by the final anode structure of the LEED gun; thus the minimum angle of incidence for (00) beam data is ~8°. The cup may be used to collect diffracted electrons in the (00) beam in any azimuth by adjustment of the specimen azimuthal orientation, or nonspecular beams in the plane of incidence of the electron beam. The angle subtended at the specimen surface by the cup aperture is ~7°, a solid angle of ~0.01 ster.; its energy resolution is approximately 1% [51].

The Faraday cup may also be used to study the angular dependence of Auger electron emission, work described in Chapter Four.

V. Power Supplies and Electron Detection System

The arrangement of the power supplies and other electronics for the LEED system is illustrated in Fig. 2.5. The electron gun filament is powered by a stabilised supply which is 'floated' to produce the

required electron electron energy; a 'J & P' programmable supply controlled by a variable speed ramp unit provides the HT voltage. HT supplies for the other anodes in the gun are provided from other stabilised units and are variable by means of multiturn potentiometers. A pair of identical resistors (R_1 and R_2), in series across the gun filament enable the potential to be measured at a simulated 'centre-tap,' thus providing a direct reading of the electron energy on a digital voltmeter; the voltage is also fed, via an attenuator (VR_1), to the X-axis of an XY potentiometric recorder.

In order to make possible more rapid data collection it was found desirable to operate the LEED system in a 'chopping' mode. By applying an oscillating potential to the Wehnelt cylinder of the electron gun the beam can be 'chopped' as the field at the hole in the can goes through the 'pinch-off' condition when no electrons can emerge; the intensity in the diffracted beam is then modulated and the signal can be detected and amplified using a 'Brookdeal' Lock-In Amplifier. This provides a method of handling the small signals involved ($\leq 10^{-8}$ A) without increasing the time constant of the data collection system. The output from the Lock-In Amplifier is fed to the Y-axis of the XY recorder; Intensity-Energy spectra may be plotted by ramping the electron energy and recording energy and intensity directly.

VI. The On-Line Computer Facility

In the late stages of this work an on-line computer was brought into operation. The system consists of a 'GEC' 4080 processor, together

with a disc file unit and lineprinter. The provision of an interface unit, consisting of multichannel analogue-to-digital (a/d) and digital-to-analogue (d/a) converters enables the system to control several simultaneous experiments remotely by programmed instruction. A schematic diagram of the system is shown in Fig. 2.6.

This facility offers the possibility of speeding up LEED data processing considerably. Intensity-Energy spectra can be plotted under computer control and the results stored. The profiles can then be easily manipulated in digital form, eliminating the necessity of digitising the curves by hand.

This was only possible for the (00) beam plots, however, which involved simply positioning the specimen and the Faraday cup by hand and then ramping the electron energy to produce a LEED spectrum. Non-specular beams required changes in cup position and repeated scans over limited energy ranges and could not be accommodated at this stage. The system was used only for (00) beam spectra for the (1 x 1)H structure.

The d/a converter provides a signal of from -10 V to + 10 V in a total of ~2000 steps under instruction from the processor. The range from 0 to 10 V only was used to provide the ramp voltage controlling the 'J & P' HT unit which supplied the electron energy. In order to limit the storage area per profile required only alternate steps were used for the high energy range where features are broader and resolution requirements are less critical. Suitable programming permitted variation of the ramp speed, with fast scans for setting up purposes and lower rates for data collection.

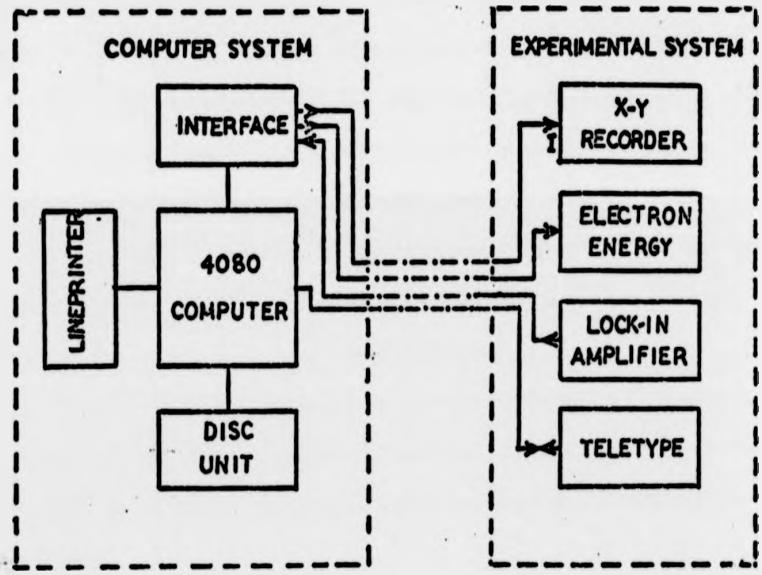

Fig. 2.6 Schematic diagram of the on-line computer system.

Intensity values were input to the computer via the a/d converter. This unit has the capability of accepting analogue voltage signals from -10 V to +10V, these are converted into digital signals with ~2000 increments covering the voltage range. Again only the positive range was used. The output of the Lock-In amplifier was adjusted to approximately 'fill' this range for optimum resolution. In order to improve the intensity scale resolution for the smaller, high-energy peaks a simple operational amplifier was added to the Lock-In output. This unit had variable gain, with values x1, x10 and x100.

Monitoring of intensity values recorded by the computer was carried out using a second channel of the d/a converter, the digital values of intensity going into storage were reconverted into analogue signals. The Intensity-Energy profile could then be plotted simultaneously on the XY recorder as a check that the data collection was proceeding correctly. The energy scale was obtained as described previously.

Commands to the processor and output messages were handled by a 'Teletype' unit at the experimental location.

VII. Magnetic Field Neutralisation

In order to perform accurate LEED and AES work it is important that there should be minimal stray magnetic fields present, resulting either from the earth's field or produced by the powerful magnet of the ion pump. These fields were neutralised by means of 3 mutually perpendicular, square 'Helmholtz' coils. These coils are visible in Fig. 2.1, surrounding the apparatus.

PART B: SETTING UP PROCEDURES AND EXPERIMENTAL ACCURACY

Before performing LEED experiments it was necessary to go through certain procedures in order to ensure that the system was set up correctly so as to yield accurate results.

In the remainder of the chapter we will describe these operations, and discuss the accuracy of the results to be presented later in this work.

I. Focussing of the Electron Gun

Focussing of the LEED gun was accomplished by adjustment of the potentials on Anodes A_2 and A_3 to produce a beam which was well focussed over the energy range 20 - 600 eV. Some broadening of the beam below 30 eV was still observed at the optimum focus condition; this was not considered serious in view of the large acceptance angle of the Faraday cup and the limited success of magnetic field neutralisation in this region. Data below 30 eV should therefore be treated with some reserve. For similar reasons all data below 20 eV has been rejected.

II. Magnetic Field Neutralisation

Neutralisation of stray magnetic fields was carried out in two stages. Initial settings of the power supplies providing current for the 'Helmholtz' coils were made by observation of the spot produced by the (00) beam through a telescope until virtually no movement of the beam could be detected down to an energy of 20 eV. The second

stage of neutralisation used a 'self-consistent' process to ensure that LEED (00) Beam Spectra were essentially identical from either side of the specimen surface normal, as predicted by the crystal symmetry for this surface. I-V Spectra were first taken from either side of the normal (i.e., positive and negative angles of incidence) in order to determine the approximate normal incidence position. Spectra for nominally equal angles (~10°) were then plotted over a range 20-380 eV and the magnetic field compensation trimmed to produce good agreement of the curves, with readjustment of the normal incidence position as necessary. In this process particular attention was paid to the postions of peaks on the energy scale, since this was regarded as the most important criterion of accuracy in angle of incidence over a wide range of energy. Certain differences of relative intensities present at low energy were ignored when peak positions and the general shape of features showed good agreement. A check of the similarity of curves at different angles of incidence (e.g., ~30°) completed the neutralisation procedure and the currents required to produce the correct compensating field were noted.

III. The Grid Bias Setting

The energy resolution of the LEED system is determined by the potential applied to the energy analysing grids G_2/G_3 in the LEED optics and within the Faraday cup. In order to allow for certain irregularities and misalignments of the Faraday cup it was found necessary to set G_2/G_3 a few volts positive of the electron energy to obtain

reproducible LEED spectra. This increases the energy 'bandwidth' accepted by the analyser; thus LEED beams detected contain elastically scattered electrons, together with a proportion that have undergone certain inelastic events. In order to limit the inelastic component the value of the bias applied to G_2/G_3 (i.e., the additional positive voltage superimposed on the electron potential) was selected on the basis of the electron energy loss spectrum obtained from silicon; this distribution is shown in Fig. 2.7. The loss spectrum was obtained by plotting the total secondary electron distribution N(E). The elastic peak at the primary energy is 'followed' on the low energy side by a series of discrete loss peaks. The large peaks in the figure are produced by electrons which have lost discrete amounts of energy creating bulk or surface plasmons.

The bias applied to grids G_2/G_3 for LEED work was chosen to be +4 V, which lies in the minimum between the elastic peak and the first plasmon peak. Inelastic electrons passed by the analyser will include those which have undergone phonon scattering, often referred to as the quasi-elastic component, together with those which have lost energy by generation of interband transitions; the promotion of electrons from the valence band into the conduction band, leaving a 'hole' behind (this process is sometimes called pair production). No electrons which have undergone plasmon processes will be accepted.

IV. Alignment of the Specimen

It was discovered in this work that there were certain misalignments in both the Faraday cup and the specimen manipulator. We will discuss

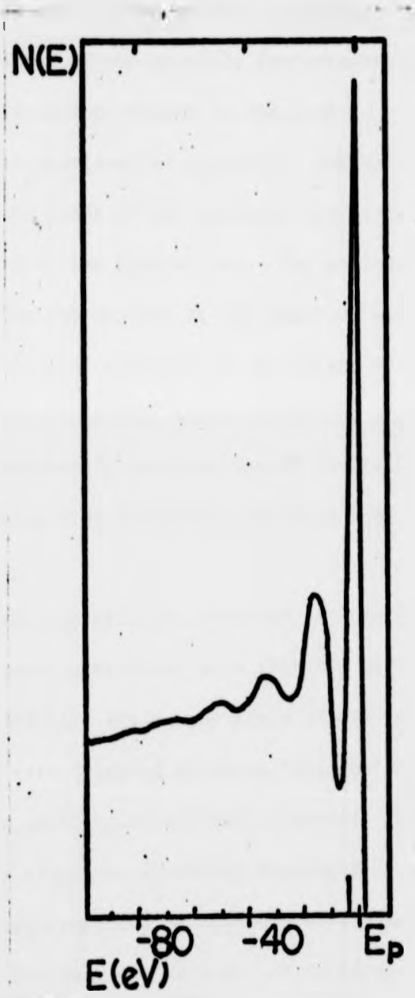

Fig. 2.7 Electron energy loss spectrum from the clean Si(100)(2 x 1) surface.

these misalignments, and the methods adopted to minimise their effect; with an examination of the possible inaccuracies in the experimental data resulting from such errors as remained.

In an ideal experimental situation, the specimen axis of rotation should lie in the plane of the specimen surface and be coaxial with the axis of rotation of the Faraday cup. The electron beam from the LEED gun should strike the surface at the point of intersection of this axis with the plane of rotation of the centre of the Faraday cup.

In practice, of course, these conditions are only partly realised, owing to difficulties in construction of the rather complex apparatus, distortion arising from successive bakeouts (and in some cases, simply poor design).

The specimen manipulator presented certain problems since it was impossible to mount a specimen such that the axis of rotation for angle of incidence variation lay in the plane of the surface. Specimen heating stages were designed to be as 'shallow' as possible; the specimen surface was still ~2 mm off axis, however. This displacement, together with a slight eccentricity displayed in the rotation of the manipulator itself, resulted in movement of the incident beam across the surface of the specimen as the angle of incidence was changed. It was therefore necessary to ensure that the surface area of the specimen was as large as possible, and that the specimen remained flat following heat treatment; so that there could be no change in angle of incidence resulting from distortion of the surface. These requirements were satisfied by using specimens of length ~2 cm and width ~1 cm, and by

checks on the flatness of the specimen. These checks were made by observing the LEED pattern as the specimen was translated perpendicular to the incident beam, any movement of the LEED spots indicated a distortion in the specimen surface.

Certain difficulties were encountered when conducting LEED experiments, owing to the above-mentioned misalignment. On some occasions it was found that the areas of good surface order were relatively small, though still larger than the beam diameter. Movement of the beam across the surface resulted in areas of poor order being encountered; in these cases it was necessary to translate the specimen so that the beam impinged on a more ordered area.

The position of the specimen was adjusted so that the axes of rotation of specimen and Faraday cup were coincident, to the degree which could be assessed by eye. Error resulting from any remaining misalignment produces a small change in the energy resolution of the Faraday cup as its position is changed since the diffracted beams enter the cup at an angle to the retarding grids. This effect was considered to be small in practice.

The procedure established to check field neutralisation and alignment; namely that of recording I-V spectra for equivalent angles of incidence on either side of the surface normal, was carried out regularly to establish the normal incidence position for each azimuth used. This routine was considered to be a good verification of the settings established above; and the almost identical nature of these curves confirmed the adequacy of the alignment measures adopted.

Fig. 2.8 illustrates the definition of angles used in this study. θ is the angle of incidence, ϕ the azimuthal angle, defined with respect to some direction in the crystal surface plane. Here $\phi = 0$ corresponds to the <110> direction in the crystal.

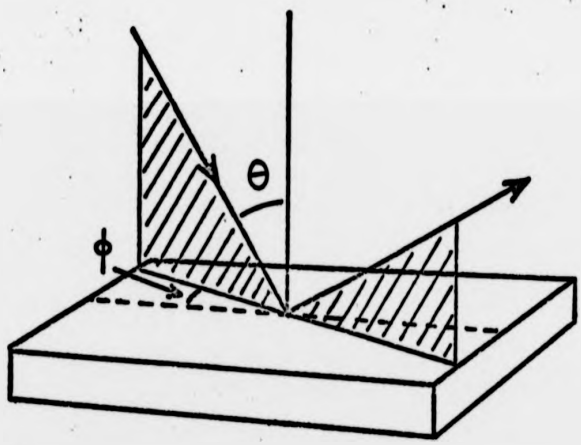

Fig. 2.8 Definition of angles of incidence (θ) and azimuth (ϕ).

CHAPTER THREE

AUGER ELECTRON SPECTROSCOPY AND SPECIMEN CLEANING

PART A: AUGER ELECTRON SPECTROSCOPY (AES)

The Auger effect [53] was first discovered in 1925 by Pierre Auger [54], from studies of cloud chamber tracks. J. J. Lander [55] was the first to suggest the use of Auger electrons as a spectroscopic tool, though the value of the technique for surface analysis was not appreciated until 1968 when Harris [14] used electronic differentiation to enhance the Auger peaks. The use of AES as an adjunct to LEED was demonstrated by Scheibner and Tharp [12] and Weber and Peria [13]. All that was required to perform AES was to modify the 2-grid LEED optics by adding a third, and sometimes a fourth grid together with some electronics external to the vacuum system.

I. The Auger Process

Fig. 3.1 illustrates the energy level structure for an atom in a solid (in this case silicon). If a beam of primary electrons is incident on the solid, a core level, here the $L_{2,3}$ level, may be ionised. This leaves a 'hole' into which one of the outer electrons may drop. The energy given up in this transition may then be emitted as a photon, or, in an Auger process, be given to another electron which is ejected from the solid with an energy characteristic of the original transition. The atom is left doubly ionized, changing the energy levels shown in the diagram. The energy of the emitted Auger electron is given by:

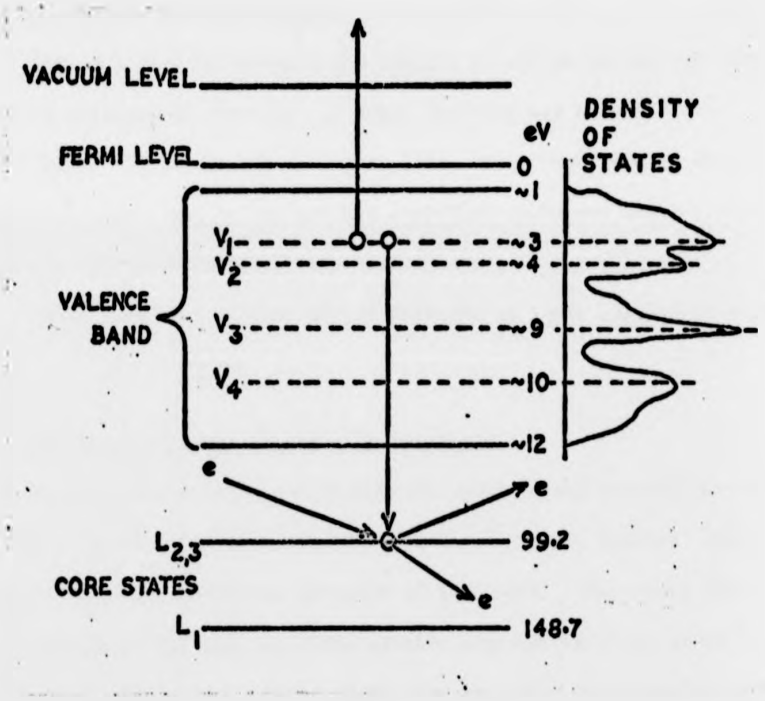

Fig. 3.1 Energy level structure for a silicon crystal, and $L_{2,3}V_1V_1$ Auger transition.

$$E = E_{L_{2,3}} - E_{V_1} - E_{V_1'} .$$

$E_{V_1'}$, is the V_1 ionisation level for the atom in some ionised state, a correction to the normal energy level must be applied to allow for the effective extra positive charge.

Fig. 3.1 also illustrates the density of states within the valence band of silicon; in practice the Auger spectrum may be some self-convolution of the density of states [56], since there are no strict selection rules, and in the process described above any other electron from the valence band could have been ejected.

Impurities on a surface may be detected by their characteristic Auger electron emission.

II. Experimental Auger Electron Spectroscopy

Auger electron energies have been calculated using a modified version of the formula above or estimated from X-ray tables; however there is little formal justification for much of this work. The use of AES as a surface analysis tool therefore usually proceeds by observation of empirically determined sets of peaks from the different elements present. A catalogue of such empirical spectra has been compiled [57], and proves very useful in this connection.

Quantitative estimates of impurity levels based on AES are difficult since the efficiency of the Auger process for a given element depends on a number of factors; the most important being the ionisation cross-section for the inner shell, the X-ray fluorescence yield (a small effect in the 0 eV - 500 eV range [58]), and the escape depth for

electrons of the Auger energy in the solid being studied (typically 3Å - 30Å for Auger electrons $\lesssim$ 500 eV). Calibrations have been made (e.g., [59-61]) which indicate that peak size is roughly proportional to concentration, especially at coverages below one monolayer.

The energy of the exciting beam required is determined by the ionisation energy of the initial core level E_W. It is found that a primary energy of ~3 E_W produces maximum yields [58,59].

The use of AES in surface analysis has been discussed in review by Chang [62]. Auger Electron Spectroscopy is also finding uses in studies of the nature of chemical bonding at surfaces by examination of 'chemical shifts' of Auger peaks, and observations have been made of the change in shape of Auger peaks according to the chemical state of the element under consideration [63]. Another important application of the Auger emission process is its use in 'microscopes' with high spatial resolution, as a tool in surface diffusion and segregation studies (e.g., [64]).

III. Electronic Detection

Auger electron detection may be performed using a retarding field analyser, as in the LEED-Auger system, or by means of a dispersive analyser such as the Cylindrical Mirror.

Auger electron currents are typically ~10^{-5} of the incident beam [62] (~10^{-9} A, for a typical beam current of 100 μA). In order to analyse and detect these small currents an oscillating component $\Delta E = k \sin \omega t$ is superimposed on the analysing potential; the signal I(E)

arriving at the collector is then modulated with respect to energy (E), and we can write the Taylor Series expansion for this current

$$I(E + \Delta E) = I(E) + I'(E)\Delta E + \frac{I''(E)\Delta E^2}{2} + \frac{I'''(E)\Delta E^3}{3!} + \frac{I''''(E)\Delta E^4}{4!} + \ldots$$

where the prime denotes differentiation with respect to E.

Thus we see that:

$$I = I_0 + [I'k + \frac{I'''k^3}{8} + \ldots] \sin \omega t - [\frac{I''k^2}{4} + \frac{I''''k^4}{48} + \ldots] \cos 2\omega t + \ldots$$

which for small modulation amplitude k, reduces to:

$$I = I_0 + I'k \sin \omega t + \frac{I''k^2}{4} \cos 2\omega t + \ldots .$$

The coefficient of the term at the fundamental frequency is $I'(E)k$, that of the 2ω term $I''(E)(k^2/4)$.

In the case of the LEED-Auger retarding field analyser, the collected current is the integral of the secondary electron distribution, i.e.:

$$I(E) = \int N(E)dE.$$

Thus, if a Lock-In Amplifier is used to detect the signal, tuning in to the 2nd-harmonic gives the derivative of the energy distribution $N'(E)$, the spectrum most commonly used since Auger peaks then stand out clearly from the background. A convention has been adopted by most workers for labelling of these derivative-form peaks; the energy of the 'peak' is defined by the position of its high-energy minimum.

IV. The Auger Electron Spectrum of Silicon

The Auger spectra from (111) and (100) surfaces of silicon are essentially identical, and it now seems clear that most or all of the peaks can be attributed to silicon, though this point has been the cause of some continuing controversy.

Some early AES studies of silicon were made by Bishop and Riviere [65] and Taylor [66]; since then most LEED experiments on silicon have included AES. Detailed studies of the silicon spectrum have been made [56,65-68], and we will summarise the results of that work below.

A typical Auger Electron spectrum from 'clean' silicon, observed by the author, is shown in Fig. 3.2. It is characterised by a large peak at 92 eV, and a series of smaller peaks at 107 eV, 83 eV, 74 eV, 57 eV, 44 eV, and 34 eV (not in figure), very small peaks are sometimes observed at 135 eV and 165 eV. Most workers have observed this set of transitions, though some refer to them by different energy 'labels' (e.g., [56,66,67]). The high energy series of peaks (~1 kV) have not been studied in detail. The peak at ~272 eV in the spectrum is due to a small amount of carbon on the surface.

The relative sizes of the low energy peaks often differ between specimens and seem to depend on the prior cleaning of the sample; dependence on the state of order of the surface also seems likely following the work of Grant and Haas on carbon [63]. An oxide layer on the surface produces a reduction in the 92 eV peak, with large peaks appearing at 78 eV and 65 eV due to silicon atoms in the oxide [61].

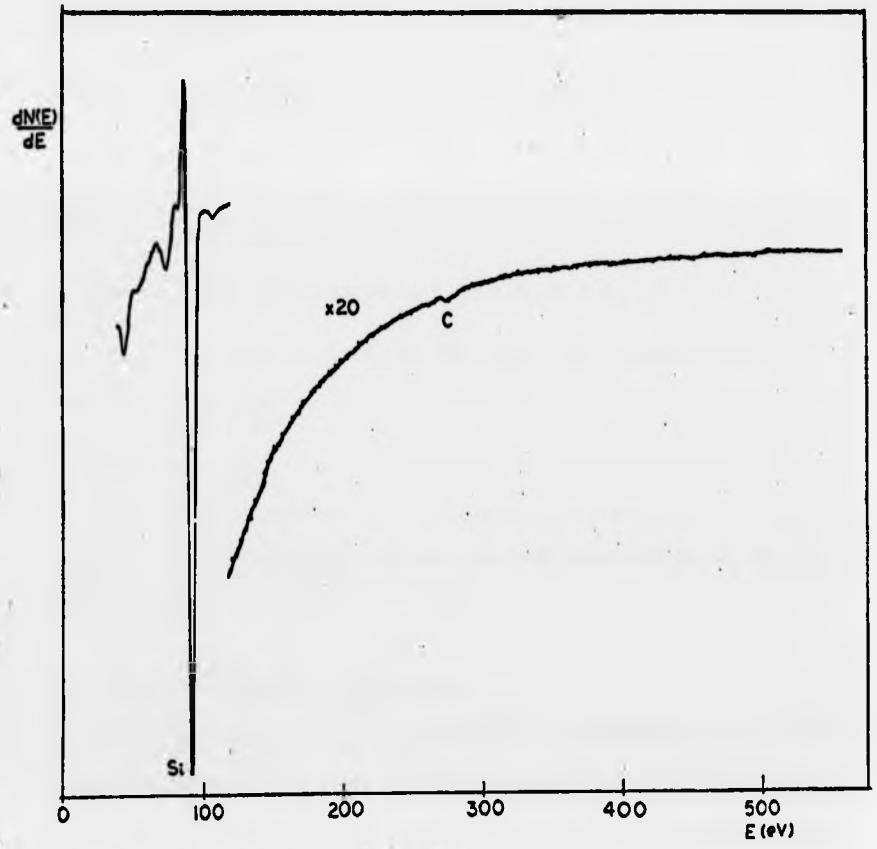

Fig. 3.2 Auger spectrum of the 'clean' Si(100)(2 x 1) surface.

The table below summarises the Low Energy Auger electron peaks from clean silicon and the transitions to which they have been attributed (refer to Fig. 3.1).

Peak	Transition
135 eV	$L_1V_1V_1$
107 eV	Auger process in atom already singly ionized or plasmon gain from 92 eV peak
92 eV	$L_{2,3}V_1V_1$
83 eV	$L_{2,3}V_3V_3$ or ionisation and surface plasmon loss from 92 eV peak
74 eV	Mainly bulk plasmon loss from 92 eV - $L_{2,3}V_4V_4$
57 eV	Impurity, Cu or Ni or 2nd order bulk plasmon loss.
44 eV	$L_1L_{2,3}V_1$
34 eV	$L_1L_{2,3}V_4$

The bulk plasmon energy in silicon has been measured at 17 eV, the surface plasmon energy at 12 eV [68].

V. AES: Experimental Arrangement

Fig. 3.3 illustrates the experimental arrangement used to perform Auger electron analysis. The primary beam is supplied by a 'Superior Electronics' SE 3K 5U Electron Gun with an indirectly heated oxide cathode. This gun is capable of producing a beam current of up to 100 μA at 1.5 keV, into a spot of ~1/2 mm in diameter. The gun is mounted in such a way that the beam strikes the specimen at glancing

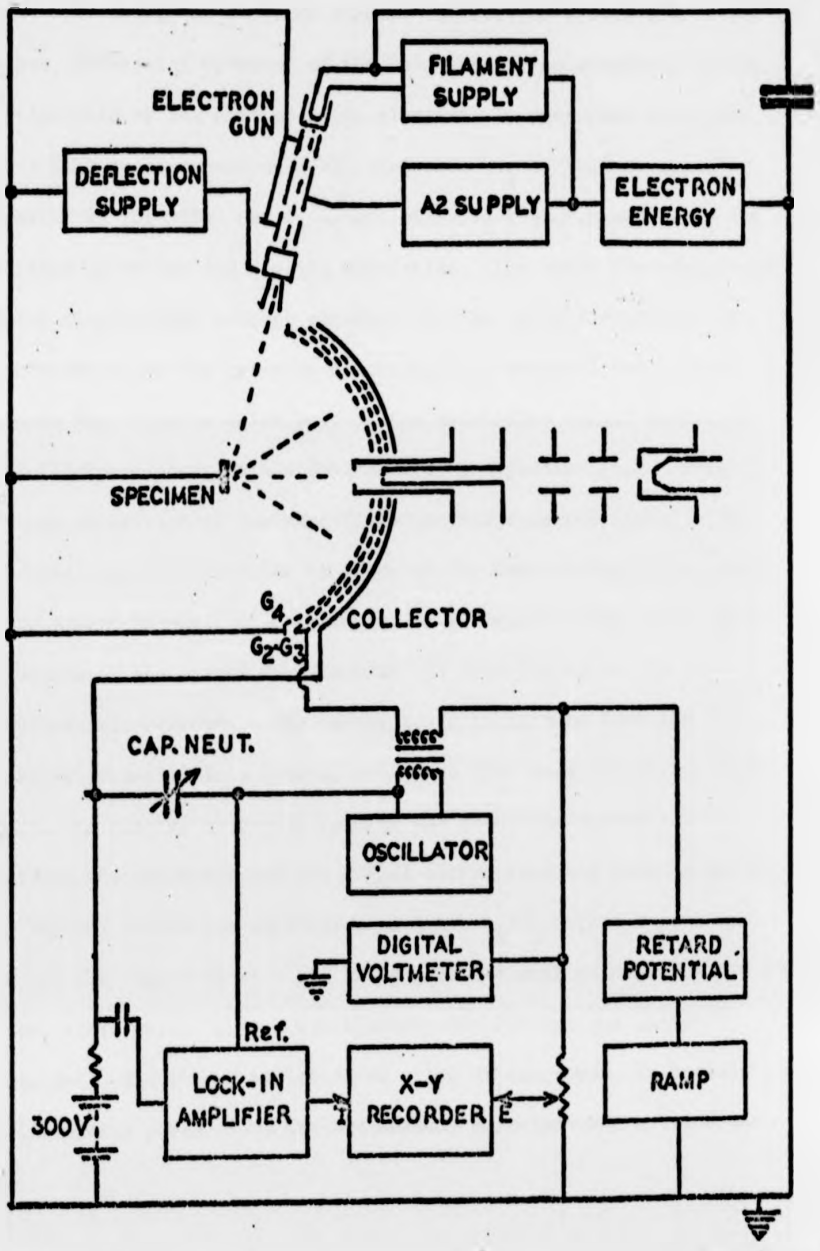

Fig. 3.3 Schematic diagram of the Auger electron spectroscopy system.

angle, increasing the detected volume. Deflection plates are fitted to the gun, permitting movement of the beam across the specimen surface.

Analysis of the emitted Auger electrons is performed using the 3-grid LEED-Auger retarding field analyser. G_4 is held at earth potential as for LEED and G_2/G_3 are strapped together and carry the retarding potential and applied modulation. The large capacitatively coupled displacement current generated in the collector circuit by the modulation on the grids is neutralised by means of the circuit shown in Fig. 3.3; in which part of the modulation signal is fed to the collector circuit, via a phase-shifting capacitor [51]. This prevents saturation of the amplifiers by this unwanted signal. The collected signal is detected by means of the Lock-In Amplifier tuned to the second harmonic of the modulation frequency. The output (the derivative of the energy distribution) is then fed to an XY-potentiometric recorder. The energy scale is derived from the retarding potential in a similar manner to that used for LEED. Auger spectra are plotted by simply ramping the retarding potential; recording the potential and the signal output from the Lock-In Amplifier.

Typical modulation amplitudes on Grids G_2/G_3 were 5 V peak to peak for the region 40 eV - 120 eV, and 12.5 V peak to peak for 120 eV - 530 eV; these values gave a satisfactory sensitivity and energy resolution. The energy region 40 eV - 530 eV was chosen to include the low-energy peaks of all the contaminants expected on a silicon surface.

The signal-to-noise ratio of the system is limited by Shot Noise, originating in the electron gun [62]; the sensitivity for contaminants, in terms of detectable peak heights relative to the main silicon 92 eV peak (allowing for the different modulation amplitudes used), was an effective minimum peak height ratio of $\leq 1 \times 10^{-3}$.

PART B: CLEANING SILICON SURFACES

I. Review

Ii. Chemical Treatment

A variety of chemical treatments have been used to clean silicon surfaces prior to ultrahigh vacuum experiments. One of the most common approaches is the use of HF/HNO_3 mixtures, to etch the surface and remove contaminated and damaged layers [1,2]. Another method involves the use of Iodine solutions after etching [61,69-71], this is claimed to produce a protective layer of Iodine on the surface. Following Reflection High Energy Electron Diffraction (RHEED) work, in which he identified carbide precipitates on silicon surfaces after heating in ultrahigh vacuum, Henderson *et al.* [72-74] showed that etching with HF, by leaving a highly reactive surface exposed to the air could result in relatively high carbon levels. He therefore proposed a 'peroxide' cleaning scheme [74] designed to produce a clean oxide layer (SiO_2, 13Å - 15Å thick) on the silicon surface, and low carbon concentrations following ultrahigh vacuum heating.

Iii. Vacuum Treatment

The principal contaminants found on silicon surfaces in ultrahigh vacuum experiments are oxygen and carbon. It has been found that oxygen can be removed relatively easily by heating in vacuum [12,61] at temperatures from 700 °C to 1200 °C. Light oxidation, in most cases, has simply reduced the intensity of the diffracted beams and increased background intensity, no ordered oxygen structures have been observed. However it has been reported [2,75] that oxidation reduces the intensity of 1/2 order spots in the (2 x 1) pattern (producing a structure which might be described as a mixture of (2 x 1) and (1 x 1) superstructures).

Carbon contamination has proved difficult to remove, a number of workers [61,72,73,76-78] have detected the formation of cubic silicon carbide (β - SiC) on the surface of silicon slices heated to 800 °C - 900 °C with residual carbon contamination. These crystallites cannot be observed directly by LEED, but may be studied using RHEED, and have been found to exist on some surfaces exhibiting (100) (2 x 1) and (111) (7 x 7) structures.

It is normally considered that carbon contamination arises from decomposition of carbon containing adsorbates on the surface rather than from diffusion from the bulk. The mechanism for carbide formation which has been proposed [76] is as follows. Heating to 800 °C - 900 °C decomposes carbon-containing adsorbates and produces a situation in which the carbon concentration in the bulk and surface layers exceeds the solid solubility limits at the surface. Silicon carbide then precipitates out, forming crystallites at preferred sites.

It has been reported [61,69,76] that heating the surface to ~1200 °C - ~1300 °C reduces the carbon significantly, believed to be by solution in the bulk material since at this temperature all surface carbon is expected to be in the form of silicon carbide and would not be expected to evaporate [51,79]. Chang [61] has produced carbon concentrations which he estimates, from Auger analyses, at 2 x 10^{13} atoms/cm^2 (1/4 monolayer if all the carbon is at the surface). Carbide crystallites have also been removed by heating in this temperature range [76], but a pitted surface may be produced due to thermal etching [80]. Henderson [74], using the 'peroxide' cleaning treatment simply heated the specimen thus prepared to 900 °C - 1100 °C for ~10^3 secs. in ultrahigh vacuum, producing a relatively carbon-free surface.

Other contaminants on silicon surfaces are principally metals, present in the bulk and diffusing to the surface on heating. High temperature annealing (> 1000 °C) has been observed to increase the concentration of metals at the surface [61]; principally Cr, Mn, Fe, Co, Ni, Cu, and Zn, also In, Sn, Sb, and Te. The total concentration of such metals was estimated at less than 1/10 of a monolayer if all the contaminants were at the surface.

Argon ion bombardment followed by annealing, often used in cleaning other materials, has been less used for silicon surfaces. Some early work [1,2] used bombardment cleaning and produced similar surface superstructures to those generated by heating alone, but no detailed work including Auger analysis has been performed on argon ion bombarded and annealed surfaces, other than recent work by Ignatiev and Jona [81].

II. Experimental Work

IIi. The Specimens

Specimens were cut from commercial polished silicon slices, supplied by the Plessey Company, Allen Clark Research Centre, Caswell. These slices were claimed to be 'dislocation free' Si(100) polished to within 1° of the (100) plane; n type slices of resistivity 2 to 10 ohm-cm were used.

IIii. Chemical Treatment

The chemical cleaning procedure was one adopted on the recommendation of workers at the Allen Clark Research Centre. This process was developed on the basis of the work by Henderson [74]; and is a 'peroxide' scheme, designed to produce a clean oxide layer on the surface.

The procedure was as follows:

Specimen washed in Iso-propyl Alcohol	
H_2SO_4/H_2O_2	Boil
Distilled water	Rinse
NH_4OH/H_2O_2	Wash
Distilled water	Rinse
Specimen blown dry with nitrogen	

The specimen was immediately mounted in the heating stage and loaded into the vacuum system.

The system was then baked for 24-36 hours at ~250 °C and all filaments to be used were thoroughly outgassed before attempting to clean the specimen.

II. Experimental Work

III. The Specimens

Specimens were cut from commercial polished silicon slices, supplied by the Plessey Company, Allen Clark Research Centre, Caswell. These slices were claimed to be 'dislocation free' Si(100) polished to within 1° of the (100) plane; n type slices of resistivity 2 to 10 ohm-cm were used.

IIII. Chemical Treatment

The chemical cleaning procedure was one adopted on the recommendation of workers at the Allen Clark Research Centre. This process was developed on the basis of the work by Henderson [74]; and is a 'peroxide' scheme, designed to produce a clean oxide layer on the surface.

The procedure was as follows:

Specimen washed in Iso-propyl Alcohol	
H_2SO_4/H_2O_2	Boil
Distilled water	Rinse
NH_4OH/H_2O_2	Wash
Distilled water	Rinse
Specimen blown dry with nitrogen	

The specimen was immediately mounted in the heating stage and loaded into the vacuum system.

The system was then baked for 24-36 hours at ~250 °C and all filaments to be used were thoroughly outgassed before attempting to clean the specimen.

An Auger spectrum from the as-loaded specimen after bakeout is illustrated in Fig. 3.4. The silicon peaks indicate that there is a thick oxide layer present, the 92 eV silicon peak is small, the peaks due to the oxide at 78 eV and 65 eV are enlarged. The oxygen series of peaks is clearly visible at ~507 eV and above, as well as a large peak at ~272 eV, due to carbon in adsorbed CO and hydrocarbons.

Once the system had reached its base pressure (~2 x 10^{-10} Torr) the cleaning procedures were commenced. Considerable difficulty was encountered in producing a clean well-ordered surface; we will therefore describe the various approaches adopted and discuss their inadequacies as a guide to some of the pitfalls which may be encountered by other workers, in the hope that forewarned is forearmed!

IIiii. Cleaning by Heat Treatment

Initial cleaning attempts followed the cleaning procedure most commonly described in the literature (and that adopted by Henderson in conjunction with the peroxide cleaning scheme) i.e., that of simply heating the specimen to 1000 °C - 1200 °C.

The heating stage used in this part of the work was similar in construction to that illustrated in Fig. 2.3, though using tungsten specimen contacts rather than tantalum.

In the early stages the specimen temperature was measured by means of a Chromel-Alumel thermocouple in contact with the back of the specimen. Subsequently temperature measurements were made with an optical pyrometer, corrected for the specimen emissivity and refraction by the viewport. The estimated accuracy of these measurements was ~±20 °C.

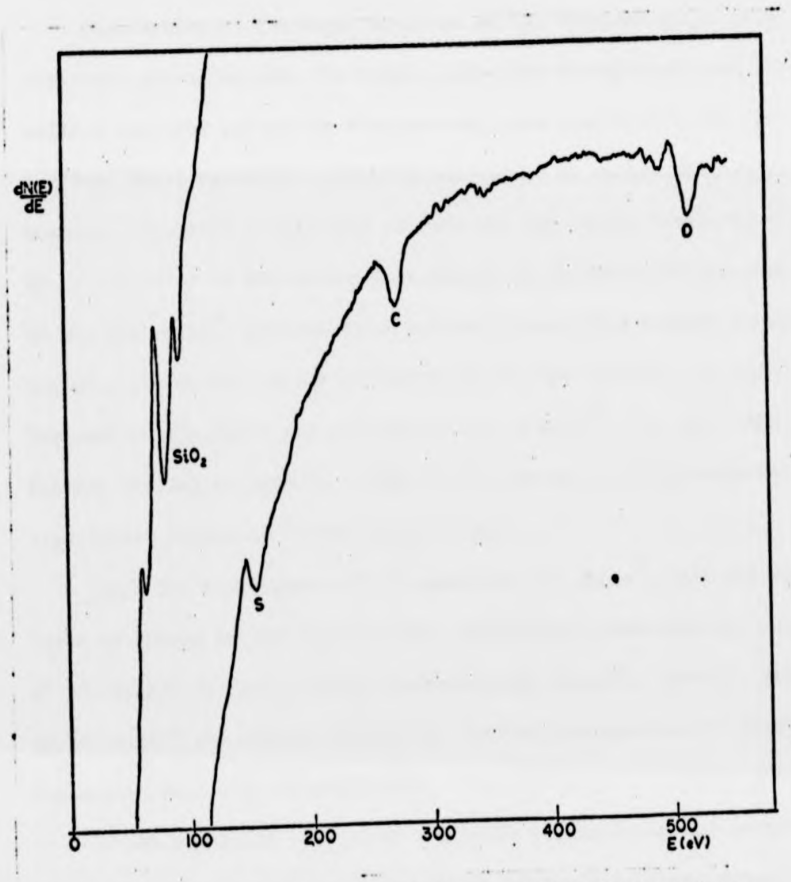

Fig. 3.4 Auger spectrum of the 'as-loaded' Si(100) surface.

The procedure was as follows: the specimen was first partly outgassed by heating to 400 °C - 500 °C for several minutes. The crystal was then heated to ~1000 °C for ~1 min., keeping the temperature in the 800 °C - 900 °C range for no longer than necessary to avoid carbide precipitate formation.

Observation of the Auger spectrum of the specimen after this treatment indicated that the oxygen peaks had disappeared, and the silicon spectrum was of the form normally associated with the 'clean' surface; there was still a significant amount of carbon contamination however. In order to quantify in some way the carbon level, we will quote the ratio of the carbon peak height to the main silicon peak at 92 eV; and we will discuss later to what extent this enables us to estimate the actual carbon concentration at the surface. In this case the peak-height ratio was typically C/Si ~2 x 10^{-2}. It was found that further heating to 1000 °C - 1200 °C for several minutes produced no significant reduction in the carbon level.

Argon ion bombardment of the specimen (~1 $\mu A/cm^2$, ~470 eV) produced no change in the carbon level; though mass spectroscopic analysis of the bombarding gas revealed insignificant impurity levels. Attempts to "burn-off" the carbon deposits by heating the specimen in an oxygen atmosphere were also unsuccessful.

It was concluded that silicon carbide precipitates had formed on the surface, and because of their shape and hardness these deposits resisted ion bombardment.

Another specimen, heated rapidly to 1250 °C and held at that temperature for less than 1 minute, showed a carbon concentration corresponding to an Auger peak-height ratio $C/Si \leq 3 \times 10^{-3}$. It was later discovered that this concentration was regarded by some workers as the typical minimum carbon level regularly achieved [75]. A well-ordered (2 x 1) LEED pattern was observed from the surface. A subsequent cleaning attempt resulted in melting of the specimen at the contacts, however. This was found to be a serious problem which resulted in the destruction of a number of specimens. At the high temperatures necessary to produce a clean surface (1250 °C - 1300 °C; melting point of Si ~1430 °C) the current through the specimen was unstable; modifications to the heating power supply to change its output impedance failed to improve the situation.

Other experiments were performed including the use of electron bombardment heating of the specimen, but because of the relatively low thermal conductivity of silicon it was found to be impossible to heat the specimen to the temperatures required for cleaning without certain 'hot spots' developing, resulting in local melting.

IIiii(a) Thermal Etching. During this work it was observed that heating to 1000 °C - 1300 °C often produced a 'dulling' of the surface of the specimen, those regions which had only attained lower temperatures remaining bright and polished. It was also discovered that in those regions which had attained the highest temperatures (~1250 °C - 1300 °C) the surface 'dulling' was again absent.

LEED patterns from the high temperature annealed 'clear' regions indicated that these areas were well-ordered, patterns from the dull regions were characterized by high background intensities and poorly defined spots, indicating a partly disordered surface.

Auger electron spectroscopic analyses of different regions of the surface showed no significant variation in the carbon concentration of $C/Si \simeq 10^{-2}$.

One of the specimens exhibiting the effect was removed and studied under the 'Stereoscan' scanning electron microscope; the results are illustrated in Fig. 3.5. These photographs show square etch pits in the (100) surface with pyramidal (111) faces, produced by thermal etching of the specimen; similar etching has been reported by other workers [80]. The reason for the nucleation of etch pits is not clear though it may be due to local carbon concentrations whose variation is on a scale too small for detection by the Auger system used here. Absence of etch pits in the highest temperature annealed regions may indicate that in those regions evaporation of silicon from the surface proceeded faster than the thermal etching process.

III. Cleaning by Ion Bombardment

In view of the failure of heat treatment to produce surfaces of the required purity in a reliable manner experiments were conducted using argon ion bombardment cleaning. Ion bombardment was carried out before any heating of the specimen, to remove carbon-containing adsorbates and eliminate carbide formation during subsequent annealing.

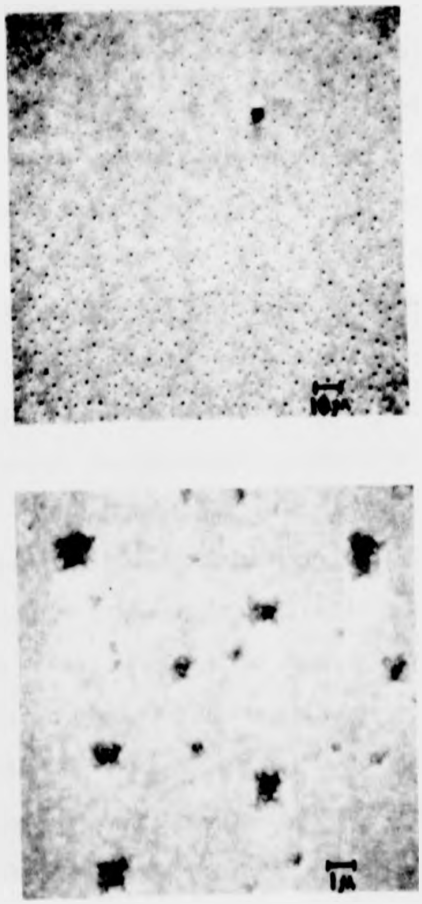

Fig. 3.5 Thermal etch pits on the Si(100) surface.

IIIi. Ion Bombardment Procedure

A new specimen was chemically treated as before and mounted in the heating stage described in Chapter Two.

On attaining the system base pressure and following thorough outgassing of the ion gun the specimen was argon ion bombarded for ~2 hrs. at a current of ~1 $\mu A/cm^2$ and an energy of ~470 eV. Auger spectra following this treatment showed the carbon concentration as $C/Si \simeq 1 \times 10^{-3}$, the only other detectable impurity being argon atoms embedded in the surface. The specimen was then annealed at 500 °C - 600 °C followed by several cycles of similar ion bombardment and heating. Successively higher annealing temperatures were used as the specimen and heating stage outgassed; the low carbon concentration observed initially was maintained and no other contaminants were detected. LEED patterns from the annealed surface showed the familiar form illustrated in Fig. 3.6. The structure is described as (2 x 1), using the Wood Notation [26]; the pattern has four-fold symmetry since two sets of surface domains are present at 90° to each other.

We conclude that argon ion bombardment followed by annealing to 'heal' surface damage is the most suitable method of producing a clean silicon surface, this method was therefore adopted for the work which follows.

IIIii. Surface Order

The annealing temperature required to produce a fully-ordered surface was investigated by means of observation of the LEED pattern and studies of (00) Beam I-V spectra.

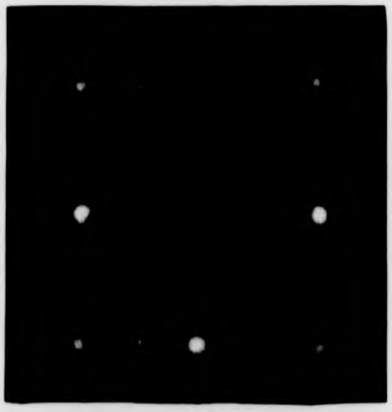

Fig. 3.6 LEED pattern from the clean Si(100) (2 x 1) surface at ~48 eV.

Increasing annealing temperatures were employed in successive bombard/anneal cycles until a temperature was reached which produced no further increase in order after heating for several minutes; i.e., a high intensity LEED pattern with low background and stable I-V spectra. A 'fully-ordered' surface was obtained by heating to ~900 °C for ≈ 10 mins. Subsequent experiments indicated however that the annealing temperature required seemed to depend on the particular specimen used, and other parameters which appeared to be difficult to control. Specimens of similar doping level which underwent essentially identical treatment and showed similarly low impurity levels showed varying behavior with respect to annealing, though in all cases the final stable structures obtained on the fully-annealed surface were identical as evidenced by the I-V spectra.

In some cases, particularly when high annealing temperatures (≥ 1000 °C) were required, thermal etching of the silicon surface was again observed. However, the LEED data to be presented later was all taken from well-ordered regions of the specimen with low-impurity levels.

Partially annealed surfaces resulted in LEED spectra with lower overall intensity. In addition the relative intensities of peaks were modified, as observed by Jona [25]. The resultant intensity profiles were similar to those observed during the intermediate stages of hydrogen adsorption (Chapter Six). The spectra essentially consist of a superposition of diffracted intensities from the bulk structure, observed through disordered areas in the top layer, together

with diffraction from (2 x 1) regions. In the case of partial hydrogen coverage the sum is composed of diffraction from (1 x 1)H regions together with residual areas of (2 x 1) structure.

Similar, though smaller, effects were observed when clean (2 x 1) surfaces were simply left in the vacuum environment. Surfaces exposed to pressures of ~2 x 10^{-10} Torr for periods of in excess of 24 hours, with no incident electron beam, were found to have surfaces which were partially disordered in this way. No additional contamination was detected in Auger spectra taken from these surfaces.

One explanation is that hydrogen adsorption from the ambient atmosphere may produce a partial "reordering" of the surface to the (1 x 1)H form.

IIIiii. Surface Impurity Levels

Impurity levels on fully-annealed surfaces were low. The Auger spectrum of a clean, annealed surface is shown in Fig. 3.2. The silicon series of peaks shows good agreement with results obtained by other workers (as described in Part A). The only peak due to an impurity is the carbon peak at ~272 eV, this is indicative of an impurity level of C/Si $\lesssim$ 2 x 10^{-3}. All other impurities if present have peaks rendered invisible by the signal-to-noise ratio of the Auger system, a peak-height ratio with respect to the silicon 92 eV peak of < 1 x 10^{-3}.

Calibration of Auger peak heights in terms of surface coverage is rather difficult. The usual method employed is to deposit a known coverage of the element under consideration and use the Auger signal

from the adsorbed layer to calibrate spectra for slightly contaminated surfaces. This technique could not be employed in the present study.

We may compare our results with those of Chang [61]. After heating to 1250 °C for 2 minutes Chang estimated carbon concentrations on Si(111) specimens to be typically less than '2 x 10^{14} atoms/cm^2,' or 1/40 to 1/4 of a monolayer, depending on whether carbon atoms were distributed uniformly throughout the detected volume or were all at the surface. Further heating reduced the remaining carbon concentration much more slowly to a minimum level of 1 x 10^{13} atoms/cm^2.

In the present study, heating the Si(100) surface to ~1250 °C for less than one minute produced a carbon level characterised by an Auger peak-height ratio C/Si $\lesssim$ 3 x 10^{-3}. In Debe's study [81] repeated heating to a similar temperature produced a peak-height ratio of C/Si $\lesssim$ 5 x 10^{-3}. If we may assume that these figures refer to a concentration essentially similar to that observed by Chang then the carbon level of C/Si $\lesssim$ 2 x 10^{-3} achieved in our ion bombardment process would seem to correspond to a carbon concentration of no greater than 1/60 to 1/6 of a monolayer, again depending upon its distribution in the detected volume.

We note that the impurity concentration required to stabilise a (2 x 1) surface net is 1/2 monolayer. The average impurity level detected for such a structure may of course be less than this value if the entire surface is not ordered in this way.

Evidently this discussion is not at all rigorous, though it would seem to suggest that the carbon concentration is likely to be substantially less than the amount implied by a carbon stabilised (2 x 1) surface net.

Attempts to detect the high-energy peaks (~1 kV) of metal contaminants reported by Chang [61] were unsuccessful, owing to inadequate sensitivity in this region. Silicon peaks in this energy range were barely detectable. The low-energy peaks of suspected metal contaminants such as Cu, Fe, and Ni coincide with the silicon series; thus impurity levels are extremely difficult to assess. However, as reported previously, concentration of these metals after heating to > 1000 °C was estimated by Chang to be less than 1/10 monolayer in total; we might expect lower concentrations in the present work, because of the generally lower annealing temperatures used. We conclude that the Si(100) (2 x 1) structure is almost certainly characteristic of the clean surface.

CHAPTER FOUR

ANGULAR DEPENDENCE OF AUGER ELECTRON EMISSION

I. Introduction

The study of the angular dependence of Auger electron emission is a relatively new and unproven technique. The method was first proposed as a technique for the determination of the position of impurity layers within the surface region of a solid. The first experimental study of clean single crystal surfaces was performed by McDonnell and Woodruff [51,82,83]. This work on Cu(100) and (111) surfaces was followed by similar results from Fe(100) [84], and recently by some further work on copper [85], and on nickel and aluminium [86].

In the following chapter we will discuss the theory of the angular dependence of Auger electron emission and present some results for the Si(100)(2 x 1) clean surface structure and the Si(100)(1 x 1)H structure produced by hydrogen adsorption. This data should enable us to assess the value of the approach in the determination of the surface structure of silicon and other semiconductors.

II. Theory

In treating the theory of the angular dependence of Auger electron emission we may decompose the problem into two parts.

1. The Initial State; an Auger electron is emitted from an atom within the surface region of the crystal, with a wave function, ψ_o.

2. The Final State; in which the electron is scattered (possibly multiply scattered) by other atoms in the crystal and emerges from the surface with a wave function, ψ_e.

Structure within a profile of intensity versus angle, an Auger Electron Angular Profile (AEAP), therefore arises from non-isotropic emission from the excited atom or from the diffraction process, or both.

Early work emphasised the former approach for explanation of the experimental results [51]. However, Matsudaira *et al.* [84] used a very simple diffraction model to calculate AEAP's, and claimed that the model explained the major features of their experimental results from Fe(100).

The angular dependence of photo-emitted electrons clearly has many similarities to the case of Auger emission and has stimulated a number of theoretical discussions. Work by Gadzuk [87], has emphasised the importance of the initial state in the emission process, whereas the discussion by Liebsch [88], considered the final state--diffraction--to be the dominant effect.

For the specific case of the $M_{2,3} M_{4,5} M_{4,5}$ emission from the clean Cu(100) and (111) faces McDonnell *et al.* [83] compared experimental profiles for several azimuthal angles with profiles calculated using a single scattering model for the final state effect.

The kinematic calculation was based on a muffin tin model of the crystal structure. Ion core potentials were expressed in terms of phase shifts calculated for the LEED energy range. The complex inner potential was chosen on the basis of LEED results from the same surface. In this single scattering model the imaginary part of the potential was chosen from studies of averaged LEED data and simulates damping produced by both inelastic and elastic processes, as in the

pseudo-kinematic calculations used in the CMTA method. The initial state was described by a spherical outgoing wave centred on the emitting atom, i.e., the initial emission was assumed to be isotropic.

Angular profiles calculated in this approximation showed some agreement with experiment. The temperature dependence of the profiles was also calculated since diffraction processes are expected to show a strong dependence on temperature through the Debye-Waller factor. Initial states would not be expected to show such a strong temperature dependence. The temperature dependence of structure within calculated profiles showed a similar magnitude to that observed experimentally.

The results of this analysis illustrated clearly that diffraction effects are important in the formation of angular emission profiles. The kinematic calculations used in this work are not expected to be adequate however, since they have proved to be insufficient to explain LEED results in the same energy range.

In view of this fact Pendry [89] and Holland [90] have recently developed multiple scattering treatments for electron emission from solid surfaces. These treatments are very similar to those employed in LEED intensity calculations. In fact Pendry has simply modified his Renormalized Forward Scattering perturbation calculation originally developed for LEED work. Holland's approach is based on the similar Reverse Scattering method.

While the importance of diffraction effects has been established, the effect of the initial state on angular profiles has still to be assessed. Clearly it may be significant, particularly in covalent

materials where emission from valence states might be expected to be markedly non-spherical. In these cases separation of initial state and final state effects may be complicated.

Estimates of the magnitude of the initial state effect are further complicated by a fact discussed previously. Auger electron emission leaves the atom in an excited state. Anisotropy of emission from this state may therefore be difficult to estimate.

IIi. Adsorbates

Perhaps the most useful application of the Angular Dependence of Auger Electron Emission or angle-resolved photoemission is in the determination of adsorbate atom sites.

Using a single scattering calculation which assumed spherical emission from the adsorbate atom, Woodruff [91] considered the case of sulphur on Ni(100), a structure which had created initial disagreement in LEED interpretations as discussed in Chapter One.

Woodruff showed that the strong elastic backscattering by the substrate, of the Auger electrons emitted from an adsorbed sulphur atom, produced emission profiles which were very sensitive to the adsorption site of the emitting atom. Thus the study of the angular dependence of Auger and photoemitted electrons may prove to be a valuable technique, especially for weakly scattering adsorbates for which LEED is relatively insensitive to the adsorption site.

III. Experimental Procedure

Though this work is described first, in fact it was performed after much of the LEED data had been taken. Criteria for surface perfection

had therefore been established both for the clean (2 x 1) superstructure as described in Chapter Five, and for the (1 x 1)H structure, in Chapter Six.

Previous work by McDonnell [51,82,83] using the same experimental system was hampered by the fact that the electron guns used lay in the plane of rotation of the Faraday cup, thus certain regions of the angular profiles obtained were missing or 'fitted' by using both guns with a correction for the change in angle of incidence. For most of the present work the exciting beam was provided by another electron gun mounted out of the plane of rotation; profiles were thus obtained over a full range of 180° and no 'fitting' or correction was necessary. The gun was the same type as used for normal Auger analysis, a "Superior Electronics" type SE 3K 5U, fitted with beam-deflection plates. An indirectly-heated oxide cathode provided beam currents of up to ~50 μA at an energy of 1.5 keV.

Connection to the three energy analysing grids in the Faraday cup was made in the usual way, illustrated in Fig. 3.3, G_2/G_3 being connected to the energy analysing potential and applied modulation; G_4 was maintained at earth potential. Auger electron currents were amplified by means of the Lock-In phase sensitive detection system and the displacement current neutralised by a similar network to that used for the full LEED-Auger optics. A potential of ~90 V was applied to the wooly soot coated-collector to limit secondary electron emission. Some care was taken in positioning the specimen and incident beam, to ensure that the excited region lay on the axis of rotation of the Faraday cup.

It is estimated that the error arising from a misalignment is $\leq 3°$ at an emission angle of 45°. Errors in the position of the Faraday cup also affect the energy resolution of the cup, as noted in Chapter Two; this effect is considered to be negligible in this instance. The energy resolution of the cup has been measured [51] at 1%. The acceptance angle of the cup (7°) is rather large for such studies and this fact together with the limited sensitivity of the retarding field analyser makes this system somewhat unsatisfactory for this work. It was felt worthwhile, however, to perform certain experiments of a limited nature in order to evaluate the importance of the angular emission effect in silicon and its dependence on the surface superstructure.

Measurement of angular emission profiles was accomplished by simply plotting the large 92 eV silicon peak for a range of emission angles. The energy range covered was from ~70 eV to ~110 eV to include the entire Auger peak, at cup angles at 2-1/2° intervals in the range -70° to +70°, and at larger intervals at greater emission angles, typical sweep rates were ~1 V/S with a time constant of ~300 mS. The peak-to-peak height of the 92 eV Auger feature was then plotted as a function of emission angle to produce an angular profile.

IV. Results

IV1. The Si(100)(2 x 1) Structure

In studies of angular Auger electron emission from the clean Si(100)(2 x 1) surface certain precautions were taken to ensure there was no disordering of the surface produced by the incident beam. Some

disordering had been observed in the (2 x 1) superstructure during LEED experiments, at much lower beam currents than used for angular Auger work. Relatively high beam currents, of at least 2 μA were necessary because of the poor sensitivity of the system.

Following measurements of angular profiles the surface was examined by LEED for evidence of disorder. However, in using different electron guns for the Auger and LEED work as well as the movement of the specimen necessary between the two sets of measurements, there could be no assurance that these observations referred to the same region of the specimen surface. Therefore certain angular profiles were plotted using the LEED gun to provide the exciting electron beam; LEED observations made before and after these measurements detected no significant surface disorder, and in this case we have more assurance that the observations refer to a common region of the surface, if we assume negligible movement of the electron beam as the energy is changed. The angular profiles produced using the low incident current of the LEED gun (≤1 μA), had a poor signal-to-noise ratio but in general showed similar structure to those plotted at higher beam currents. We conclude that the structure in these profiles is characteristic of a well-ordered surface.

We may remark at this point that surface order might be expected to be rather less important for angular Auger work than for LEED, in the specific case of measurement of 'intrinsic' Auger peaks due to a clean surface, because in angular Auger the contribution from 'bulk' atom layers is a higher proportion of the total signal. Of course this also limits the effectiveness of the technique in the determination of clean surface structures.

In addition, whereas LEED requires relatively long range order over areas comparable with the coherence zone of the beam, angular Auger is primarily sensitive to local order. The two techniques will therefore show different results as a result of their sensitivity to different types of surface damage.

Further work was performed using the SE 3K 5U, with a beam energy of 1 kV and specimen current of ~5 μA. The beam was defocussed slightly to produce a spot of diameter ~1 mm, in order to reduce the incident power per unit area dissipated in the specimen. In view of the large angular width of the Faraday cup the effect of the beam broadening on angular resolution is negligible; though the relative magnitude of peaks at different angles of incidence may be modified as discussed by McDonnell *et al.* [83].

Results of these studies are plotted in Fig. 4.1 as the average of 3 profiles for each of the <110> and <100> azimuths, in order to improve signal-to-noise ratio.

These profiles show considerably less structure than those observed for copper surfaces, and the profiles from the two azimuths differ only slightly. Both profiles reflect the mirror symmetry inherent in the crystal in these azimuths, in that they are symmetric about the surface normal, within the limit of experimental accuracy.

IVii. The Si(100)(1 x 1)H Structure

Following the hydrogen adsorption work to be described in Chapter Six angular Auger profiles were plotted for the silicon 92 eV peak for the (1 x 1)H structure; adsorption procedures were as described in

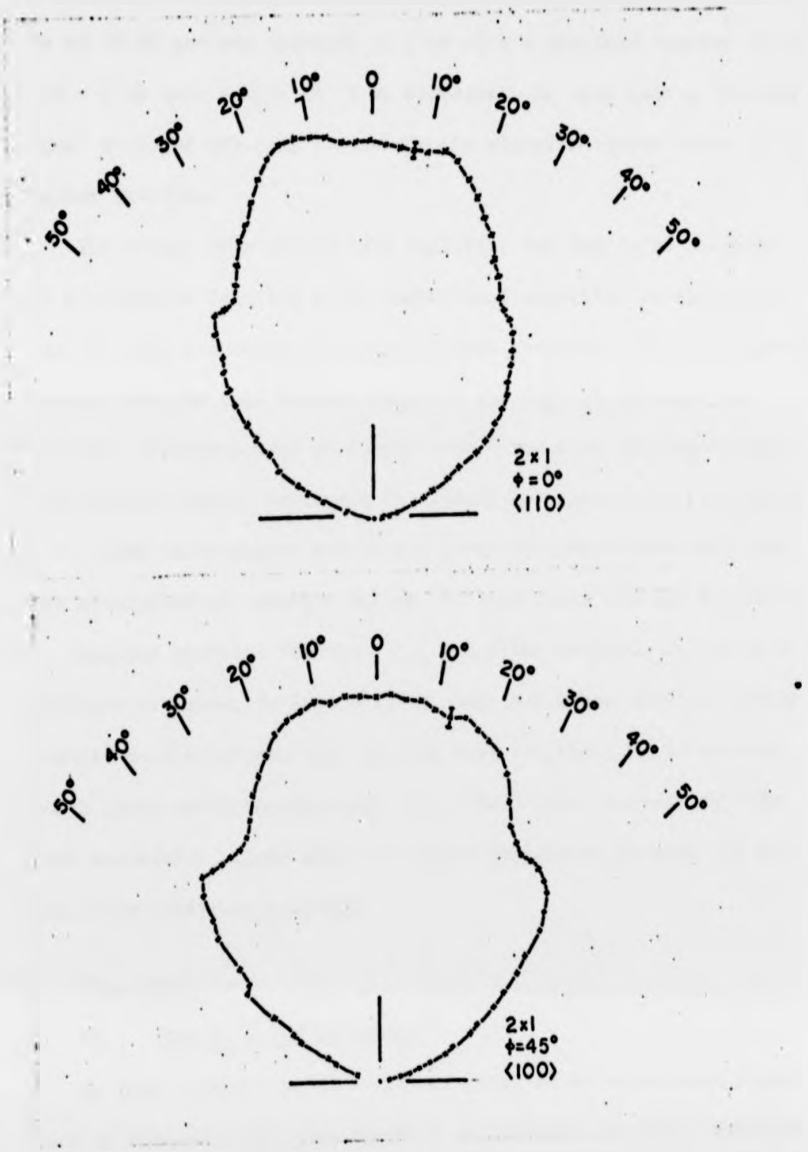

Fig. 4.1 $L_{2,3}V_1V_1$ Auger emission profiles for the Si(100)(2 x 1) surface in the <110> and <100> azimuths.

that chapter. In order to avoid desorption of hydrogen under the beam, the SE 3K 5U gun was operated at 1 kV with a specimen current of only 1 μA - 2 μA into a spot of ~1 mm diameter. In this case a 'Datalab' signal averager was used to improve the signal-to-noise ratio of the angular profiles.

The output from the Lock-In amplifier was fed to a 'Keithley' 417 picoammeter (serving as an operational amplifier in this case), which in turn was connected to the signal averager. This arrangement ensured that the full dynamic range of the digital averager was utilized. Averages were performed over 4 scans of the Auger peak for each emission angle, improving the signal-to-noise ratio by a factor of 2. LEED observations before and after the Auger work indicated that desorption of hydrogen during the experiment was not significant.

Angular profiles for the <110> and <100> azimuths in the (1 x 1)H structure are shown in Fig. 4.2. We see that these profiles contain slightly more structure than was the case for the (2 x 1) surface, though again still considerably less detail than is observed from other materials. Again there is little difference between the profiles from different azimuths.

V. Discussion

Vi. The (1 x 1)H Structure

We might expect the (1 x 1)H structure to be relatively simple since it possesses the same symmetry as the bulk crystal. Hydrogen adsorption may be expected to saturate the dangling bonds, allowing the surface to relax to essentially the bulk structure, though with a

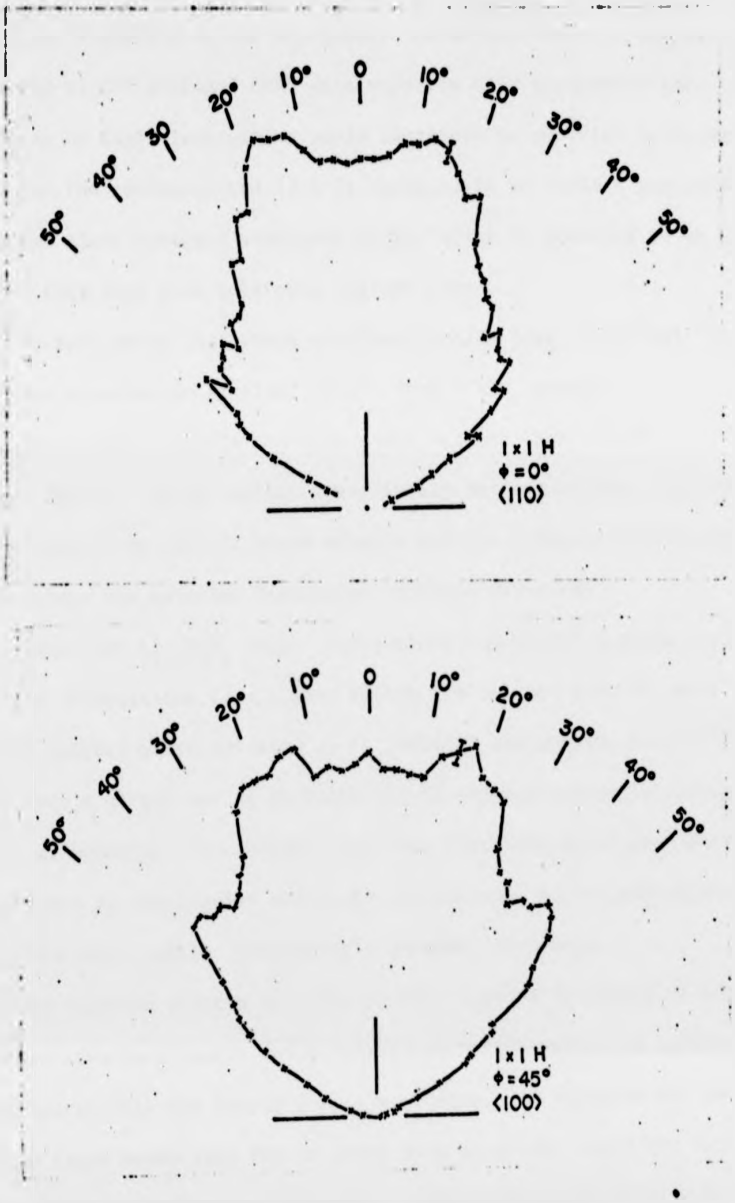

Fig. 4.2 $L_{2,3}V_1V_1$ Auger emission profiles for the Si(100)(1 x 1)H surface in the <110> and <100> azimuths.

different d-spacing in the top layer. As we will show in Chapter Seven, analysis of CMT averaged LEED data supports this interpretation. Angular profiles of Auger intensities would therefore be expected to be simpler than for the reconstructed (2 x 1) surface, if we neglect scattering from the light hydrogen adsorbate atoms, which is expected to be much weaker than that from substrate silicon atoms.

We have noted that these profiles contain less 'structure' than has been observed in similar results from f.c.c. metals.

The angular profile contains contributions from roughly 5 to 15 atomic layers. If we neglect specifically surface effects, and divide the process into initial state effects and final state effects, we may discuss the relative importance of these processes.

Since the $L_{2,3}V_iV_1$ Auger transitions considered in these studies involve transitions from states within the valence band we might expect initial state emission to be markedly non-spherical in silicon, as a result of the strong perturbation of valence states by strong covalent bonding. The initial state may therefore be of considerable importance in the angular structure, in contrast to the situation in the relatively weakly bound metals studied previously.

Diffraction effects may also be more complex by virtue of the silicon structure factor which introduces modifications of intensities as compared with the simple f.c.c. structure. In addition the basis of two atoms means that for an ideal bulk structure there are two non-equivalent sites for emitting atoms. For the (1 x 1)H structure the presence of the surface introduces at least one further non-equivalent site.

Each emitting atom in the bulk 'sees' scatterers related by only 2-fold rotational symmetry, rather than the 4-fold symmetry characteristic of the simple f.c.c. structure.

An angular profile consists of a superposition of diffracted intensities emitted from these non-equivalent sites. Summing the incoherently emitted electron waves from the two (or more) sets of sites will tend to "wash-out" both initial and final state effects. This would produce a profile with less sharp structure than for f.c.c. metals, as observed.

Multiple scattering effects are also present though their effect on the profiles is difficult to assess.

Vii. The (2 x 1) Structure

Our interest in the technique is of course primarily concerned with the surface layer. We note that the angular profile shows some sensitivity to surface structure as evidenced by comparison of the profiles obtained from the two structures. In this context we may refer to the increased complexity of structure within LEED profiles from the (2 x 1) structure as compared with the (1 x 1)H form, as we will show later. Much of this additional structure may be interpreted as multiple scattering effects. These may not be as important for angular emission studies, since the profiles consist of an average over a range of diffraction angles [83].

We observe however that (2 x 1) angular profiles contain effectively less well-defined structure than the (1 x 1)H profiles, while the form is essentially similar. The reconstructed surface leads to further 'washing-out' of structure in the angular emission profiles.

Again we may attribute this to an increased complexity of structure. As we have remarked, an ideal bulk silicon structure has two non-equivalent emitting atom sites, a (1 x 1)H terminated structure at least three. For the bulk crystal terminated by a (2 x 1) reconstructed surface the number of non-equivalent emitters is at least four. Thus an incoherent sum will result in a 'washed-out' profile, obscuring features produced by initial and final state effects.

As an illustration of this effect Fig. 4.3 shows profiles calculated for an ideal (1 x 1) structure and a possible (2 x 1) structure. The calculation was performed by Woodruff [9], in the single scattering approximation for the final state, neglecting initial state effects. The model for the (2 x 1) structure was an ideal radius, 'hard-sphere' model of the 'leaning-rows' structure. While these profiles do not reproduce the structure found experimentally--due to the omission of a reasonable account of the initial state and multiple scattering--the effect on the profile on moving from the (1 x 1) structure to the (2 x 1) reconstruction is significant. We note that the (2 x 1) structure exhibits somewhat less well defined features as observed in experimental profiles, though again the general form is similar.

Viii. Implications for Future Work

This result places some doubt on the sensitivity of the angular Auger technique in surface structure determination since the fairly profound change in superstructure, from (1 x 1)H to (2 x 1), fails to produce substantial changes in the profile, largely because of the absence of any clearly defined features in any of the data.

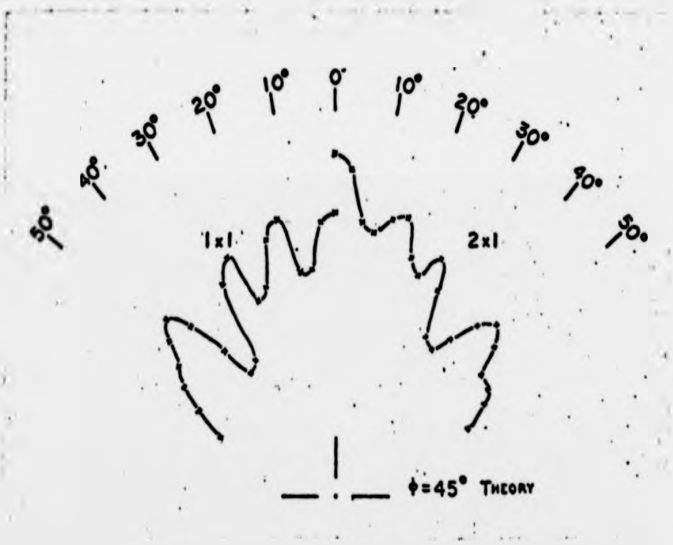

Fig. 4.3 Theoretical $L_{2,3}V_1V_1$ Auger emission profiles for ideal (2 x 1) and (1 x 1) surfaces calculated by Woodruff [92].

This may well be true for other materials with a complex bulk structure. Angular dependence of Auger emission may therefore prove to be ineffective in 'intrinsic' clean surface structure determination, at least for these materials.

We note that this conclusion does not weaken the case for use of the technique in adsorbate structure determination, since many of the effects associated with the bulk, and specifically the proportion of collected intensity which arises from the surface layer, are not encountered in that case. In adsorbate structure determination all emission arises from the adsorbed layer. Diffraction of this emission by the substrate should then permit the structure to be inferred.

CHAPTER FIVE

SI(100)(2 x 1) CLEAN SURFACE LEED DATA

I. Experimental Procedures

The experimental system has been described in detail in Chapter Two, together with the methods adopted for initial alignment of the specimen position. Here we will discuss the setting of experimental parameters and the conditions under which LEED data was taken for the clean (2 x 1) structure.

In plotting I-V spectra using the AC detection method the voltage of G_1, the Wehnelt cylinder of the electron gun, was set to produce an electron beam small in diameter and with a small energy spread, consistent with obtaining a satisfactory signal level with a modulating voltage of several volts. The beam diameter was ~1 mm at the specimen. The beam current used was typically ~0.25 μA at 75 eV.

The ramp rate of the electron energy, the limiting factor in the speed of data collection, was set to 3-4 volts/sec. This was determined to be the maximum rate possible without unacceptable shifts of the peaks in I-V spectra, due to the characteristic time constant of the electron energy power supply. The time constant of the Lock-In amplifier was ~10 mS - 30 mS.

Azimuthal angle adjustments for both specular and non-specular beams were made by viewing the LEED pattern and aligning the chosen azimuth with the plane of rotation of the Faraday cup; settings were checked by measurement of photographs of the LEED pattern. Accuracy of these settings is estimated to be within $\pm$ 1°.

Having determined the normal incidence position, in the manner described previously, the angle of incidence was set to the required value. Inaccuracies introduced by any free-play in the manipulator were eliminated by rotating the specimen in one sense only. Angle of incidence settings are estimated to have an accuracy of ± 1/2°

II. (00) Beam Data Collection

Faraday cup settings for (00) beam data collection were made by adjusting the cup position for maximum detected intensity, with the electron energy set to a suitable peak in the (00) beam spectrum. The (00) beam spectrum was then plotted by ramping the electron energy over the required range. Most spectra were taken in two sections, covering the energy ranges 20 eV - 380 eV and 200 eV - 580 eV; the higher energy range plotted at higher modulation and sensitivity. Spectra were plotted for five azimuths in the (2 x 1) structure, ϕ = 0°(<110>), 22.5°, 26.5°, 35°, 45°(<100>), at angles of incidence from 8° - 32° in steps of 2°.

III. Non-Specular Beam Data Collection

In order to establish the required positions of the Faraday cup for collection of non-specular beam intensities, calculations were made of the emergence condition for the various beams together with observations of the range of movement of the beams when visible in the LEED screen. These procedures were necessary in order to eliminate spurious results produced by incorrect positioning of the cup. This was particularly important when the beam in question was not visible in the screen to avoid collection of intensity from the 'wrong' beam.

Plotting of an I-V spectrum for a non-specular beam was accomplished by moving the Faraday cup in 2° steps (at fixed specimen angle of incidence). For each cup position the electron energy was ramped over a small range to move the beam in question across the cup aperture. The intensity profile for this beam was the enevelope of the curves produced in this way. Data was collected for the (1/2,0), (1,0), (1,1/2), and (1,1) beams in the (2 x 1) structure, over a range of angles of incidence from 0° - 30° in 2° steps. I-V spectra were also produced for the (2,0), (2,1), (3/2,0), and (3/2,1) beams at normal incidence only.

IV. Surface Conditions During Experiment

The procedures adopted for obtaining a clean well-ordered surface were described in detail in Chapter Three.

Concentrations of impurities during experimental runs were monitored by means of Auger spectra taken before and after LEED data. The only contaminant detected in these spectra was carbon, typically characterized by a peak-height ratio of $1 - 2 \times 10^{-3}$ and the concentration was never greater than 4×10^{-3} (this concentration was only occasionally reached, at the end of a long experimental run). Other impurities were never visible, if present their concentrations were such that their peak height was $< 1 \times 10^{-3}$, the noise level in Auger scans. The concentration of metal contaminants has been discussed in Chapter Three, the concentration is likely to be much less than 1/10 monolayer in total, distributed throughout the detected volume.

Some disordering of the surface during experiments was detected from LEED I-V spectra; the criterion for a well-ordered surface was that changes in relative intensities of peaks in LEED spectra should be less than 10%.

V. Measurement of Beam Current

In order to correct for the variation of beam current with energy the beam current was measured into the Faraday cup, with a 'Keithley' 417 picoammeter. The magnetic field compensation current supplies were adjusted to maximise the current into the cup for values of beam energy from 10 eV - 580 eV. This small deflection of the beam was necessary to correct for the small misalignment of gun and cup axes. As for LEED measurements, 90 V was applied to the collector to limit secondary emission.

The method of measurement also takes into account any variation of collector efficiency as a function of energy. The beam current function is illustrated in Fig. 5.1.

VI. (2 x 1) LEED Data

In order to produce normalised data plots with a uniform intensity scale the experimentally plotted data was digitised and processed by computer. Digitisation of the curves was carried out by hand using a 'PCD' digitiser linked to a data logger, numerically coding the intensity and energy coordinates of points in each curve for (e.g.) approximately 300 points for a (00) beam spectrum. The energy resolution of these measurements varied according to the information content

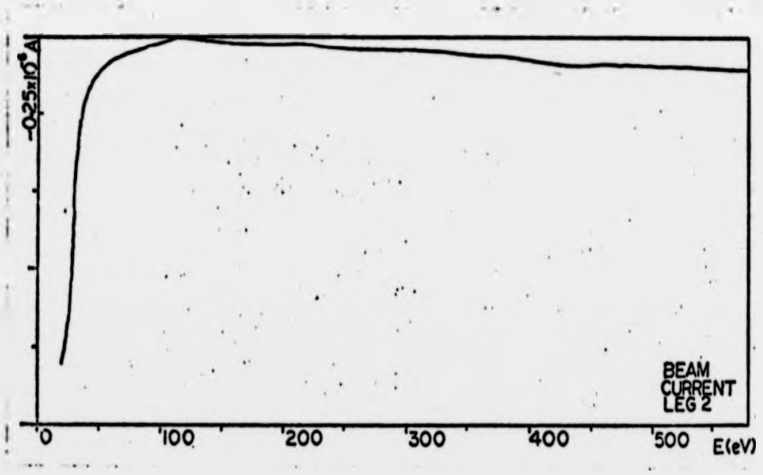

Fig. 5.1 The beam current from the LEG2 LEED gun as a function of energy

within the curve, with a fine resolution of ~0.5 eV for rapidly varying portions of the spectrum. The precision of peak positions is to within ± 0.5 eV. Measurement of peak heights also vary in accuracy from < 0.5% for the largest peaks to ~5% for the smallest peaks in the spectra. These uncertainties are no greater than those present in the original plots.

Punched paper tapes produced by this method were fed to a 'G.E.C.' 4080 computer and edited. The data were then normalised to the incident beam current using the digitised beam current profile illustrated in Fig. 5.1. The normalised profiles shown in Figs. 5.2 to 5.13 were produced using the digital plotter of an 'Elliott' 4130 computer.

VIi. Accuracy

We have discussed possible errors introduced by the digitising process. Errors in the data as a whole, arising both from this process and from experimental sources as discussed in Chapter Three, are probably beyond the ability of current dynamical theory to resolve, with the exception of errors in angle of incidence. LEED spectra are very sensitive to changes in this parameter; errors here may account for some of the poor agreement found previously between experimental and calculated profiles, especially when these comparisons were based on limited ranges of data. The data presented here include profiles for a large range of angles of incidence at 2° intervals, observation of changes in peak shapes as a function of angle of incidence provide for a better comparison with calculated curves.

In the case of averaging, this process tends to average out these small errors, though some slight broadening of peaks may result in consequence of the limited energy resolution. This broadening is expected to be less than 1 eV.

VIii. Intensity-Energy Spectra

LEED Intensity-Energy spectra for the (2 x 1) surface are illustrated in Figs. 5.2 to 5.13, Bragg peak positions at normal incidence for the bulk structure are indicated where appropriate. No correction for the crystal inner potential has been made in these curves, kinematic features are therefore shifted downwards in energy by ~10 eV. Intensities are labelled as a fraction of the incident beam. In the following discussion we will first emphasise features of individual beams, going on to discuss the data as a whole.

VIii(a) (00) Beam. The angular evolutions of (00) beam spectra are presented in Figs. 5.2 to 5.8 for five azimuthal angles. The normal incidence Bragg peak positions for the bulk structure are indicated. The first Bragg peak occurs at an energy of ~20 eV (i.e., ~10 eV after correction for the inner potential) and is below the lower energy limit for these measurements.

The intensity in this beam is ~4 x 10^{-3}, expressed as a fraction of the incident beam. This is the mean value of the large peak at ~72 eV, averaged over the five azimuths, and is characteristic of the relatively low intensities observed in LEED, due to the large cross-section for inelastic scattering in this energy range.

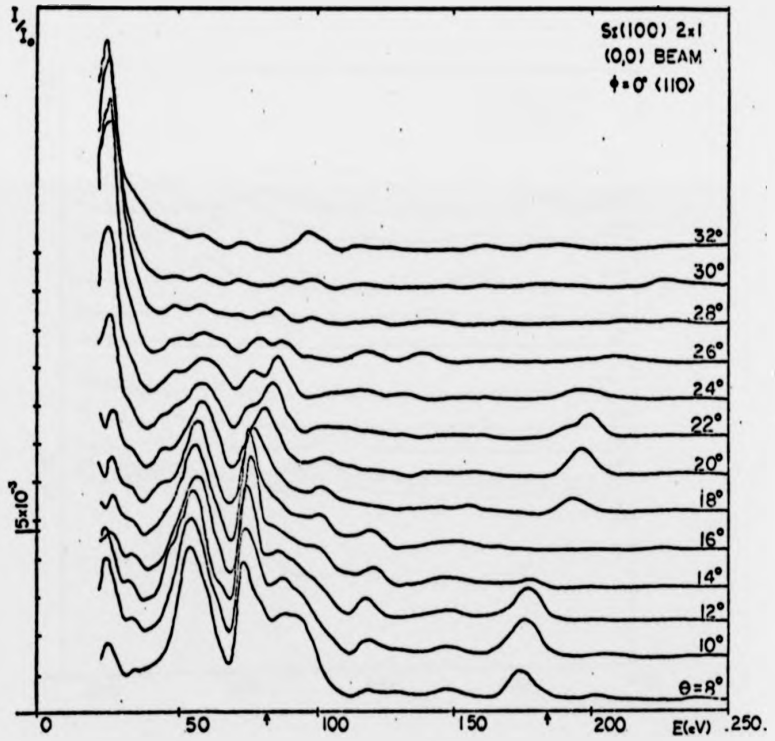

Fig. 5.2 Intensity-Energy spectra for the Si(100)(2 x 1) surface. (00) beam, $\phi = 0°$. † indicates bulk Bragg peak positions at normal incidence.

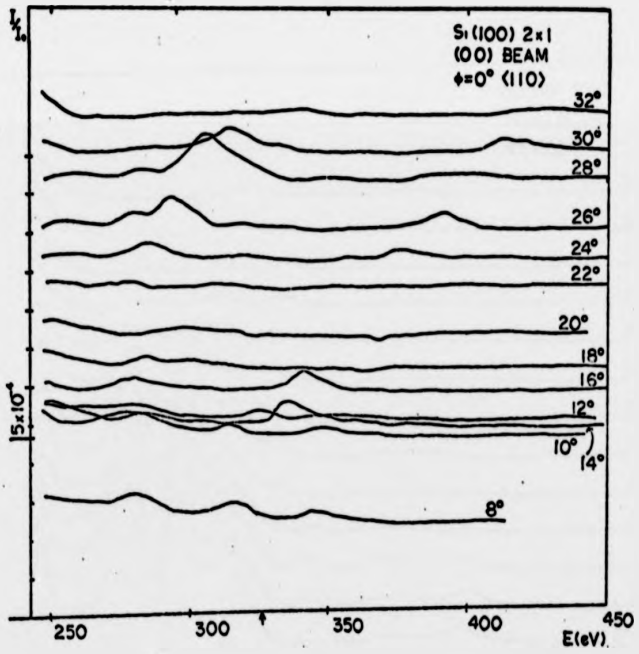

Fig. 5.3 Intensity-Energy spectra for the Si(100) (2 x 1) surface. (00) beam, ϕ = 0°. ↑ indicates bulk Bragg peak positions at normal incidence.

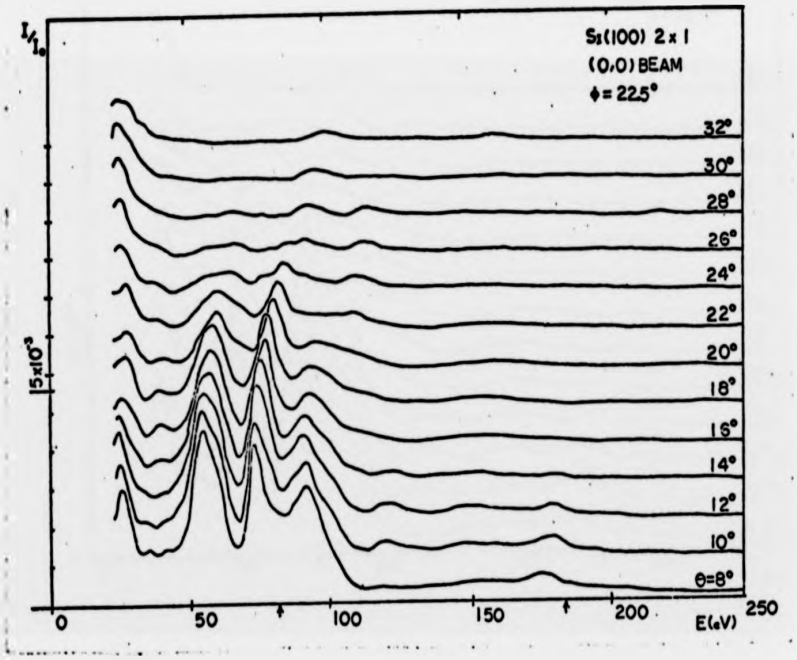

Fig. 5.4 Intensity-Energy spectra for the Si(100)(2 x 1) surface. (00) beam, $\phi = 22.5°$. ↑ indicates bulk Bragg peak positions at normal incidence.

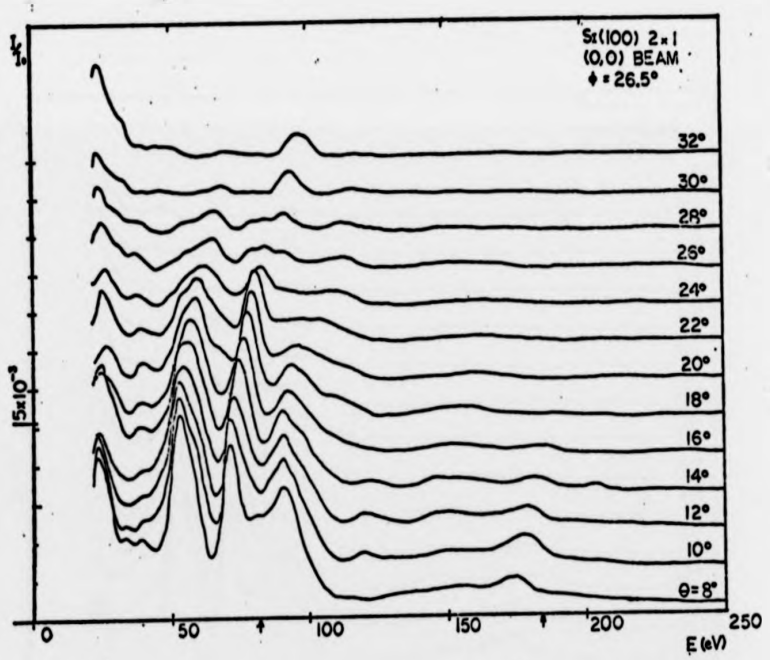

Fig. 5.5 Intensity-Energy spectra for the Si(100)(2 x 1) surface. (00) beam, ϕ = 26.5°. ↑ indicates bulk Bragg peak positions at normal incidence.

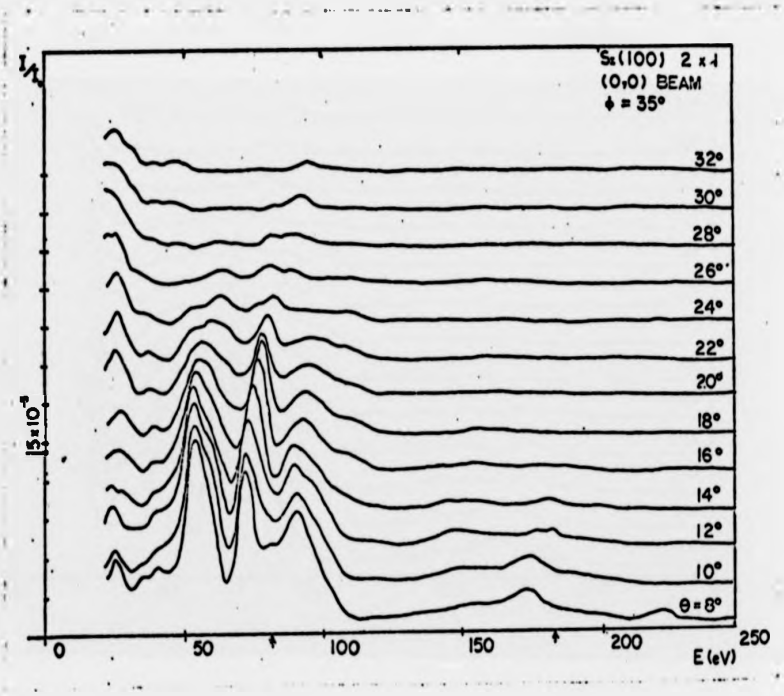

Fig. 5.6 Intensity-Energy spectra for the Si(100)(2 x 1) surface. (00) beam, $\phi = 35°$. ↑ indicates bulk Bragg peak positions at normal incidence.

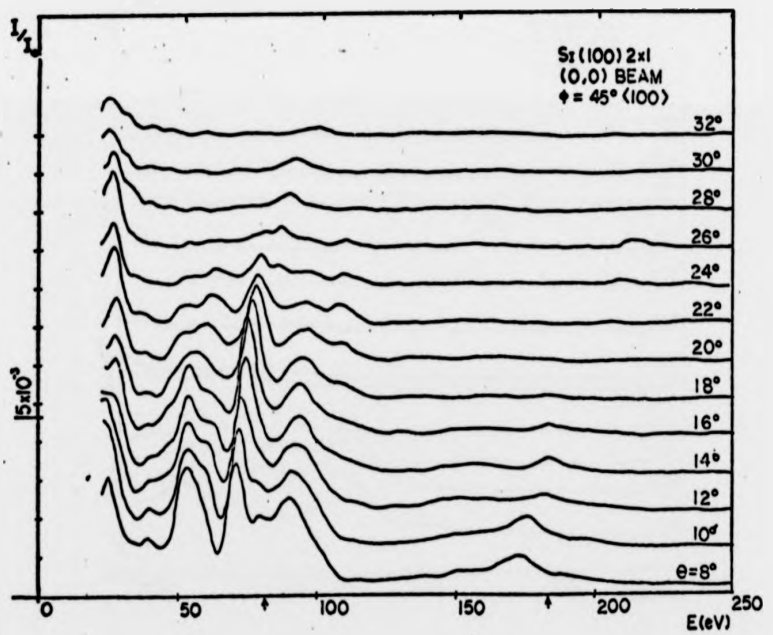

Fig. 5.7 Intensity-Energy spectra for the Si(100)(2 x 1) surface. (00) beam, $\phi = 45°$. † indicates bulk Bragg peak positions at normal incidence.

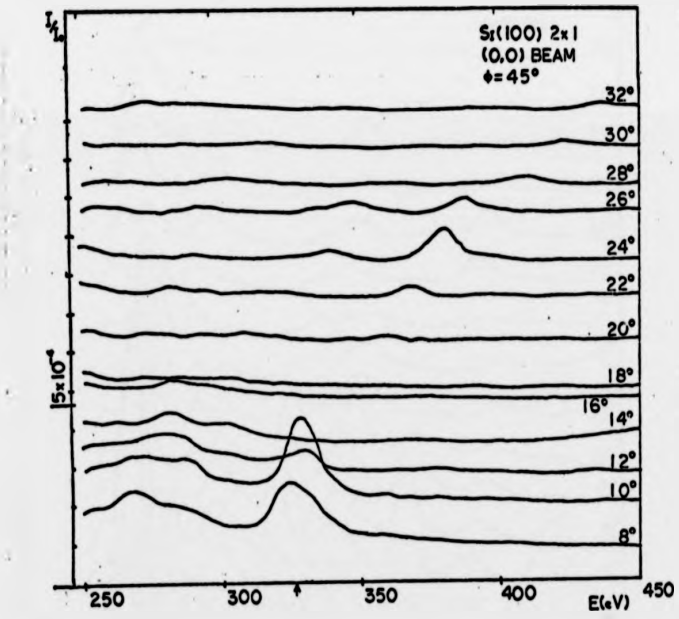

Fig. 5.8 Intensity-Energy spectra for the Si(100) (2 x 1) surface. (00) beam, ϕ = 45°. ↑ indicates Bragg peak positions at normal incidence.

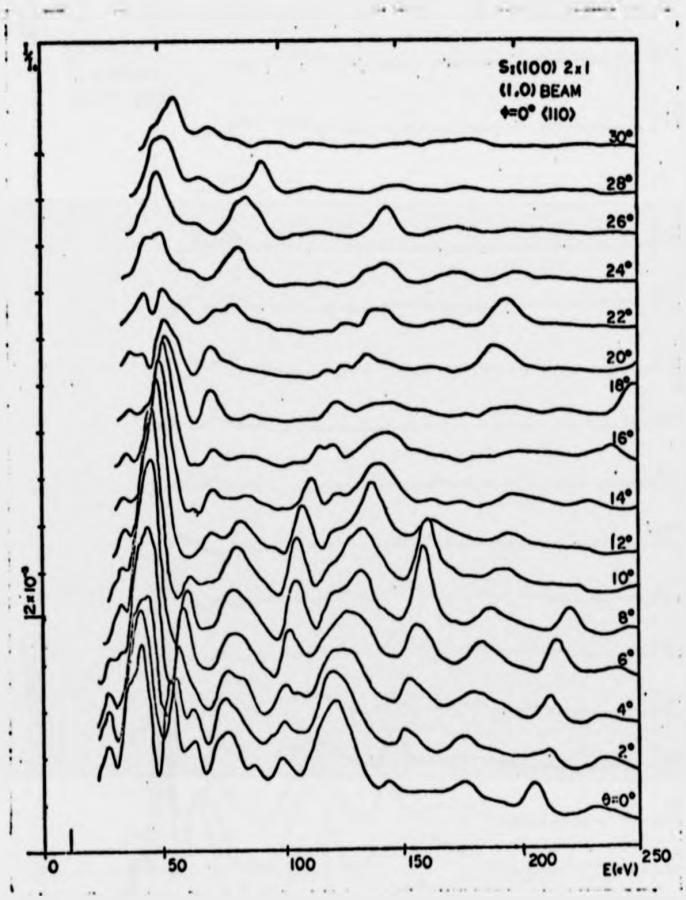

Fig. 5.9 Intensity-Energy spectra for the Si(100)(2 x 1) surface. (1,0) beam, $\phi = 0°$.

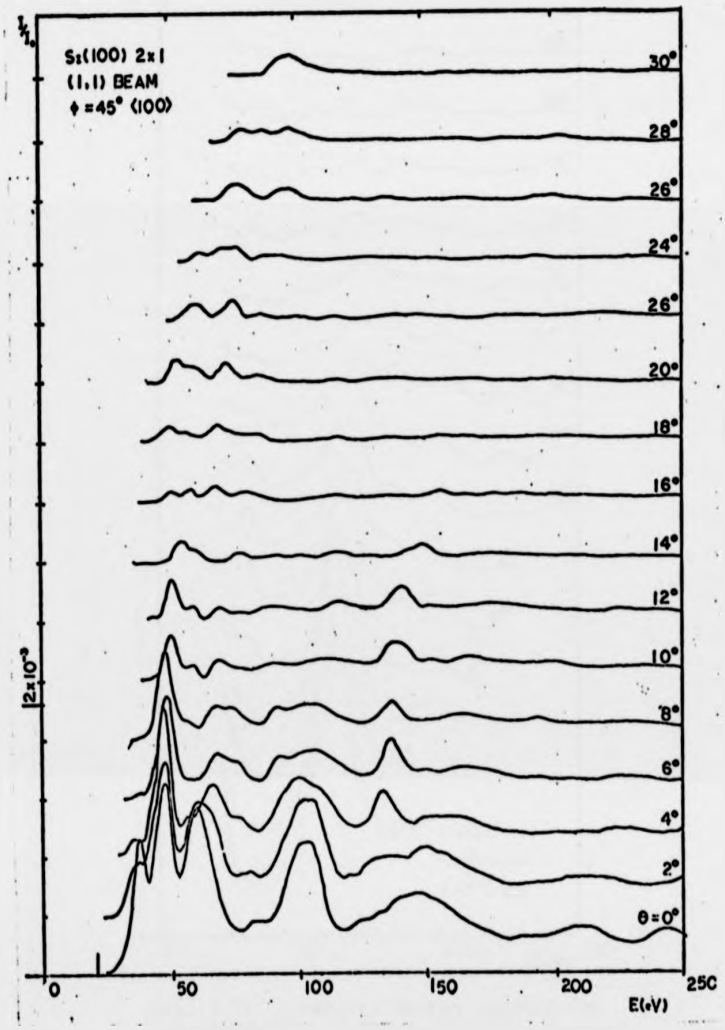

Fig. 5.10 Intensity-Energy spectra for the Si(100)(2 x 1) surface. (1,1) beam, $\phi = 45°$.

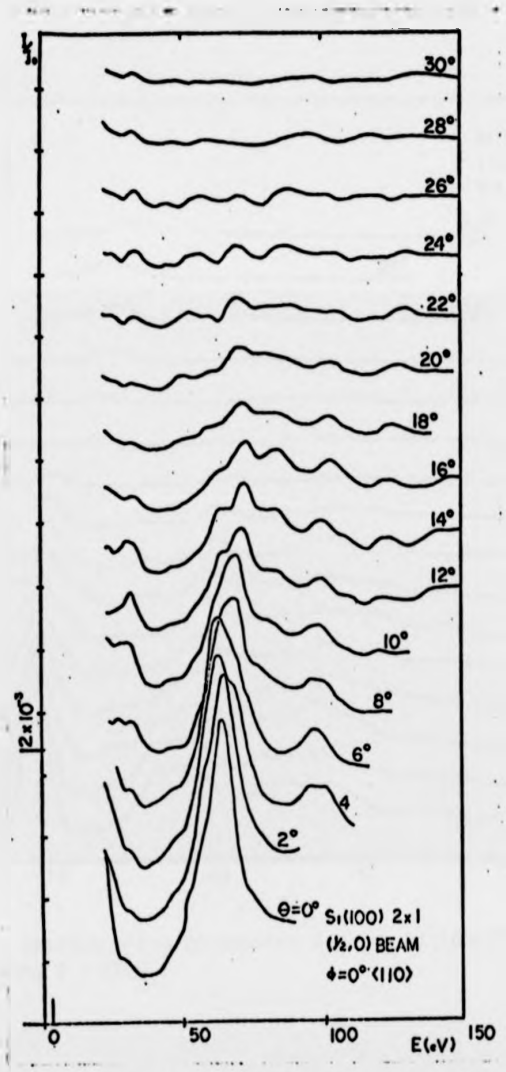

Fig. 5.11 Intensity-Energy spectra for the Si(100)(2 x 1) surface. (1/2,0) beam, $\phi = 0°$.

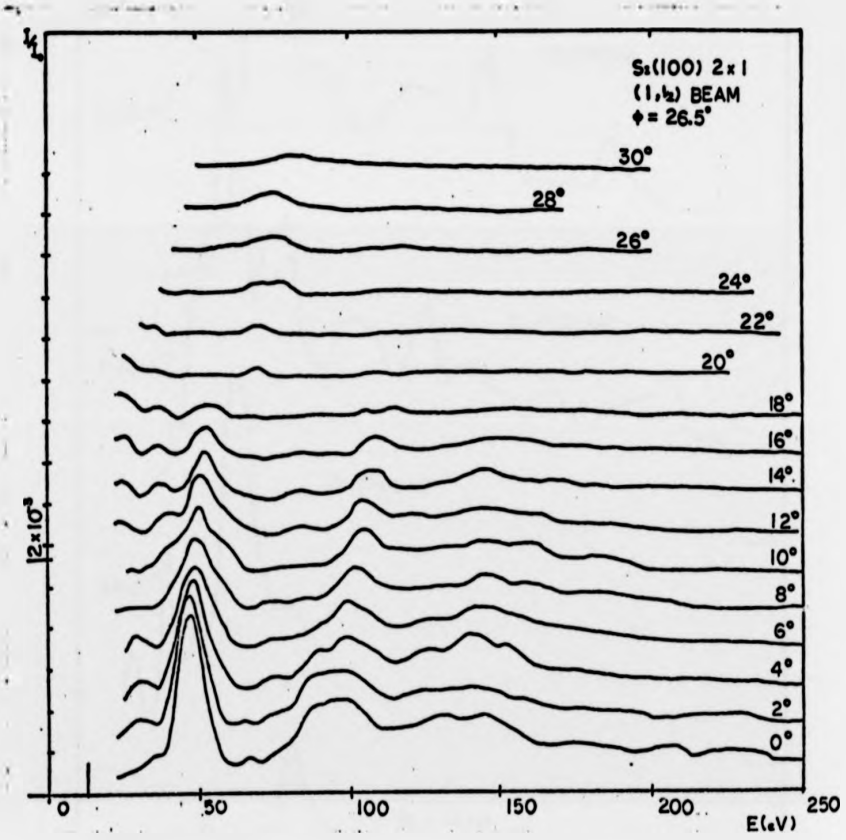

Fig. 5.12 Intensity-Energy spectra for the Si(100)(2 x 1) surface. (1,1/2) beam, ϕ = 26.5°.

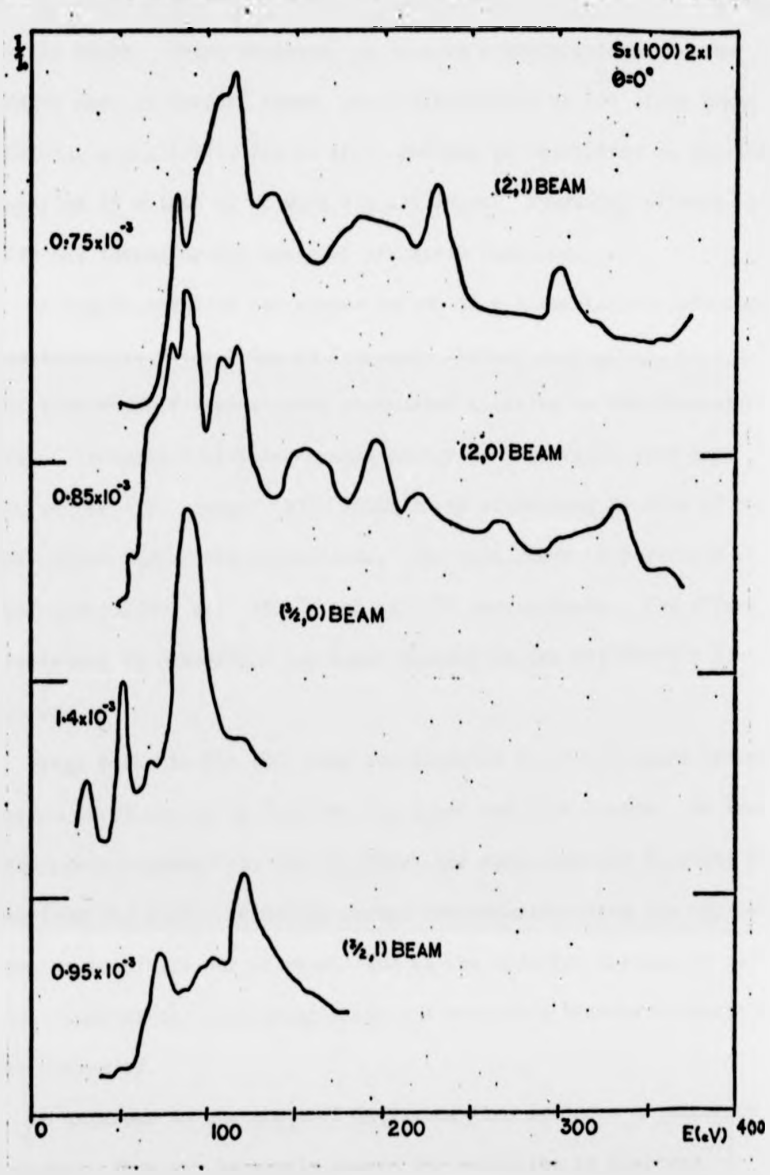

Fig. 5.13 Intensity-Energy spectra for the Si(100)(2 x 1) surface. (3/2,1), (3/2,0), (2,0) and (2,1) beams. The intensity figures on the left refer to the maximum height of the respective curve.

At low energies ($\lesssim$ 100 eV) the structure in the curves is very complex, the Bragg features cannot be clearly identified due to the presence of extra peaks. These features, as is more clearly evident in the averaged data in Chapter Seven, occur principally at 1/4 order Bragg positions, e.g., 1-3/4, 2-1/4, etc., and may be identified as multiple scattering in origin as we will discuss later. Dynamical effects also modify the intensity and shape of kinematic features.

At higher energies the curves become more kinematic in appearance; intensities are reduced due to increased thermal scattering, with multiple scattering features being attenuated relative to the kinematic peaks. Attenuation with increasing energy is more rapid than that observed for e.g., copper [93], which seems surprising in view of the higher Debye temperature of silicon. The bulk Debye temperatures of copper and silicon are ~350 °K and ~650 °K respectively. The effect may be explained by a modified top layer spacing in the Si(100)(2 x 1) structure.

Bragg peaks in the (00) beam are produced by interference between electron waves scattered from the top layer and bulk layers. At low energy, contributions from the top layer are approximately in phase with those from the bulk. At higher energy, contributions from the top layer become increasingly out of phase, due to the modified spacing of this layer, 'washing-out' the Bragg peaks and producing broader features with lower intensity.

An increase in the angle of incidence also produces a reduction in intensity. This may be partly due to the reduction in electron

penetration normal to the surface at higher θ, (penetration is proportional to cos θ). The top layer, with its larger vibrational amplitude, then assumes greater weight in the diffraction sum, producing a reduction in intensity by the Debye-Waller factor. In addition the form of the atomic scattering factor plays a part. The scattering factor for a single ion core has in general a large amplitude in the forward direction and a smaller peak in the reverse direction. At small θ, i.e., large scattering angle, the electrons experience the effect of reverse scattering. At higher θ scattered amplitudes are lower until the forward scattering regime is entered.

The reduction in intensity at higher angles of incidence is experienced to a greater degree by the multiple scattering peaks, consistent with the thermal scattering interpretation of intensity reduction.

In addition to the change in overall intensity, angle of incidence changes produce large modifications in structure. Trends can be seen, as clusters of peaks centred about the kinematic positions move upward in energy, following the line of constant momentum transfer in scattering.

Multiple scattering features are very sensitive to changes in scattering parameters; thus at certain energies and angles of incidence the conditions for a multiple scattering event may be satisfied, producing an 'extra' peak in the (00) beam spectrum or robbing a kinematical peak in that beam of intensity. This opening and closing of alternative scattering channels as diffraction parameters are changed modifies the relative intensities of peaks in the spectrum and changes their shape.

Changes in shape occur in features which, though they appear as a single peak, are in fact composed of several overlapping peaks. A modification of the relative intensities of these peaks produces a change in shape of the 'peak' as a whole.

For example, in the set of curves for the <110> azimuth the largely kinematic peak at ~75 eV at $\theta = 18°$ gradually becomes split at increasing angle of incidence as it is crossed by a dynamical scattering condition, re-emerging as a single peak at $\theta = 32°$. In the same set of spectra the 3rd Bragg peak at ~175 eV at $\theta = 8°$ is completely annihilated at $\theta = 16°$ as it is robbed of intensity by a dynamical process. The peak reappears as the angle of incidence is increased to 18° and the conditions for the multiple scattering event are no longer satisfied.

Many similar events may be observed in the profiles presented. It is this complexity of the diffraction process which makes a full dynamical treatment necessary if experimental curves are to be reproduced by model calculations. The effects of multiple scattering events on experimental LEED spectra have been discussed by Seah [5,94].

In comparing curves for different values of azimuthal angle we note that the LEED profiles are much less sensitive to changes in this parameter. In a kinematical model of the diffraction process there should be no change in the (00) beam with change in azimuth since we are effectively looking at diffraction from sets of planes parallel to the surface. The observed changes are therefore due to the effect of a variation in azimuth on multiple scattering conditions,

and here tend to produce relatively small changes in peak shapes and in their relative intensities.

We will not attempt to examine the widths of peaks in these curves in any detail. Many of the 'peaks' are composed of several overlapping peaks. For example Bragg peaks may be flanked by multiple scattering features whose variation in intensity with changes in diffraction parameters produces a variation in the apparent width of the composite peak. We may remark however that the width of the narrowest Bragg peaks increases gradually over the energy range studied, from ~7 eV at 70 eV to ~10 ev at 350 eV. As discussed in Chapter One, the lowest possible width of a kinematic peak is ~2 V_{oi} in consequence of the energy uncertainty introduced by inelastic damping. This would imply a value for the imaginary component of inner potential of from 3 - 5 eV over this energy range. This is a rather lower value than that found for most metals (e.g. [23]) and implies a longer inelastic mean free path.

VIii(b) (1,0) Beam. Intensity-Energy curves for the (1,0) beam for a range of angles of incidence in the <110> azimuth are illustrated in Fig. 5.9. The low energy limit for most non-specular beam curves at higher angles of incidence is determined by the emergence condition for that beam. The energy of emergence at normal incidence is indicated.

By comparison with the (00) beam spectra the structure in these curves is much more complex. The (1,0) beam and other non-specular beams sample momentum transfer parallel to the surface, i.e., in the (1,0) beam case the effect of interference between waves scattered from <110> rows in the surface layer. Atomic displacements or absences in

the top layer producing the (2 x 1) surface net should then produce features within these profiles, so their greater complexity is not unexpected. The bulk of the extra peaks occur at 1/2 order positions, i.e., at values of momentum transfer half way between Bragg peak positions and, as we will discuss later, may be identified with multiple scattering. There is also a good deal of subsidiary structure, the origin of which cannot be established with any certainty.

At higher energies (> 100 eV) the curves become simpler, many of the multiple scattering features are suppressed by their higher Debye-Waller factor relative to Bragg peaks. The 'half order' peaks are still strong however up to 250 eV.

Increasing angle of incidence again weakens dynamical structure. Multiple scattering effects produce splitting and annihilation of Bragg peaks at specific energies and angles of incidence, but in general Bragg features become dominant at angles of incidence greater than 18°.

Widths of the narrowest kinematic peaks in the spectra, where these can be identified, are essentially similar to those noted for the (00) beam. A slight tendency towards broadening is observed which may be associated with changes in atomic spacing parallel to the surface though it may also be due to the strong multiple scattering effects observed in these plots.

All non-specular beam curves exhibit a rather high background level in comparison with the (00) beam, especially in the case of the (1,0) beam. The reason for this is not clear, it may simply be due to the difficulty of collecting non-specular beam data with the Faraday

cup employed in this study. The cup has a rather large aperture and intercepts a 'cone' of background intensity in addition to the beam, as noted by McDonnell [51].

VIii(c) (1,1) Beam. LEED spectra for the (1,1) beam are illustrated in Fig. 5.10, for a range of angles of incidence in the <100> azimuth (ϕ = 45°).

Structure in these curves is simpler than that for the (1,0) beam, though multiple scattering is again strong. The principal extra features occur at approximately 1/4 order Bragg positions. Structure in the curves undergoes similar changes with energy and angle of incidence to those discussed for the (1,0) beam

Peak widths are similar to those for the (1,0) beam.

VIii(d) (1/2,0) Beam. Intensity-Energy spectra for the (1/2,0) beam are presented in Fig. 5.11. The plots were taken for a range of angles of incidence in the <110> azimuth (ϕ = 0°). The curves are dominated by a single peak at low angles of incidence, with some other features, presumably multiple scattering in origin.

In considering the width of the dominant feature at ~64 eV at θ = 0 we note that at normal incidence a shoulder is evident on the low energy side of the peak. If we reject this shoulder as due to multiple scattering and measure the width of the peak that remains, considering it to be approximately symmetric about the highest intensity position, we arrive at a width of ~13 eV, or approximately double the width of peaks at ~70 eV in the (00) beam spectra. This is to be expected since this beam arises only from the (2 x 1) reconstruction

which is likely to be limited to the top layer or certainly a small number of layers. As in the case of optical interference a small number of contributing layers (or beams in the case of optics) leads to a broad interference peak.

VIii(e) (1,1/2) Beam. Fig. 5.12 illustrates LEED profiles for the (1,1/2) beam for a range of angles of incidence in the azimuth, $\phi = 26.5°$. Two major peaks are evident, with additional multiple scattering structure. The width of the narrowest peak at ~50 eV is ~10 eV, wider than peaks at ~70 eV in the (00) beam. Again this width arises from the limited number of contributing layers.

VIii(f) Other Non-Specular Beams. Intensity-Energy spectra for the (2,0), (2,1), (3/2,0) and (3/2,1) beams at normal incidence are presented in Fig. 5.13.

VII. Discussion

Reviewing the data as a whole we note that for all the spectra kinematic features are severely modified by dynamical scattering, especially at low energies.

In addition to the Bragg peaks, other large peaks are observed; in some cases these features are of similar magnitude to the peaks predicted by kinematical theory. We will discuss the origin of these principal features in more detail when we consider the averaged spectra.

We may remark that the positions of the peaks follow the commonly observed behaviour of multiple scattering features, namely 'systematic' sets of peaks at fractional Bragg order positions. This pattern can be related to the periodicity of structure normal to the surface. For

example for the (00) beam f.c.c. (111) surfaces with 3 non-equivalent atomic layers show extra features at 1/3 order positions [51], f.c.c. (100) surfaces with 2 non-equivalent layers exhibit 1/2 order extra features [23]. Thus the f.c.c. (100) diamond structure, with 4 non-equivalent layers might be expected to show extra peaks at 1/4 order positions in the (00) beam, as observed. The systematic fractional order peaks in other beams may be produced by the same mechanism.

The overall intensity of the various beams is from $1 - 4 \times 10^{-3}$ measured at the 'highest point' of each spectrum, and expressed as a fraction of the incident beam. Intensities are somewhat lower than the value observed for Cu(100) by McDonnell [51,93] using the same equipment. This reflects the atomic numbers of silicon and copper, 14 and 29 respectively. Elements with higher Z have, in general, higher scattering factors due to their deeper ion cores.

In all the curves we observe the effect of the Debye-Waller factor, which as discussed in Chapter One produces a reduction in intensity with increasing energy. A higher electron energy implies a greater momentum transfer on scattering and thus an increased Debye-Waller factor. In a multiple scattering process an electron experiences this reduction in scattering factor at each scattering event. Thus intensities due to multiple scattering processes are reduced relative to single scattering peaks, producing the more kinematic appearance of profiles at higher energy.

Another mechanism also acts to 'simplify' I-V spectra at higher energy. At higher incident energies electrons penetrate further into the crystal.

The collected intensity is a summation over scattering events in the top reconstructed layer, together with scattering arising from more bulk-like layers deeper in the crystal. Increased penetration gives greater weight to these deeper layers in the sum, resulting in an intensity spectrum which is rather more like what would be expected for diffraction from the bulk structure.

As noted above the effects of the phase difference introduced by the reconstructed top layer tend to wash out higher energy Bragg peaks producing a rather more rapid attenuation with increasing energy than is typically observed for unreconstructed metals.

Studying the angular evolution of the various beams we observe a substantial reduction in intensity at higher angles of incidence, as discussed above, together with a weakening of dynamical features relative to kinematic peaks.

VIII. The Value of the Data

We have presented a comprehensive set of Intensity-Energy spectra for the Si(100)(2 x 1) surface. The size of the data set was largely determined by the requirements of the CMT Averaging procedure. A wide range of data is also valuable for comparison with spectra calculated by the dynamical method; in particular evolutions of curves as a function of angle of incidence provide a more rigorous test of multiple scattering approaches as well as alleviating problems due to errors in θ. In the past limited comparisons of one or two curves have sometimes led to misleading conclusions regarding the surface structure.

In view of the former unreliability of some LEED intensity data it is worthwhile to review the 'confidence factor' of these results. In comparisons with two separate sets of data obtained by Ignatiev and Jona, and Debe and Johnson, respectively, we find very good agreement in almost all cases where the data sets overlap. A study of all three sets of data, together with comparisons of curves, is to be published [81].

CHAPTER SIX

THE SI(100)(1 x 1) HYDROGEN STRUCTURE

I. Hydrogen Adsorption

In this work it was observed that adsorption of atomic hydrogen on the (2 x 1) structure produced a (1 x 1) pattern. We have characterised the structure produced as Si(100)(1 x 1)H [95].

Ii. Surface Characterisation

Initial experiments in the work with hydrogen were undertaken in order to characterise the adsorption in terms of exposure required to produce the (1 x 1)H structure. The gas-handling system was used in the same way as for argon bombardment. In this case, however, a trapped rotary pump was used to back the diffusion pump, since the zeolite sorption pump showed a very low pumping speed for hydrogen. During early adsorption experiments relatively high levels of H_2O and OH were observed in mass spectrometer analyses of the gas in the system; presumably these gases were produced by reaction of hydrogen with oxygen adsorbed on the walls of the chamber. In order to condense out these impurities liquid nitrogen was circulated through the cooling coils of the sublimation pump.

Following cleaning and annealing of the silicon surface to produce a well-ordered (2 x 1) structure hydrogen was admitted to the system to a pressure, as indicated by the ion gauge, of ~5 x 10^{-6} Torr. Since the gauge is calibrated for nitrogen, this indicates a true pressure of ~1.5 x 10^{-5} Torr. The ion gauge (previously thoroughly

outgassed) was left on during this work, with an electron emission of 0.1 mA, producing the atomic species by dissociation at the filament and by electron bombardment. The specimen surface faced the gauge at a distance of ~20 cm. The specimen was held at room temperature (~20 °C) during adsorption.

After each exposure hydrogen in the system was pumped out and the LEED pattern observed. Increasing exposures produced intermediate structures on the surface; 1/2 orders in the (2 x 1) pattern disappeared and faint 1/4 orders appeared. I-V spectra of these disordered surfaces resembled those obtained from partially annealed surfaces. Further exposure produced a bright (1 x 1) pattern with well-defined spots and very low background intensity, indicating a well-ordered surface structure. Photographs of this pattern are shown in Fig. 6.1. The exposure required to produce the stable (1 x 1) structure was determined to be ~3 x 10^{-4} Torr min. (corrected pressure; H_2 + H). Increased exposures of up to three times this value produced no further structural changes, I-V spectra were unchanged, suggesting saturation of coverage at 1 monolayer. The exposure quoted is based on the measured total pressure in the chamber, consisting of both molecular and atomic hydrogen.

Previous work [96,97,98] has indicated that only the atomic species shows significant adsorption on silicon surfaces. The proportion of the atomic species at the specimen surface is unknown. Mass spectrometer analyses indicated a peak height for H of 1/4 to 1/2 that of H_2, however the filament in the ionization source of the mass spectrometer would also produce dissociation of H_2.

outgassed) was left on during this work, with an electron emission of 0.1 mA, producing the atomic species by dissociation at the filament and by electron bombardment. The specimen surface faced the gauge at a distance of ~20 cm. The specimen was held at room temperature (~20 °C) during adsorption.

After each exposure hydrogen in the system was pumped out and the LEED pattern observed. Increasing exposures produced intermediate structures on the surface; 1/2 orders in the (2 x 1) pattern disappeared and faint 1/4 orders appeared. I-V spectra of these disordered surfaces resembled those obtained from partially annealed surfaces. Further exposure produced a bright (1 x 1) pattern with well-defined spots and very low background intensity, indicating a well-ordered surface structure. Photographs of this pattern are shown in Fig. 6.1. The exposure required to produce the stable (1 x 1) structure was determined to be ~3 x 10^{-4} Torr min. (corrected pressure; H_2 + H). Increased exposures of up to three times this value produced no further structural changes, I-V spectra were unchanged, suggesting saturation of coverage at 1 monolayer. The exposure quoted is based on the measured total pressure in the chamber, consisting of both molecular and atomic hydrogen.

Previous work [96,97,98] has indicated that only the atomic species shows significant adsorption on silicon surfaces. The proportion of the atomic species at the specimen surface is unknown. Mass spectrometer analyses indicated a peak height for H of 1/4 to 1/2 that of H_2, however the filament in the ionization source of the mass spectrometer would also produce dissociation of H_2.

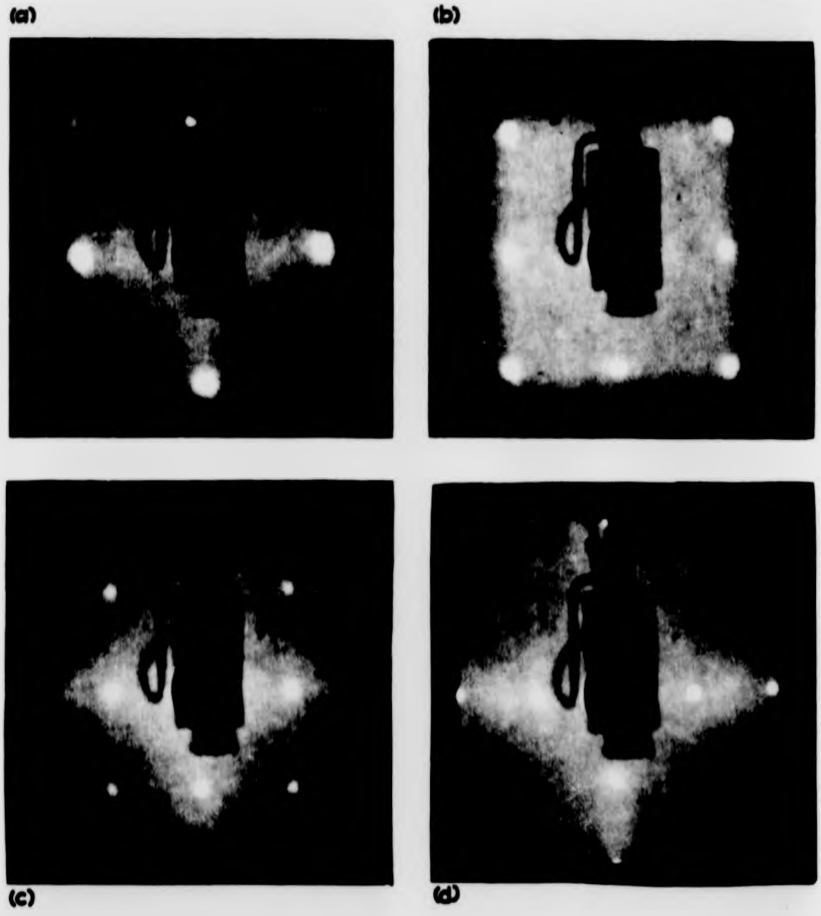

Fig. 6.1 LEED patterns from the Si(100)(1 x 1)H surface. (a) ~42 eV (b) ~52 eV (c) ~75 eV (d) ~100 eV.

Impurity levels in the adsorbing gas were checked at intervals. Analyses indicated that upper limits of impurities present were as follows, at a pressure of ~1.5 x 10^{-5} Torr. Mass peak heights are scaled to an H_2 peak height of 1.

Impurity	Mass Peak Height
He	<.004
H_2O	<.001
CO	<.0005
Others	<.0005

In an attempt to observe adsorption of molecular hydrogen a similar exposure to that referred to above was used; the ion gauge was on only for sufficient time to determine the hydrogen pressure, no change in structure was observed.

Iii. Auger Analysis

Auger spectra from the (1 x 1)H surface before and after data collection showed impurity levels similar to those observed for the clean surface (Of course hydrogen shows no Auger electron emission.). No oxygen was detected on the hydrogen-adsorbed surface. A small increase in the silicon peak at ~74 eV was noted; this is sometimes associated with the appearance of the ~78 eV peak identified with silicon atoms in the oxide. Since the transition involves valence-band states (Table 1: Chapter Three) a similar effect may be produced in the Si-H bound state.

Iiii. Flash Desorption

Qualitative Flash Desorption studies, performed by rapidly heating the specimen to 700 °C - 900°C, indicated that hydrogen desorbed rapidly at these temperatures, with the reappearance of the (2 x 1) structure. Mass spectrometer observations showed a large increase in the hydrogen peak on heating; there was little or no change in the other peaks in the mass spectrum. This is in agreement with the results of Burton [99] who observed thermal hydrogen desorption at 645 °C.

Iiv. Beam Assisted Desorption

In LEED studies of the hydrogen adsorbed surface it was observed that the (1 x 1)H structure became disordered under the influence of high electron beam currents, gradually reverting toward the (2 x 1) structure. Following long exposure to high electron beam fluxes 1/2 order spots began to appear within the pattern. I-V spectra from the disordered surface resembled those obtained from surfaces which were disordered following ion bombardment and insufficient annealing. It is likely that this was due to beam-assisted desorption of hydrogen, as observed by Joyce and Neave [100], allowing portions of the surface layer to revert to the (2 x 1) structure. The superposition of electrons diffracted from (2 x 1) and (1 x 1)H structures results in a partially disordered LEED pattern and I-V spectra which show features characteristic of both surface structures

Iv. Conclusions on Adsorption Work

The results above are in agreement with those of Law, who observed saturation of adsorption of atomic hydrogen, with a drastic reduction

Iiii. Flash Desorption

Qualitative Flash Desorption studies, performed by rapidly heating the specimen to 700 °C - 900°C, indicated that hydrogen desorbed rapidly at these temperatures, with the reappearance of the (2 x 1) structure. Mass spectrometer observations showed a large increase in the hydrogen peak on heating; there was little or no change in the other peaks in the mass spectrum. This is in agreement with the results of Burton [99] who observed thermal hydrogen desorption at 645 °C.

Iiv. Beam Assisted Desorption

In LEED studies of the hydrogen adsorbed surface it was observed that the (1 x 1)H structure became disordered under the influence of high electron beam currents, gradually reverting toward the (2 x 1) structure. Following long exposure to high electron beam fluxes 1/2 order spots began to appear within the pattern. I-V spectra from the disordered surface resembled those obtained from surfaces which were disordered following ion bombardment and insufficient annealing. It is likely that this was due to beam-assisted desorption of hydrogen, as observed by Joyce and Neave [100], allowing portions of the surface layer to revert to the (2 x 1) structure. The superposition of electrons diffracted from (2 x 1) and (1 x 1)H structures results in a partially disordered LEED pattern and I-V spectra which show features characteristic of both surface structures

Iv. Conclusions on Adsorption Work

The results above are in agreement with those of Law, who observed saturation of adsorption of atomic hydrogen, with a drastic reduction

in sticking coefficient at a coverage which he estimated at 1 monolayer [96]. These measurements were for silicon filaments however, rather than a single crystal surface.

Our observation of a (1 x 1) structure is in conflict with the results of Rowe and Ibach [97] however. If we consider the possibility of adsorption of some impurity, the most likely process would appear to be oxidation from the H_2O and OH present. As noted above no oxygen was detected in Auger spectra, and we refer to some early work on oxygen adsorption by the author.

Oxygen coverages in that study were monitored by Auger Electron Spectroscopy, and exposures up to $\geq 10^{-4}$ Torr min. of oxygen were used. Increasing oxygen coverages produced a gradual reduction in the intensity of spots in the (2 x 1) LEED pattern and an increase in the background intensity, but no (1 x 1) structure was produced.

In addition, in the hydrogen work, variation of the partial pressures of H_2O and OH, produced by carrying out adsorption with and without cooling of the sublimation pump, had no significant effect on the exposure required to form the (1 x 1) structure.

We conclude that the (1 x 1) structure is indeed produced by adsorption of atomic hydrogen. This might be expected from chemical considerations if hydrogen saturates dangling bonds at the surface, permitting a stable (1 x 1) structure. Becker and Gobeli [101] observed infrared vibrational spectra of adsorbed atomic hydrogen and found that the frequency was close to the Si-H stretching vibration of SiH_4, suggesting that atomic hydrogen sits on top of the silicon atoms,

bound by a single Si-H bond. This result is in agreement with our observations. Recently a (1 x 1) phase has been reported by Sakurai and Hagstrum [98]. These authors characterise this structure as Si(100)(1 x 1)2H and claim that the hydrogen saturated surface is likely to have two hydrogen atoms attached to each surface layer silicon atom.

II. Data Collection

Following adsorption and the establishment of a sharp (1 x 1)H pattern, data collection was carried out in a similar manner to that used for the (2 x 1) study. In this case the (00) beam spectra were recorded directly into a disc file on the 'G.E.C.' 4080 computer. The system is described in Chapter Two. The computer provided the energy ramp, via a digital-to-analogue converter. Intensities were recorded digitally, with an analogue-to-digital converter connected to the output of the Lock-In amplifier. Simultaneously the recorded intensity was monitored, via a second analogue computer output, to produce an I-V spectrum on the X-Y recorder.

A typical data recording run would then proceed as follows.

The specimen position was set up in the normal way; the angle of incidence setting was made and the Faraday cup positioned as described previously. The LEED program was then called and zeros for intensity and energy scales established and the minimum and maximum values of the energy scale input to the computer for calibration purposes. The intensity amplifier was set to a gain of x1 and the angle of incidence input.

On command the computer then began to ramp the electron energy, storing intensity and energy values and feeding intensity values to the X-Y recorder.

At a prearranged value of energy (~200 eV) the scan would stop for adjustment of the intensity gain to x10 to improve the resolution of the small high energy peaks; the processor was instructed to divide these digital intensity values by 10 to obtain a uniform scale. The scan was then resumed to the upper limit of energy (~580 eV).

The system was then reset and the process repeated. Once the full range of angles of incidence had been covered the computer was instructed to store the set of profiles in a specified disc file. These could then be accessed at any time for normalisation to beam current and averaging.

During the initial setting up procedures for this system I-V profiles were checked against those plotted manually to ensure that the computer-produced data was accurate, particularly for peak positions and shapes.

Non-specular beam data was plotted manually on the X-Y recorder, and digitised as described for the (2 x 1) data.

LEED beam currents used for this study were somewhat lower than those employed previously, in order to minimise desorption of hydrogen by the beam. The typical beam current was ~0.22 μA at 80 eV. Other experimental parameters were essentially the same as those for the (2 x 1) study.

(00) beam spectra were recorded over an energy range 20 eV to ~500 eV for angles of incidence from 8° - 32° in 2° steps, in each of

the azimuths, ϕ = 0 (<110>), 22.5°, 26.5°, 35°, 45° (<100>). The (1,0) and (1,1) beams were plotted for angles of incidence from 0 - 30° in 2° steps, in the <110> and <100> azimuths respectively. An Intensity-Energy spectrum was also plotted for the (2,2) beam at normal incidence.

III. Surface Conditions During Experiment

Auger spectra taken during initial experiments to determine adsorption conditions indicated that contaminant levels were similar to those on the clean (2 x 1) surface. During data collection Auger spectra were monitored only after LEED data had been obtained, to avoid desorption of hydrogen by the high energy and beam current required for accurate Auger studies. Impurity levels were typically characterised by a carbon to silicon peak height ratio of $\sim 2 \times 10^{-3}$, and this was never greater than 5×10^{-3}. Other impurities, if present, were below the noise level in Auger spectra, $\sim 1 \times 10^{-3}$ times the silicon peak height.

As in the (2 x 1) study some disordering of the surface was observed during experimental runs, in this case due to beam assisted desorption. LEED data was obtained only from surfaces exhibiting a change in relative peak heights of less than 10% from the fully ordered state.

IV. LEED Intensity-Energy Data

Normalised Intensity-Energy plots were produced by the 'Elliott' 4130 computer. The energy resolution for non-specular beam curves is variable, with a fine resolution of 0.5 eV in regions where the curves exhibit high rates of change. (00) beam curves have an energy resolution

of 0.5 eV in the range 20 eV to ~200 eV, 1 eV from ~200 eV to ~450 eV. Peak positions in all curves are defined to within similar limits. Intensity resolution is typically 0.2% for the larger peaks to ~1% for the smaller features. In a discussion of the accuracy of the curves, similar comments to those for the (2 x 1) data apply.

The spectra are presented in Figs. 6.2 to 6.9. No correction for inner potential has been made; kinematic peaks are therefore shifted downwards in energy by ~10 eV. Intensity scales are labelled as a fraction of the incident beam.

IVi. The (00) Beam

Intensity-Energy spectra for the (00) beam are presented in Figs. 6.2 to 6.6 for a range of angles of incidence in each of five azimuths. Bragg peak positions for the bulk structure are indicated.

Features predicted by kinematic theory are dominant in these profiles, though the second Bragg peak is modified in shape by dynamical features. Extra peaks are observed, principally at 1/4 order positions as for the (2 x 1) curves, and 1/2 order positions. The 1/4 order features are much weaker than their counterparts in the clean surface data.

The overall intensity into the (00) beam, measured as the average value of the 2nd Bragg peak height over the five azimuthal angles is $\sim 4.6 \times 10^{-3}$, compared with a value for the (2 x 1) (00) beam of $\sim 4.0 \times 10^{-3}$. This intensity difference may not be significant because of the difficulty in measuring the beam current accurately. However the lower intensity in (2 x 1) Bragg peaks may be accounted for by the large extra peaks in those results, diverting intensity from the Bragg features.

of 0.5 eV in the range 20 eV to ~200 eV, 1 eV from ~200 eV to ~450 eV. Peak positions in all curves are defined to within similar limits. Intensity resolution is typically 0.2% for the larger peaks to ~1% for the smaller features. In a discussion of the accuracy of the curves, similar comments to those for the (2 x 1) data apply.

The spectra are presented in Figs. 6.2 to 6.9. No correction for inner potential has been made; kinematic peaks are therefore shifted downwards in energy by ~10 eV. Intensity scales are labelled as a fraction of the incident beam.

IVi. The (00) Beam

Intensity-Energy spectra for the (00) beam are presented in Figs. 6.2 to 6.6 for a range of angles of incidence in each of five azimuths. Bragg peak positions for the bulk structure are indicated.

Features predicted by kinematic theory are dominant in these profiles, though the second Bragg peak is modified in shape by dynamical features. Extra peaks are observed, principally at 1/4 order positions as for the (2 x 1) curves, and 1/2 order positions. The 1/4 order features are much weaker than their counterparts in the clean surface data.

The overall intensity into the (00) beam, measured as the average value of the 2nd Bragg peak height over the five azimuthal angles is ~4.6×10^{-3}, compared with a value for the (2 x 1) (00) beam of ~4.0×10^{-3}. This intensity difference may not be significant because of the difficulty in measuring the beam current accurately. However the lower intensity in (2 x 1) Bragg peaks may be accounted for by the large extra peaks in those results, diverting intensity from the Bragg features.

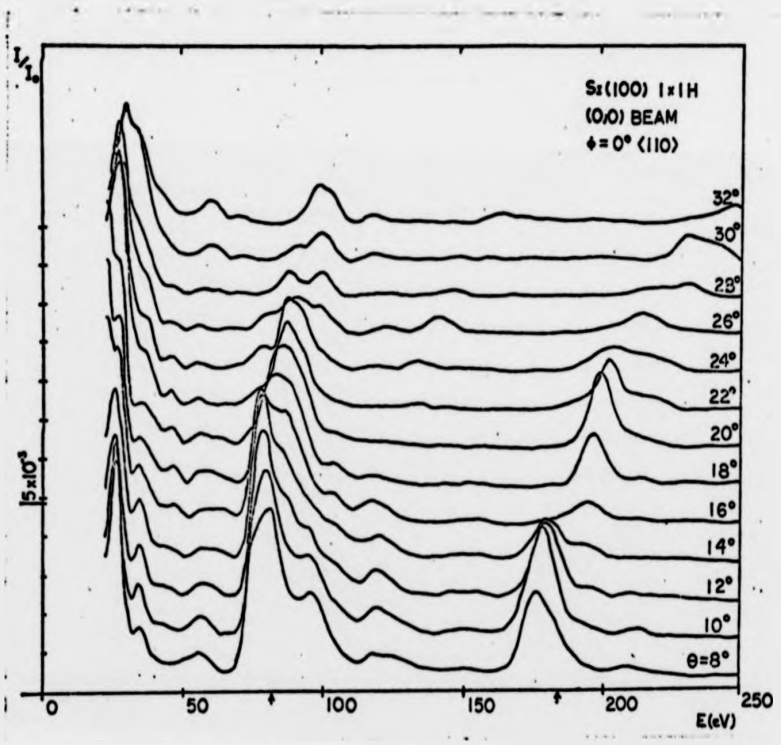

Fig. 6.2 Intensity-Energy spectra for the Si(100)(1 x 1)H surface. (00) beam, ϕ = 0°. ↑ indicates bulk Bragg positions at normal incidence.

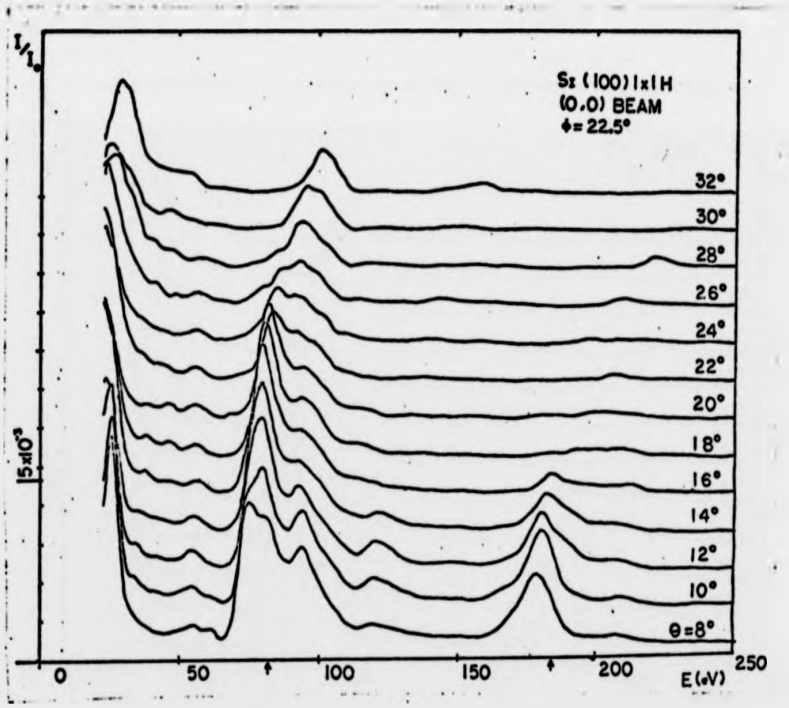

Fig. 6.3 Intensity-Energy spectra for the Si(100)(1 x 1)H surface. (00) beam, ϕ = 22.5°. ↑ indicates bulk Bragg positions at normal incidence.

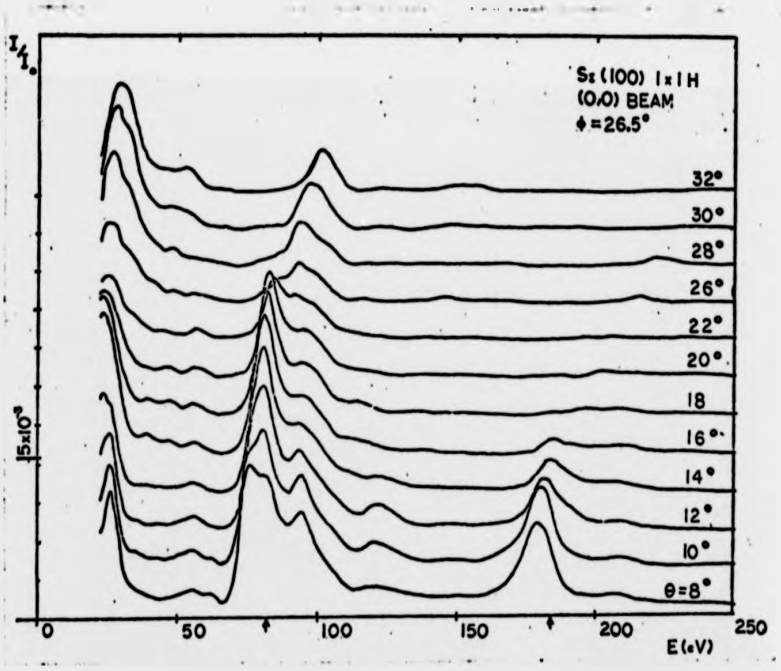

Fig. 6.4 Intensity-Energy spectra for the Si(100)(1 x 1)H surface. (00) beam, $\phi = 26.5°$. † indicates bulk Bragg positions at normal incidence.

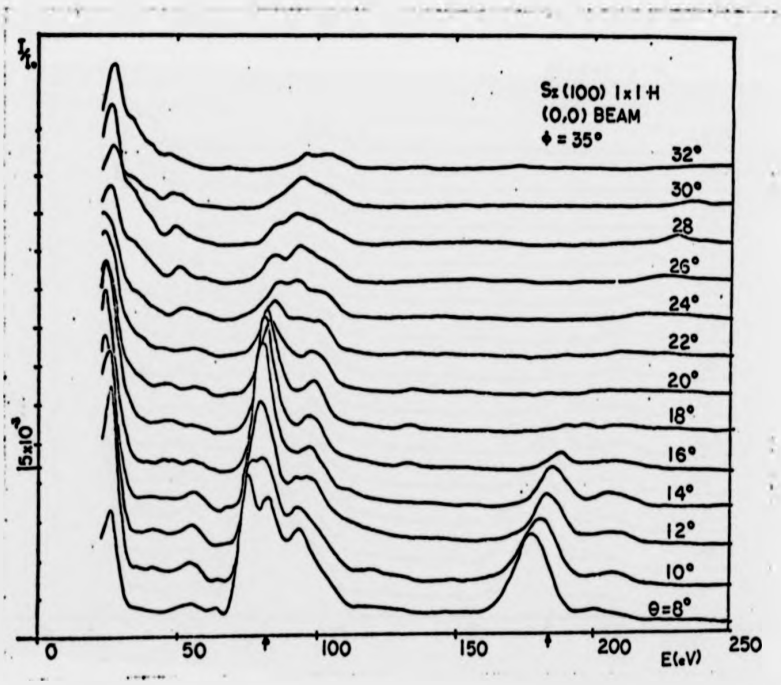

Fig. 6.5 Intensity-Energy spectra for the Si(100)(1 x 1)H surface. (00) beam, ϕ = 35°. ↑ indicates bulk Bragg positions at normal incidence.

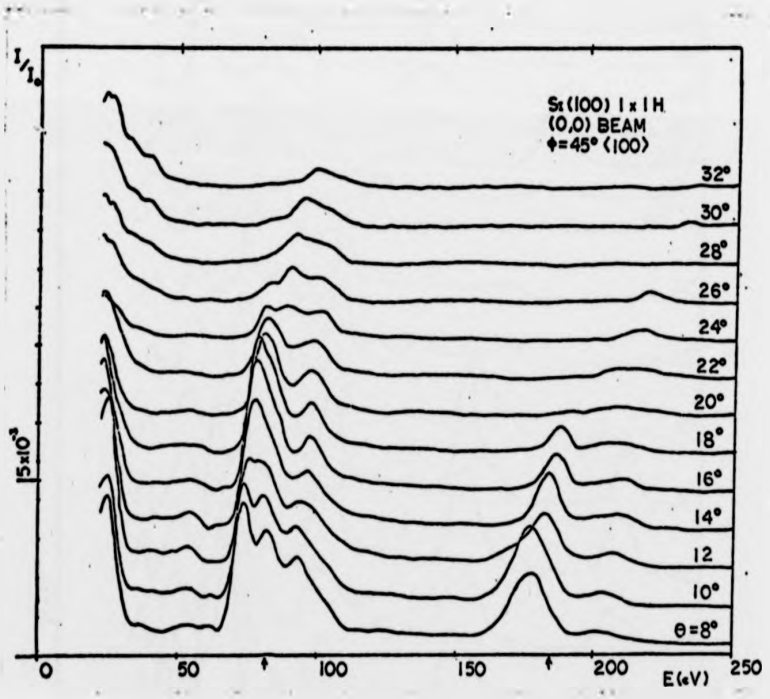

Fig. 6.6 Intensity-Energy spectra for the Si(100)(1 x 1)H surface. (00) beam, ϕ = 45°. ↑ indicates bulk Bragg positions at normal incidence.

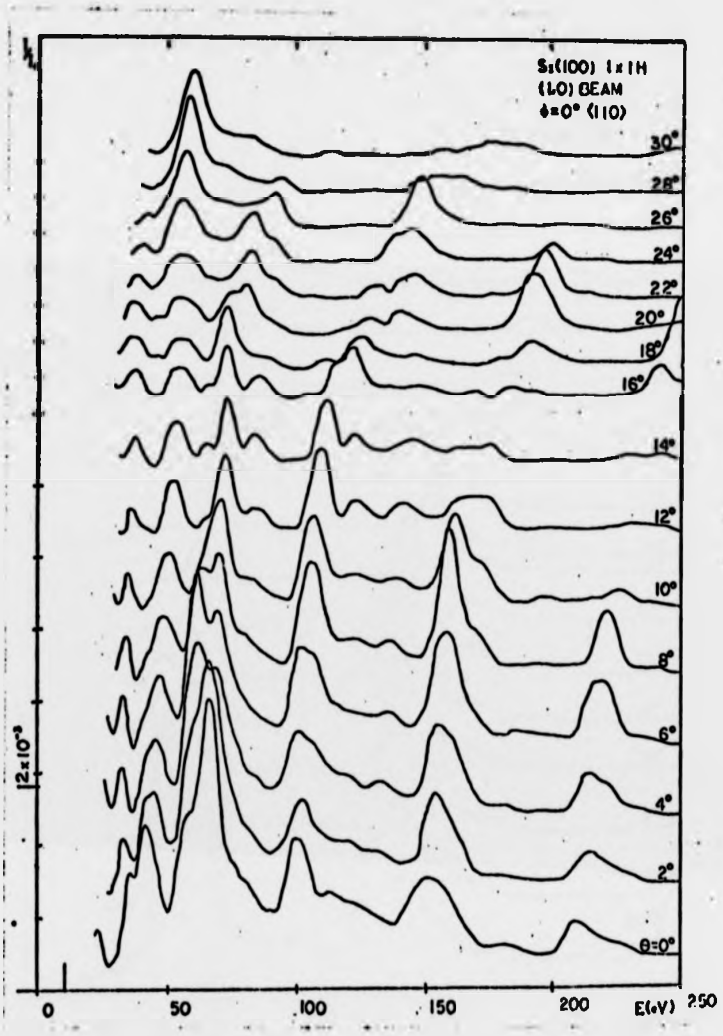

Fig. 6.7 Intensity-Energy spectra for the Si(100)(1 x 1)H surface. (1,0) beam, $\phi = 0°$.

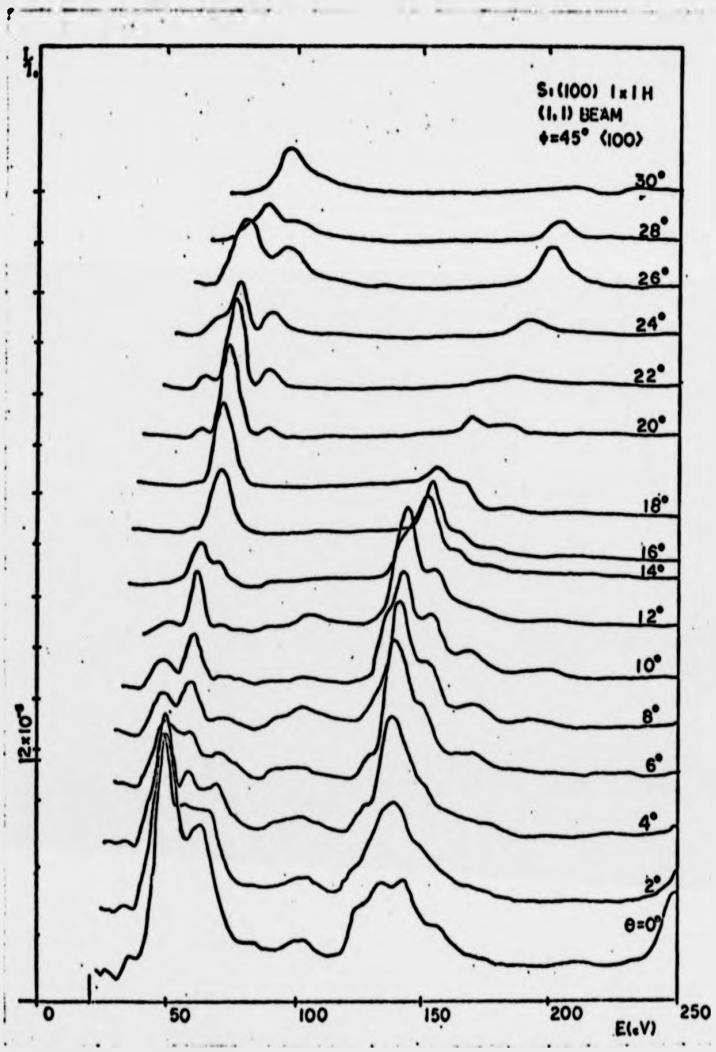

Fig. 6.8 Intensity-Energy spectra for the Si(100)(1 x 1)H surface. (1,1) beam, $\phi = 45°$.

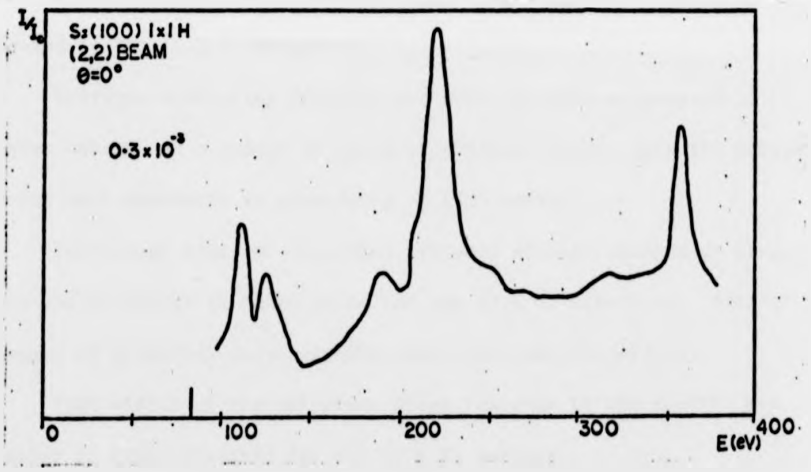

Fig. 6.9 Intensity-Energy spectra for the Si(100)(1 x 1)H surface. (2,2) beam. The intensity figure on the left refers to the maximum height of the curve.

Increasing electron energy produces the expected reduction in diffracted intensity due to thermal scattering. The attenuation is weaker for (1 x 1)H spectra than for the (2 x 1) curves; for example, while the second Bragg peak in the (00) beam is of approximately equal intensity in the two sets of curves, the 3rd Bragg peak at low angles of incidence in (1 x 1)H profiles is approximately twice the size of its counterpart in (2 x 1) data. As discussed previously this may be the result of phase differences introduced by a modified top layer spacing in the (2 x 1) structure.

Multiple scattering features are more strongly attenuated at higher energy, as a result of the Debye-Waller factor, thus the curves become more kinematic in appearance at high energy.

Increasing angle of incidence produces similar changes in structure and intensity to those noted for the (2 x 1) structure. Similarly changes of azimuthal angle produce relatively smaller effects.

Peak widths of the narrowest Bragg features in the spectra are similar to those observed for the (2 x 1) surface.

IVii. Non-Specular Beams

Non-specular beam LEED profiles are illustrated in Figs. 6.7 and 6.8, covering a range of angles of incidence in the <110> and <100> azimuths, for the (1,0) and (1,1) beams respectively. A profile for the (2,2) beam at normal incidence is presented in Fig. 6.9.

In both the (1,0) and (1,1) beams kinematic peaks dominate the curves, though the (1,0) beam exhibits some strong extra features at low energy. The extra peaks are observed principally at 1/2 integral Bragg orders as in the (2 x 1) case.

Multiple scattering effects also produce modifications to kinematic peaks in both these beams.

The effects of increasing energy and angle of incidence are similar to those noted for the (00) beam, as are the peak widths.

V. Discussion

Reviewing the data for the (1 x 1)H structure we note that in general Intensity-Energy curves are much simpler than those for the (2 x 1) surface. The single scattering Bragg peaks can be easily identified in most cases, the extra features are absent or considerably weakened. Those extra peaks which are evident are in similar positions to those for the clean reconstructed surface. The relative intensities are modified however; for example 1/4 order features in the (1 x 1)H (00) beam spectra are much weaker than those in the (2 x 1) data though the 1/2 orders are of similar height. If these features are due to multiple scattering this behaviour would seem to be linked to the structure-related systematic appearance of multiple scattering features discussed previously; it implies that dynamical peaks are much more strongly structure dependent than the Bragg features. We will discuss the origin of the extra features and their implications for a structural model in detail in conjunction with an examination of the CMT averaged data. The other commonly observed effects of multiple scattering are evident in these spectra, in the form of modification of kinematical peaks.

A higher diffracted intensity than for the (2 x 1) surface is observed in all the beams studied. Since this intensity is measured as the height of Bragg peaks in the profiles the difference between the two

structures may be due to the large extra peaks in the (2 x 1) spectra robbing Bragg features of intensity. These intensity measurements, however, emphasise the highly ordered nature of the (1 x 1)H structure. Attenuation of the spectra as the electron energy is increased is observed in the (1 x 1)H data as expected, though the effect is not as pronounced as in the (2 x 1) case, particularly for the (00) and (1,1) beam spectra, for reasons discussed above. Again the curves become more kinematic in appearance at higher energy, as multiple scattering peaks experience greater attenuation than single scattering features.

Increasing angle of incidence also reduces diffracted intensity as a result of reduced penetration and the form of the atomic scattering factor.

VI. Structural Implications

As we mentioned previously, a number of models of the Si(100) (2 x 1) reconstruction have been proposed. Most of these models involve reconstruction of the top layer only. Our observation of the (1 x 1)H structure formed by atomic hydrogen adsorption would appear to support this type of model, as opposed to one which requires large migrations of atoms from their bulk positions.

We assume that the (1 x 1)H structure is essentially similar to that of the bulk, possibly with some adjustment of the top layer spacing as observed for many clean metal surfaces. Hydrogen adsorption makes this structure stable by saturating the dangling bonds at the surface. A model of electron diffraction by this structure may then neglect scattering by hydrogen atoms, since their scattering factor is expected

to be much smaller than that for silicon atoms by virtue of their lower atomic number. The simplicity of the LEED profiles from the (1 x 1)H surface lends support to this interpretation of surface structure and scattering, which will be discussed further in consideration of the averaged data.

On exposure to atomic hydrogen at room temperature the (2 x 1) structure rapidly changed to the (1 x 1)H form. This observation implies that the potential barrier to be surmounted for 'unreconstruction' to occur is relatively weak; the most probable (2 x 1) structure is then one in which atomic displacements from the bulk structure are small.

This view of the reconstruction particularly favours the 'leaning rows' model discussed earlier [1,3], in which adjacent <110> rows move together to form pairs. Other models involving small displacements of atoms within the surface layer are also possible.

Vacancy models [2,4], are thought unlikely on this basis, since significant mass transport would be involved in unreconstruction

Again, we will discuss the (2 x 1) reconstruction in more detail in the following chapter.

VII. The Value of the Data

The principal value of LEED data for the (1 x 1)H surface structure lies in its use for determination of the (2 x 1) structure.

There is now a large body of reliable experimental data available for the (2 x 1) surface [81], but at present theoretical workers have had little success in producing calculated curves which show reasonable agreement with experiment. In view of this difficulty it would be

valuable to confirm the scattering model used before attempting determination of the possibly complex reconstruction of the clean surface. Evidently this 'test case' would ideally consist of a (1 x 1) surface with essentially no modification from the bulk structure. The (1 x 1)H structure would appear to offer the closest possible approach to this situation. We may therefore use data from this surface to establish non-structural parameters, such as the ion-core potential and the imaginary, damping component of inner potential, in a theoretical model of electron scattering.

Averaged data performs a similar role, as the basis for comparison with averages for the (2 x 1) surface. Analysis of averaged (1 x 1)H data enables us to determine the non-structural parameters appropriate for a single scattering calculation in an attempt at (2 x 1) structure determination by the CMTA method.

VIIi. Comparison with Theory

In Fig. 6.10 we present comparisons of selected experimental spectra for the (1 x 1)H surface with profiles calculated for a (1 x 1) (bulk) structure by Jona *et al.* [102].

An exact comparison is not possible. Theoretical curves are calculated for an angle of incidence of 5° in the ϕ = 45° <100> azimuth. Our spectra are at angles: for the (00) beam θ = 8°, the lowest angle of incidence for which we have data; for the (1,1) beam θ = 4° and 6°. Both beams are recorded for ϕ = 45°. In the case of the (1,0) beam our data is in the ϕ = 0° <110> azimuth, for θ = 4° and 6°.

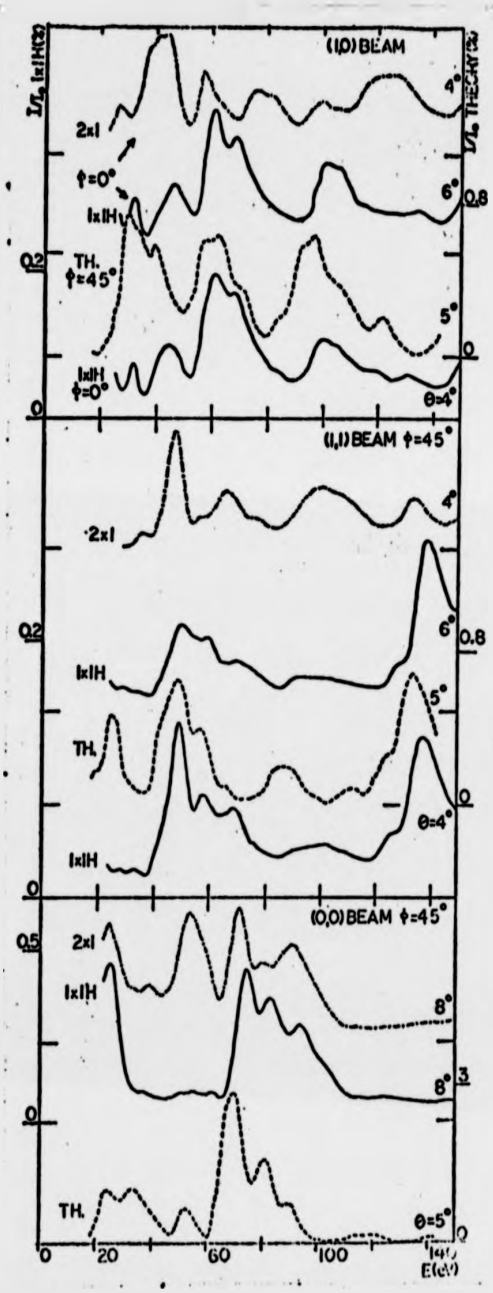

Fig. 6.10 Comparisons of experimental LEED spectra for the (1 x 1)H and (2 x 1) structures with theoretical profiles calculated for the bulk structure by Jona *et al.* [102]. ——— expt (1 x 1)H; —·—·—·—·— expt (2 x 1); – – – – – – theory.

Despite these differences in angle we find some agreement, particularly for the (00) and (1,1) beams. In the (00) beam the triplet structure near the second Bragg condition at ~80 eV is reproduced in the theoretical profiles. Similar structure at ~60 eV in the (1,1) beam is reproduced, as is the peak at ~140 eV together with its shoulder on the low energy side. In the case of the (1,0) beam agreement is not good, this is not surprising in view of the difference in azimuth.

We note that agreement between theoretical and experimental profiles would be improved by a uniform shift of calculated curves upwards in energy by ~2 - 5 eV. This may be accounted for by a different inner potential value for theoretical spectra. Contact potential differences, which we have not corrected for in experimental data, may produce errors of 1 - 2 eV. In addition we may ascribe some of the energy shift to the contraction of the top layer spacing in the (1 x 1)H structure, discussed later, which will tend to produce shifts of peaks toward higher momentum transfer (higher energy) positions. Addition of this contraction to the theoretical model may produce better agreement with experiment.

The agreement achieved indicates that scattering parameters are reasonably well accounted for in the theoretical model. The large differences between these (1 x 1) curves and the (2 x 1) spectra (see Fig. 6.10) indicate considerable sensitivity to surface structure in both experiment and theory. With some refinement of theory it should now be possible to reproduce the (2 x 1) surface data and to determine the atomic structure of this surface.

CHAPTER SEVEN

CONSTANT MOMENTUM TRANSFER AVERAGING

I. Introduction

In this chapter we will discuss the application of Constant Momentum Transfer Averaging to the LEED data, and some of the conclusions which the analysis enables us to form about the nature of the clean and hydrogen adsorbed Si(100) surfaces.

As we have noted previously the (1 x 1)H surface may be interpreted as an essentially bulk-like structure. It seems probable that the adsorbed hydrogen atoms may simply saturate the dangling bonds at the surface, stabilising the formation of this simple structure.

We adopt a model of the scattering in which the hydrogen atoms are neglected in the analysis by reason of their small atomic scattering factors. The only unknown factor in a structural model is then the top silicon layer spacing.

It is quite possible, as we may infer from LEED studies of the materials, that this spacing is somewhat different from the bulk layer spacing.

Analysis of the results for this simple structure enables us to determine the values of the important non-structural parameters in a kinematic calculation. We will therefore discuss the (1 x 1)H CMTA results first, going on to examine the more complex (2 x 1) structure, with the former results as a basis for comparison.

II. Averaging Procedure

Data averaging for the (1 x 1)H and (2 x 1) data was carried out on the 4080 computer. The normalised I-V spectra, consisting of a series of points with intensity and energy coordinates, were converted to plots of intensity versus $S_\perp$, the momentum transfer normal to the surface.

$$\frac{S_\perp}{S_o} = \frac{2|\underset{\sim}{K}|}{g_\perp} \cos\left(\frac{\theta' + \theta}{2}\right) \cos\left(\frac{\theta' - \theta}{2}\right)$$

where $g_\perp$ is a reciprocal lattice vector normal to the surface (i.e., $g_\perp = \frac{2\pi}{d}$ where d is the plane spacing). θ is the angle of incidence, θ' the diffracted angle. These angles are measured inside the crystal; they may be identified with angles outside the crystal (θ_o) using the correction for refraction by the inner potential:

$$\sin\theta = \frac{\sqrt{E}\sin\theta_o}{\sqrt{E + V_o}}$$

Intensity values at given S were then added. Plots of intensity versus $S_\perp/S_o$ were produced using the 4130 computer. S_o is the momentum transfer corresponding to constructive interference between adjacent (100) layers in the bulk silicon structure; the spacing of these layers is 1.358 Å, 1/4 of the unit cell dimension in this direction. This corresponds to the 1-dimensional Bragg notation used previously; Bragg order 1 for the (00) beam is a 400 type reflection in 3-dimensional notation. Non-specular beams are labelled in Bragg order relative to the (00) beam.

The inner potential value chosen is 10 eV. This choice is such that the highest order Bragg peak (the 4th in the (00) beam averaged spectrum) occurs at almost exactly the ideal value for both the clean and hydrogen adsorbed surfaces. The high-order Bragg peaks are the most kinematic and thus less likely to be shifted by multiple scattering. In addition these peaks are insensitive to the model structure chosen; owing to the increased electron penetration at these higher energies their position is largely dominated by the bulk structure. The effect of the choice of inner potential is illustrated in Fig. 7.1. We note that peak shapes in the (00) beam are little affected by the choice of inner potential in the range 0 - 20 eV, and that peak positions are essentially constant for small changes (1 - 2 eV) of this parameter

The same value of inner potential is used for averages for both surfaces. Work function changes on hydrogen adsorption are unlikely to be greater than 1 eV. Measurements of the photoemission threshold for the Si(111) surface by Eisinger [103], indicated a difference of <0.4 eV between clean and hydrogen saturated surfaces.

As we remarked in the review of LEED theory, the inner potential is expected to be energy dependent. In the absence of accurate knowledge of this variation, and in view of the weak dependence of peak shapes and positions on the value chosen, we conclude that a constant value of 10 eV is satisfactory for the purposes of this analysis.

III. The (1 x 1) Structure

Averaged LEED spectra for the (1 x 1)H structure are illustrated in Fig. 7.2

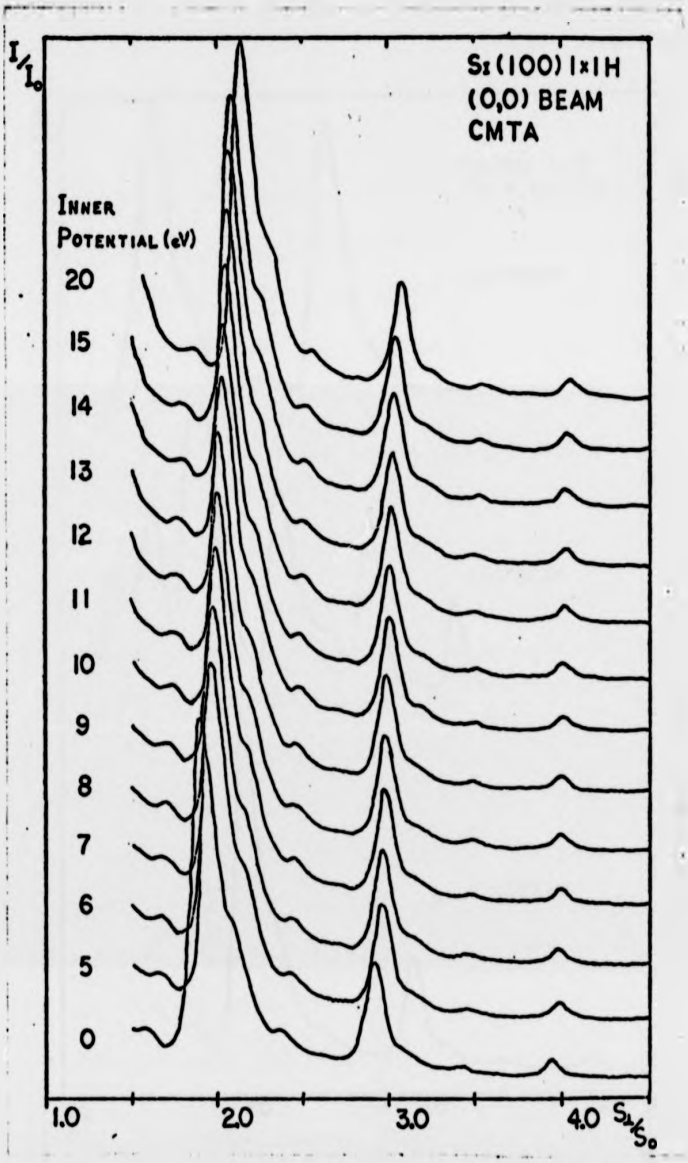

Fig. 7.1 The effect of inner potential on the CMT average, for the (1 x 1)H (00) beam.

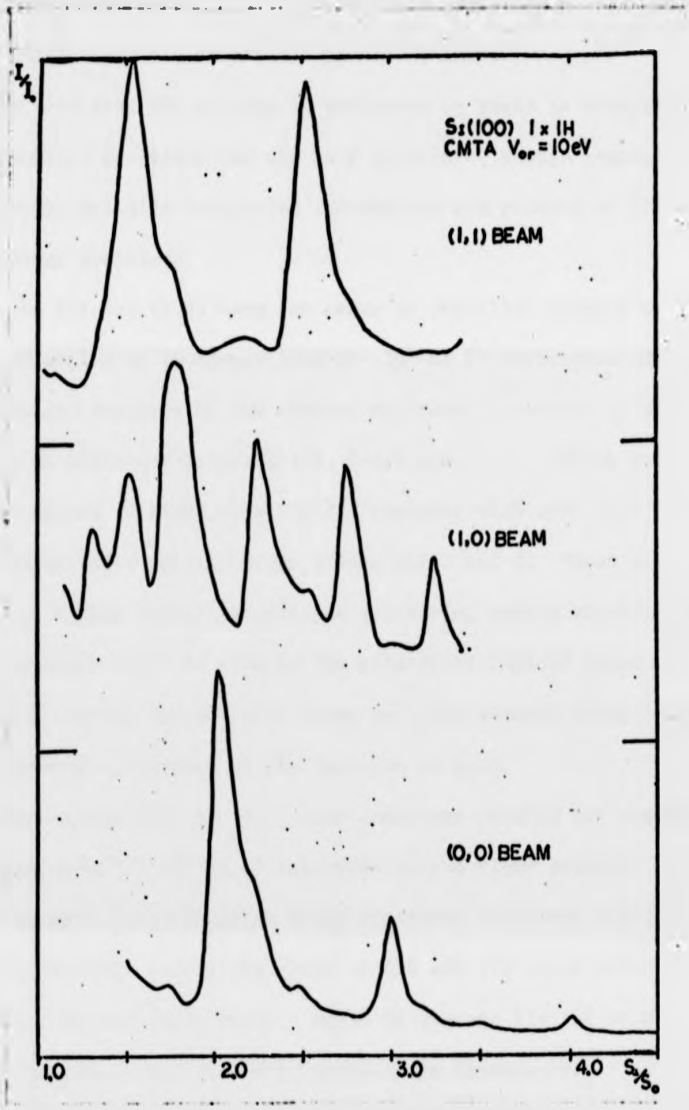

Fig. 7.2 Constant Momentum Transfer averaged spectra for the Si(100)(1 x 1)H surface. (00), (1,0) and (1,1) beams. The inner potential is 10 eV.

The (00) beam average is composed of spectra for a range of angles of incidence from 8° - 32° in 2° intervals, for each of five azimuths ϕ = 0 (<110>), 22.5°, 26.5°, 35° and 45° (<100>).

We note that the average is dominated by peaks in approximately the kinematic positions for the bulk structure, though remnants of, presumably, multiple scattering information are present at 1/4 and 1/2 order Bragg positions.

Data for the (1,0) beam was taken in the <110> azimuth over a range of angles of incidence from 0 - 30° at 2° intervals. Once again the dominant features in the average are those predicted by kinematic theory, at positions 1-3/4, 2-1/4, 2-3/4 and 3-1/4, though a strong feature occurs at Bragg order 1-1/2, together with weak "1/2 order" features at approximately Bragg orders 2-1/2 and 3. These extra peaks are almost certainly multiple scattering events which have not fully averaged out. In view of the relatively limited range of averaging carried out for this beam, only one azimuth being included, the kinematic appearance of the spectrum is good.

The average for the (1,1) beam comprises results for angles of incidence from 0 - 30° at 2° intervals in the <100> azimuth. Kinematic peaks dominate the average at Bragg positions 1-1/2 and 2-1/2, with residual multiple scattering peaks at 1/4 and 1/2 order intermediate positions between these peaks. Again an average limited to only one azimuth yields a spectrum very kinematic in appearance.

IIIi. Discussion

Constant Moment Transfer averaged LEED spectra for the (1 x 1)H structure are highly kinematic in appearance, though with some extra features. These peaks follow the commonly observed behaviour for multiple scattering features discussed previously, namely systematic sets of peaks at fractional orders. Thus the (00) beam curve exhibits 1/4 order features after averaging, corresponding to the 4 non-equivalent layers in the f.c.c. (100) diamond structure. We conclude that the extra peaks are due to dynamical processes which have not been fully eliminated by the averaging process.

IIIii. Structural Analysis

The results of the averaging process appear to be consistent with the structural model discussed above, with dominant peaks occurring at or near the kinematic positions for the bulk structure. The principal effect of expansion or contraction of the surface silicon layer spacing will be to modify peak positions and shapes. For example contraction produces shifts of peaks to higher momentum transfer positions and shoulders on the high $S_\perp$ side of these peaks. Examination of the averages shows that peaks tend to occur at positions slightly above the ideal bulk values of momentum transfer and that there is evidence of high $S_\perp$ shoulders, though these may be due in part to residual multiple scattering features. Thus contraction of the surface layer is indicated. In order to determine the degree of contraction it is necessary to carry out a full kinematic calculation with parameters suggested by the experimental data.

The calculation was carried out by Woodruff [104], and for full details we refer the reader to the reference cited.

The kinematic calculation included a model of the silicon atomic scattering factor described by seven phase shifts. Scattering by hydrogen atoms was neglected. Thermal effects were included by means of the Debye-Waller factor.

The relative values of Debye temperature chosen for the surface layer (θ_{DO}) and substrate (θ_{DS}) respectively, prove to be significant in terms of sensitivity to the surface layer. A smaller θ_{DO}/θ_{DS} weakens surface layer scattering relative to the bulk. A surface mean square vibrational amplitude of twice the bulk value was chosen, a value typical of most metals. This imples a surface layer Debye temperature of 465 °K for a bulk value of 658 °K.

The imaginary component of inner potential, which simulates the effect of both elastic and inelastic damping in this approach, was chosen by fitting peak widths and varied from 2 eV to 8.7 eV in the energy range 25 - 400 eV. This value is somewhat less than that typical for metals, e.g., Cu [23], and implies a longer mean free path.

A wide range of surface layer spacings was investigated. Comparisons of peak positions between calculated and experimental curves were inconclusive, in that agreement could be found for most peaks for a range of contracted layer spacings by suitable choice of inner potential. Inspection of peak shapes was more instructive. As we have noted the choice of inner potential has very little effect on the shapes of peaks. The criterion for agreement was based largely on the

size of the high $S_{\perp}$ peak shoulders. It was concluded that the best agreement between the model calculations and experimental averages occurs for a surface layer contraction of 3% ± 3%.

IV The (2 x 1) Structure

Averaged Intensity-Energy spectra for the (2 x 1) structure are illustrated in Figs. 7.3 and 7.4. These averages were compiled from exactly the same range of data used for the (1 x 1)H study.

Considering the (00) beam average we note that strong features occur at approximately the positions predicted by kinematic theory. In addition there are other large peaks at 1/4 and 1/2 order positions, these features are in general slightly broader than the kinematic features.

The (1,0) beam average is markedly non-kinematic in appearance. Peaks predicted by kinematic theory occur at approximately Bragg orders 1-3/4, 2-1/4 and 2-3/4, with very strong features at Bragg orders approximately halfway between the former peaks. The extra peaks are slightly broader than the Bragg peaks in the spectrum.

In the (1,1) beam average kinematic peaks are observed at approximately the expected positions, Bragg orders 1-1/2 and 2-1/2. In this case however, the spectrum is dominated by extra peaks at approximately 1/4 order positions between these features. Again the extra peaks are somewhat broader than the kinematic peaks.

The average for the (1/2,0) beam is presented in Fig. 7.4, it is composed of spectra for a range of angles of incidence from 0 - 30° at 2° intervals in the <110> azimuth.

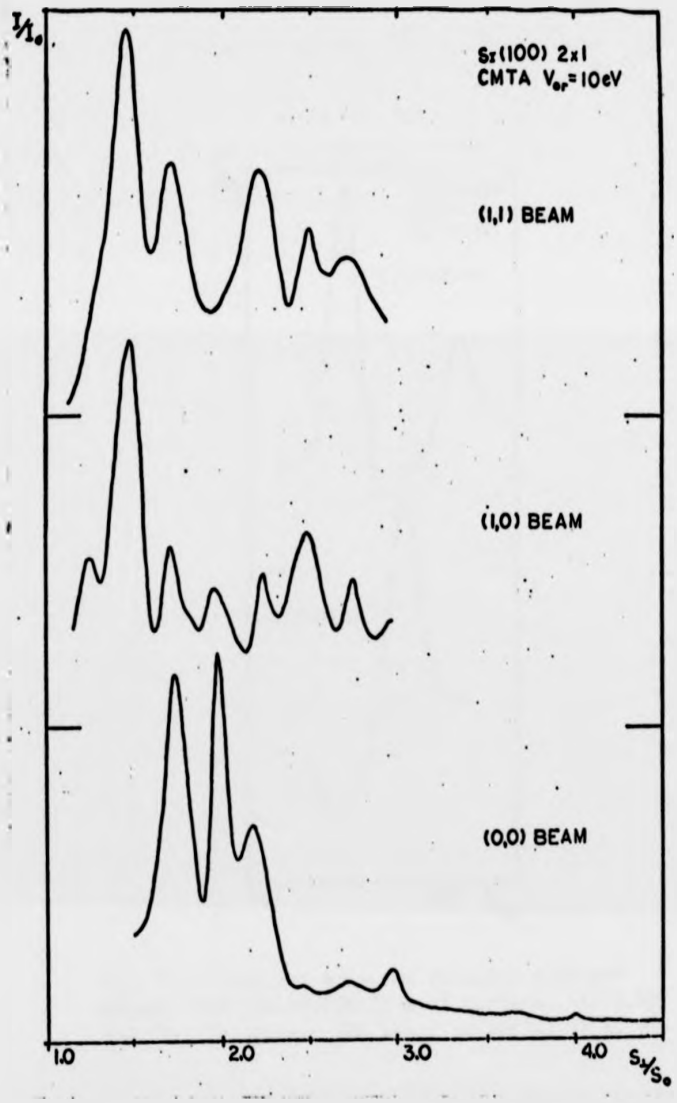

Fig. 7.3 Constant Momentum Transfer averaged spectra for the Si(100)(2 x 1) surface. (00), (1,0) and (1,1) beams. The inner potential is 10 eV.

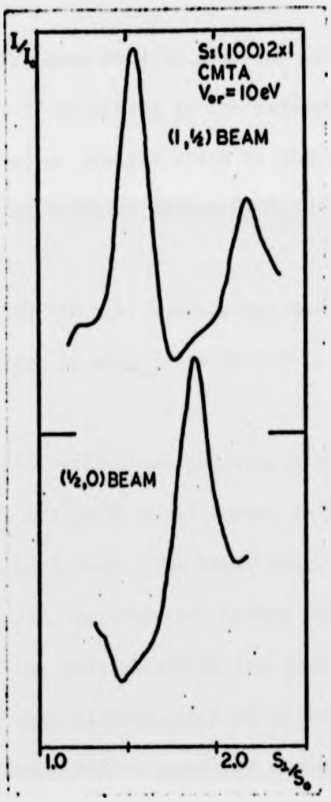

Fig. 7.4 Constant Momentum Transfer averaged spectra for the Si(100)(2 x 1) surface. (1/2,0) and (1,1/2) beams. The inner potential is 10 eV.

This spectrum consists of a single peak at $S_\perp/S_o \simeq 1.9$, its width is approximately 50% greater than that of the Bragg peak at similar momentum transfer in the (00) beam. This is just what we expect for a beam arising from a structure confined to a small number of atom layers.

The averaged (1,1/2) beam data is compiled for a range of angles of incidence 0 - 30° at 2° intervals in the azimuth $\phi = 26.5°$. The curve exhibits two peaks, of similar width to that of the peak in the (1/2,0) beam, at momentum transfer values $S_\perp/S_o \simeq 1.55$ and $\simeq 2.2$.

IVi. Discussion

Data averages for the (2 x 1) surface are markedly non-kinematic in appearance, with large, in some cases dominant, extra peaks in the spectra.

Comparing the results with those for the (1 x 1)H structure we note that in both cases the extra peaks appear in approximately the same momentum transfer positions. The Bragg features occur at similar values of momentum transfer as expected, indeed the inner potential value was chosen such that this should be the case for the highest energy Bragg peak. We note however, that while the lower energy Bragg peaks in the (1 x 1)H data tend to appear at momentum transfer values slightly above those predicted by kinematic theory for the bulk structure the reverse is true for the (2 x 1) data, with the Bragg peaks appearing slightly below the bulk positions. As we remarked in the discussion of the (1 x 1)H results, the shift of these peaks is indicative of surface layer contraction. Similarly we may interpret the shift

of (2 x 1) kinematic peaks to lower momentum transfer values in terms of a surface layer expansion, though this alone is insufficient to account for the (2 x 1) diffraction pattern. The widths of kinematic peaks in the (2 x 1) averages is somewhat less than that for similar peaks in the (1 x 1)H results, for example the second Bragg peak in the (2 x 1) (00) beam spectra has a width ~70% of the same peak in the (1 x 1)H average. This may be a result of narrowing of the (2 x 1) peaks by multiple scattering contributions which have not averaged out. Some slight broadening of (1 x 1)H Bragg peaks may be produced by surface layer contraction though the calculated curves were relatively insensitive to this effect.

IVii. Structural Analysis

We have commented on the differences between (1 x 1)H averages and those for the (2 x 1) surface. Clearly it is in these differences that the key to the solution of the (2 x 1) reconstruction must lie.

There are two possible interpretations of the extra structure within the (2 x 1) data averages.

1. That these peaks are primarily single scattering in origin and are due to the structural difference between the two surfaces. A kinematic calculation based on the correct model should then reproduce the features and enable the structure to be determined.

2. That the peaks are due to multiple scattering contributions which have not fully averaged out in the CMTA process. These features would not be reproduced by a kinematic calculation, even one based on the correct structural model. Determination of the (2 x 1) superstructure would then be impossible by the averaging method.

We will discuss these interpretations separately.

IVii(a). Single Scattering . Structural models for the (2 x 1) surface were discussed in Chapter One. Most proposed models have involved reconstruction of the top layer only, a rearrangement of only those atoms which would have dangling bonds in a (hypothetical) simply terminated structure. As was pointed out previously, our observation of the transformation to the (1 x 1)H structure seems to support this type of model, in particular the 'leaning rows' structure.

Model calculations were carried out by Woodruff [105] in an attempt to reproduce experimental (2 x 1) averaged data using a single scattering approach. It was found that no change in structure involving only one layer could account for the strong additional features present in the averages.

Adjustment of the top layer spacing in the model produced only changes in the positions and shapes of the bulk Bragg features. The non-specular beams were also insensitive to lateral displacements of atoms in the top layer. In a single scattering model the (00) beam is unaffected by the positions of atoms parallel to the surface. No significant extra peaks were produced by structural changes confined to the top layer.

Variation of the surface Debye temperature and the imaginary part of the inner potential (both of which affect the relative contribution of the top layer to the scattering) over very wide ranges did not modify this conclusion.

Consideration of interference effects, as observed in optics for example, clarifies this finding. In a single scattering model

interference maxima produced by a limited number of scattering layers tend to be rather broad. Electrons in this energy range sample a depth of 5 - 10 Å or approximately 4 to 8 layers. Thus a single layer reconstruction would produce features both weaker and significantly broader than the Bragg peaks. We note that the extra peaks in averaged data are only slightly broader than the kinematic features and are of similar intensity. In this model these extra peaks must result from interference in several reconstructed layers i.e., the reconstruction must be deep.

In order to examine this hypothesis further, while avoiding the complexity involved in a model structure of this type, further calculations were carried out by Woodruff using a layer scattering model for the (00) beam. Calculations for a range of layer spacings led to the conclusion that several layers (of the order of 4) must be involved if the features in experimental averages are to be reproduced. Alternatively, if layers are heavily distorted into sublayers this may be reduced to 4 sublayers (2 full layers), though with the same depth of reconstruction. Examination of the (1/2,0) and (1,1/2) beam averages supports this view.

IVii(b). Multiple Scattering. An alternative explanation for the extra structure in (2 x 1) experimental averages is simply that these are multiple scattering features which have not been fully averaged out.

Although some success in structure determination has been claimed for the CMTA method; previous studies have been mainly for relatively simple metal surface structures in which the only modification to the

bulk structure is a change in the top layer spacing (similar to our hydrogen adsorbed silicon surface). Even in these cases some residual multiple scattering structure is evident in averages. It is not particularly surprising that the first application of the technique to a reconstructed clean surface seems to produce significantly different results.

As we have remarked, the main difficulty in interpreting the extra peaks in the spectra is that they are narrow. This can only be explained in a single scattering model by deep reconstruction. However we know that multiple scattering peaks in individual Intensity-Energy spectra are narrow. Inadequate averaging would therefore produce similar features to those observed.

In support of this view we note that the extra features occur at the characteristic positions expected for multiple scattering features, as discussed previously.

One of the problems in the application of the CMTA method is of knowing the range over which averaging is necessary to effectively eliminate multiple scattering contributions. In applying the method to structural analysis one would normally regard successful averaging for a known surface structure as being indicative of the data range required for an average to determine an unknown structure of the same material. The simple answer to the large multiple scattering features, that the average was carried out for an insufficient range of data, would therefore seem hard to justify. Our difficulty then, in accepting a multiple scattering interpretation of these features, arises from the very

different results obtained for the two different Si(100) surface structures, when the averages were compiled for exactly the same range of data in each case.

If we accept this interpretation, the fact that the averaging procedure was successful in one case (the simple (1 x 1)H structure) and markedly unsuccesful in the other (the complex (2 x 1) reconstruction), clearly augurs ill for the future of the CMTA approach in surface structure determination. The method would appear to be useful only when we wish to ascertain the top layer spacing of an unreconstructed surface. In these cases single scattering structure is strong in individual spectra and highly dominant in averages. Complex surface reconstruction, at least in the Si(100)(2 x 1) case, produces very strong multiple scattering features which survive averaging. This may be a result of the more complex phase relationships between electron waves scattered from a variety of layer spacings, both normal to and parallel to the surface.

Once again structure determination by LEED is obstructed by strong multiple scattering contributions, which, as this study shows, are more highly structure dependent than are Bragg features, in addition to the strong dependence on scattering parameters noted in individual Intensity-Energy spectra.

V, Conclusions

Averages of data for the (1 x 1)H surface produce highly kinematic results with only weak residual multiple scattering peaks. Kinematical calculations indicate that the results are consistent with a surface

structure similar to the bulk (with the addition of hydrogen atoms, which 'take up' the dangling bonds), with a top silicon layer spacing which is probably contracted by ≈3%.

(2 x 1) averages, on the other hand, are markedly non-kinematic in appearance, with strong extra peaks in addition to the Bragg features. If these extra peaks are single scattering in origin this implies that the (2 x 1) reconstruction is deep (~4 layers). Such a structure would appear to be inconsistent with our observation of the unreconstruction of this surface on exposure to atomic hydrogen.

A possibly more likely explanation is that the extra peaks are due to multiple scattering. In view of the successful average obtained for the (1 x 1)H surface, for an identical range of data, this suggests that the CMTA method may not be useful in the case of reconstructed surfaces.

CHAPTER 8

SUMMARY

We have presented the results of a comprehensive Low Energy Electron Diffraction investigation of the silicon (100) surface.

LEED uniquely offers the opportunity of the determination of atomic structures as has been demonstrated in previous studies of other materials. As an introduction to the experimental work we set out the principles of LEED and described the evolution of theoretical methods aimed at the interpretation of experimental results. We also discussed the physical principles underlying dynamical theory and sought to emphasise the importance of multiple scattering processes in LEED, and the degree to which these processes increase the complexity of surface structure determination. Another method of analysis, the Constant Momentum Transfer Averaging method, was described. This approach is said to eliminate most of the effects of multiple scattering by averaging experimental data; the results may be compared with kinematic calculations.

It was concluded that a study of the Si(100) surface is well timed, and that the Si(100)(2 x 1) reconstruction provides an ideal case for an examination of the value of the CMTA method.

The experimental system used in these studies was described, together with the setting-up procedures required for accurate data collection. The system consists of a conventional LEED optics, with a moveable Faraday cup for intensity measurements and electronics systems for the plotting of Intensity-Enery spectra. An on-line computer system was used for some of the data collection work.

Auger Electron Spectroscopy is an invaluable technique for the determination of the purity of surfaces studied by LEED. The principles of Auger emission and its angular dependence were discussed. The equipment used here was of the conventional LEED-Auger retarding field type.

Cleaning procedures used to obtain a 'clean' well-ordered Si(100) surface were described. It was found that the most effective method was argon ion bombardment followed by annealing. Following ion bombardment (~470 eV, ~1 $\mu A/cm^2$) and annealing at ~900 °C for several minutes a clean surface was produced with carbon levels of C/Si $\approx 2 - 3 \times 10^{-3}$, expressed as the ratio of Auger peak heights. Other impurities, if present, had concentrations such that their peak heights were less than the noise level in Auger spectra, $\approx 1 \times 10^{-3}$ of the silicon peak height. Surface concentrations are difficult to determine, though we estimate that carbon concentrations are probably 1/60 to 1/6 monolayer depending on the distribution of the carbon detected. Concentrations of other impurities are likely to be less than this value. Surfaces were well ordered after annealing, with sharp LEED patterns and stable I-V spectra. The familiar Si(100)(2 x 1) structure was observed on clean surfaces

The angular dependence of Auger electron emission from (2 x 1) and (1 x 1)H surfaces was studied, using the Faraday cup for collection of Auger electron 'intensities.' Angular profiles were found to exhibit little well-defined structure due to the complexity of the diffraction process in silicon. It was concluded that the technique is of little value for structure determination in this case.

We have presented a large set of LEED Intensity-Energy spectra for the (2 x 1) surface. The profiles are complex, with large extra peaks in addition to the Bragg features. These extra peaks are probably multiple scattering in origin. The data show good agreement with the results of similar studies by two other groups of workers.

A previously unreported adsorption structure was found on the Si(100) surface. The Si(100)(1 x 1)H structure was produced by adsorption of atomic hydrogen at room temperature. Saturation of adsorption at (presumably) 1 monolayer was observed and the process was reversible. Heating of the specimen to 700 °C - 900 °C desorbed the hydrogen and restored the (2 x 1) phase. Impurity levels in the adsorbate structure were similar to those for the clean surface. It seems likely that atomic hydrogen simply saturates dangling bonds at the surface allowing 'unreconstruction' to a structure with a (1 x 1) surface net. This view suggests that the (2 x 1) reconstruction is confined to the top one or two layers, and vacancy models seem unlikely.

A large volume of LEED intensity data was collected for this surface. Spectra are much simpler than in the (2 x 1) case, with strong kinematic peaks and only small extra features. It was concluded that data from this bulk-like structure provides a valuable test case for the establishment of a reliable theoretical model of low energy electron scattering from silicon surfaces. Limited comparisons of experimental data with profiles calculated for the bulk structure by Jona *et al.* show fairly good agreement, suggesting that similar agreement for the (2 x 1) surface is within reach.

We have presented the results of CMT averaging of LEED data for the (2 x 1) and (1 x 1)H structures. For the (1 x 1)H surface a good fit was found with kinematic calculations produced by Woodruff. The analysis suggests that the structure is probably like the bulk, though with a top silicon layer spacing which is contracted by ≈3%. Averaged data for the (2 x 1) surface contains large fractional order Bragg peaks which cannot be reproduced by a kinematic calculation for a simple model of reconstruction, including all the models currently proposed. We conclude that the reconstruction may be deep (~4 layers or 2 full layers distorted into sublayers), which would seem to be in conflict with our observation of the structural transformation on hydrogen adsorption. An alternative explanation is that the extra peaks in averaged data are due to multiple scattering which the CMTA process has failed to eliminate. In view of the exactly similar range of data used in (1 x 1)H and (2 x 1) averages this would imply that CMTA is unlikely to be useful in the structure determination of reconstructed surfaces.

BIBLIOGRAPHY

1. R. E. Schlier and H. E. Farnsworth, "Semiconductor Surface Physics," Univ. of Pennsylvania Press, Philadelphia, Pa. (1957) 3; J. Chem. Phys. 30 (1959) 917.

2. J. J. Lander and J. Morrison, J. Chem. Phys. 37 (1962) 729; J. Appl. Phys. 33 (1962) 2089; 34 (1963) 1403.

3. J. D. Levine, Surface Sci. 34 (1973) 90.

4. J. C. Phillips, Surface Sci. 40 (1973) 459; 44 (1974) 290.

5. W. A. Harrison, Surface Sci. 55 (1976) 1.

6. D. Haneman, Phys. Rev. 121 (1961) 1093.

7. R. Seiwatz, Surface Sci. 2 (1964) 473.

8. C. J. Davisson and L. H. Germer, Phys. Rev. 30 (1927) 705.

9. H. E. Farnsworth, Phys. Rev. 34 (1929) 1287.

10. W. H. Ehrenburg, Phil. Mag. 18 (1934) 878.

11. E. D. Scheibner, L. H. Germer and C. D. Hartmann, Rev. Sci. Instrum. 31 (1960) 112; L. H. Germer and C. D. Hartmann, Rev. Sci. Instrum. 31 (1960) 780.

12. E. J. Scheibner and L. N. Tharp, Surface Sci. 8 (1967) 247; L. N. Tharp and E. J. Scheibner, J. Appl. Phys. 38 (1967) 3320.

13. R. E. Weber and W. T. Peria, J. Appl. Phys. 38 (1967) 4355.

14. L. A. Harris, J. Appl. Phys. 39 (1968) 1419.

15. T. W. Haas, G. J. Dooley III, J. T. Grant, A. G. Jackson and M. P. Hooker, Progr. Surface Sci. 1 (1971) 155.

16. E. G. McRae, J. Chem. Phys. 45 (1966) 3258.

17. D. S. Boudreaux and V. Heine, Surface Sci. 8 (1967) 426.

18. C. B. Duke and C. W. Tucker, Surface Sci. 15 (1969) 231; C. B. Duke, J. R. Anderson and C. W. Tucker, Surface Sci. 19 (1970) 117.

19. J. E. Demuth, P. M. Marcus and D. W. Jepsen, Phys. Rev. Lett. 31 (1973) 540; P. M. Marcus, J. E. Demuth and D. W. Jepsen, Surface Sci. 53 (1975) 501.

20. C. B. Duke, N. O. Lipari, G. E. Laramore and J. B. Theeten, Abstracts: 33rd Annual Conf. on Physical Electronics, Berkeley (1973) 46; C. B. Duke, N. O. Lipari and G. E. Laramore, Nuovo Cimento. 23 B (1974) 241; J. Vac. Sci. Technol. 11 (1974) 180.

21. S. Andersson, J. B. Pendry, B. Kasemo and M. A. van Hove, Abstracts: 33rd Annual Conf. on Physical Electronics, Berkeley (1973) 47; Phys. Rev. Lett. 31 (1973) 595; see also ref [24] cited in Marcus *et al.* [19].

22. T. C. Ngoc, M. G. Lagally and M. B. Webb, Phys. Rev. Lett. 26 (1971) 1557.

23. L. McDonnell, D. P. Woodruff and K. A. R. Mitchell, Surface Sci. 45 (1975) 1.

24. R. D. Heidenreich, "Fundamentals of Transmission Electron Microscopy," Interscience, New York (1964).

25. F. Jona, Surface Sci. 8 (1967) 478.

26. E. A. Wood, J. Appl. Phys. 35 (1964) 1306.

27. R. L. Park, Surface Sci. 11 (1968) 188.

28. S. Y. Tong, Progr. Surface Sci. 7 (1975) 1.

29. M. B. Webb and M. G. Lagally, Solid State Physics 28 (1973) 302.

30. J. B. Pendry, "Low Energy Electron Diffraction," Academic Press, London (1974).

31. H. Bethe, Annalen der Physik 87 (1928) 55.

32. P. M. Morse, Phys. Rev. 35 (1930) 1310.

33. M. Lax, Rev. Mod. Phys. 23 (1951) 287; Phys. Rev. 85 (1952) 621.

34. D. Pines, "The Many Body Problem," Benjamin, New York (1962).

35. J. L. Beeby, J. Phys. C 1 (1968) 82.

36. J. B. Pendry, J. Phys. C 4 (1971) 2501, 2514.

37. S. Y. Tong and T. N. Rhodin, Phys. Rev. Lett. 26 (1971) 711.

38. C. B. Duke and G. E. Laramore, Phys. Rev. B 2 (1970) 4765, 4783.

39. D. W. Jepsen, P. M. Marcus and F. Jona, Phys. Rev. Lett. 26 (1971) 1365.

40. D. W. Jepsen, P. M. Marcus and F. Jona, Phys. Rev. B 5 (1972) 3933.

41. P. M. Marcus and D. W. Jepsen, Phys. Rev. Lett. 20 (1968) 925.

42. G. Capart, Surface Sci. 26 (1971) 429.

43. J. B. Pendry, Phys. Rev. Lett. 27 (1971) 856; J. Phys. C. 4 (1971) 3095.

44. B. W. Holland and R. S. Zimmer, J. Phys. C. 8 (1975) 2395.

45. F. Herman and S. Skillman, "Atomic Structure Calculations," Prentice Hall, Englewood Cliff, N. J. (1963).

46. T. A. Clarke, R. Mason and M. Tescari, Surface Sci. 30 (1972) 553.

47. C. W. Tucker and C. B. Duke, Surface Sci. 23 (1970) 411; 29 (1972) 237.

48. M. G. Lagally, T. C. Ngoc and M. B. Webb, J. Vac. Sci. Technol. 9 (1972) 645.

49. J. C. Buchholtz, G. C. Wang and M. G. Lagally, Surface Sci. 49 (1975) 508.

50. D. P. Woodruff, Discuss. Faraday Soc. 60 (1976) 218.

51. L. McDonnell and D. P. Woodruff, Vacuum 22 (1972) 477; L. McDonnell, Ph.D. Thesis, University of Warwick (1975).

52. M. P. Seah, Ph.D. Thesis, University of Bristol (1969).

53. E. H. S. Burhop, "The Auger Effect and other radiationless transitions," University Press, London (1952).

54. P. Auger, J. Phys. Radium 6 (1925) 205.

55. J. J. Lander, Phys. Rev. 91 (1953) 1382.

56. H. G. Maguire and P. D. Augustus, J. Phys. C. 4 (1971) L174.

57. P. W. Palmberg, G. E. Riach, R. E. Weber and N. C. MacDonald, "Handbook of Auger Electron Spectroscopy," Physical Electronics Industries, Edina, MN (1972).

58. H. E. Bishop and J. C. Rivière, J. Appl. Phys. 40 (1968) 1740.

59. R. E. Weber and A. L. Johnson, J. Appl. Phys. 40 (1969) 319.

60. P. W. Palmberg and T. N. Rhodin, J. Appl. Phys. 39 (1968) 2425.

61. C. C. Chang, Surface Sci. 23 (1970) 283.

62. C. C. Chang, Surface Sci. 25 (1971) 53.

63. J. T. Grant and T. W. Haas, Surface Sci. 24 (1971) 332.

64. B. D. Powell, D. P. Woodruff and B. W. Griffiths, J. Phys. E. 8 (1975) 548.

65. H. E. Bishop and J. C. Rivière, J. Phys. D. 2 (1969) 1635.

66. N. J. Taylor, Surface Sci. 17 (1969) 466.

67. G. F. Amelio, Surface Sci. 22 (1970) 301.

68. M. F. Chung and L. H. Jenkins, Surface Sci. 26 (1971) 649.

69. G. O. Krause, Phys. Stat. Sol. A 3 (1970) 899.

70. R. C. Henderson, W. J. Polito and J. Simpson, Appl. Phys. Lett. 16 (1970) 15.

71. R. Liebermann and D. L. Klein, J. Electrochem. Soc. 113 (1966) 956.

72. R. C. Henderson, R. B. Marcus and W. J. Polito, J. Appl. Phys. 42 (1971) 1208.

73. R. C. Henderson and R. F. Helm, Surface Sci. 30 (1972) 310.

74. R. C. Henderson, J. Electrochem. Soc. 119 (1972) 772.

75. F. Jona, private communication.

76. J. M. Charig and D. K. Skinner, Surface Sci. 15 (1969) 277.

77. H. C. Abbink, R. M. Broudy and G. P. McCarthy, J. Appl. Phys. 39 (1968) 4673.

78 B. A. Joyce, J. H. Neave and B. E. Watts, Surface Sci. 15 (1969) 1.

79. P. Rai Choudhury and N. P. Formigon, J. Electrochem. Soc. 116 (1969) 1440.

80. F. Jona, Appl. Phys. Lett. 6 (1965) 205.

81. A. Ignatiev, F. Jona, M. Debe, D. C. Johnson, S. J. White and D. P. Woodruff, J. Phys. C. to be published.

82. B. W. Holland, L. McDonnell and D. P. Woodruff, Solid State Commun. 11 (1972) 991.

83. L. McDonnell, D. P. Woodruff and B. W. Holland, Surface Sci. 51 (1975) 249.

84. T. Matsudaira, M. Watanabe and M. Onchi, Japan J. Appl Phys. (Suppl) 2 (1974) 181.

85. J. R. Noonan, D. M. Zehner and L. H. Jenkins, J. Vac. Sci. Technol. 13 (1976) 183.

86. G. Allié, E. Blanc and D. Dufayard, Surface Sci. 57 (1976) 293.

87. J. W. Gadzuk, Phys. Rev. B 10 (1974) 5030.

88. A. Liebsch, Phys. Rev. Lett. 32 (1974) 1203.

89. J. B. Pendry, J. Phys. C 8 (1975) 2413.

90. B. W. Holland, J. Phys. C 8 (1975) 2679.

91. D. P. Woodruff, Surface Sci. 53 (1975) 538.

92. D. P. Woodruff, private communication.

93. L. McDonnell and D. P. Woodruff, Surface Sci. 46 (1974) 505.

94. M. P. Seah, Surface Sci. 17 (1969) 181.

95. S. J. White and D. P. Woodruff, J. Phys. C 9 (1976) L451.

96. J. T. Law, J. Chem. Phys. 30 (1959) 1568.

97. H. Ibach and J. E. Rowe, Surface Sci. 43 (1974) 481.

98. T. Sakurai and H. D. Hagstrum, Phys. Rev. B 14 (1976) 1593.

99. L. C. Burton, J. Appl. Phys. 43 (1972) 232.

100. B. A. Joyce and J. H. Neave, Surface Sci. 34 (1973) 401.

101. G. E. Becker and G. W. Gobeli, J. Chem. Phys. 38 (1963) 2942.

102. F. Jona, D. W. Jepsen and P. M. Marcus, unpublished.

103. J. Eisinger, J. Chem. Phys. 30 (1959) 927.

104. S. J. White and D. P. Woodruff, 4th NEVAC Symposium on Surface Physics, Eindhoven (June 1976); to be published in Surface Sci.

105. S. J. White and D. P. Woodruff, Surface Sci. to be published.